DESIGN AND CONSTRUCTION OF A NEW ULTRACOLD YTTERBIUM EXPERIMENT FOR RYDBERG PHYSICS

PHILIPP LUNT

Supervisor: Dr. Sebastian Hofferberth
University of Southern Denmark

Master Thesis
1st of January 2019

ABSTRACT

In the scope of this thesis the design and implementation of a new experimental setup is presented aiming to explore Rydberg atom mediated nonlinear quantum optics by using the alkaline-earth-like atomic species ytterbium.

A fundamental property of the constituent quanta of light is their extremely weak interaction among each other. The creation of strong nonlinearities at the level of single photons is of basic interest to explore new realms of elementary physics and of technical significance for future applications exploiting fundamental principles of quantum mechanics. The strong, long-range interaction of Rydberg atoms in ultracold atomic ensembles allows a significant enhancement of optical nonlinearities enabling the control of light on the most fundamental, single photon level. It paves the way for unique applications including the realization of exotic, strongly correlated many-body states of light and matter, non-classical light sources, and all-optical quantum logic building blocks.

This thesis reports the progress on the construction of a new experiment for nonlinear quantum optics based on Rydberg atoms with the novel approach of using the alkaline-earth-like element ytterbium. The production of ultracold ytterbium ensembles is approached by a two chamber setup presented in detailed description. It includes a two-dimensional magneto-optical trap as a source of cold atoms and a science chamber containing an electric field control required for high-precision electric field compensation to avoid line shifts and broadening of the highly polarizable Rydberg atoms. The performance of these crucial design components is quantitatively verified with extensive numerical simulations. Further, the setup of the complete laser system is discussed. In particular focus is placed on the frequency stabilization to an ultrastable, high-finesse cavity which is characterized by means of the beat note signal of two lasers simultaneously locked to the cavity yielding a beat note linewidth of below 100 Hz.

RESUMÉ

I dette speciale beskrives design og implementering af en ny eksperimentel opstilling som skal bruges til eksperimenter med Rydbergatommedieret ulineær kvanteoptik med det jordalkalimetallignende grundstof ytterbium.

En fundamental egenskab af de grundlæggende kvanter af lys er deres ekstremt svage interaktion med hinanden. Derfor er realiseringen af stærke uliniariteter på enkeltfotonniveau af stor interesse som mulighed for at udforske nye domæner af grundlæggende fysik og af teknisk vigtighed som grundsten for nye, innovative teknologier. De stærke, langtrækkende interaktioner mellem Rydbergatomer i ultrakolde atomensembler tillader en signifikant forstærkning af optiske ulinearitet, som muliggør kontrol over lys på det mest fundamentale niveau, Enkeltfotonniveau. Derved får man adgang til unikke applikationer såsom realisering af eksotiske, stærkt korrelerede mangelegemetilstande af lys og stof, ikke-klassiske lyskilder og fuldoptiske elementer til kvante-logiske operationer.

Dette speciale rapporterer fremskridtet af konstruktionen af et nyt eksperiment til ulineær kvanteoptik baseret på Rydbergatomer. I det nye eksperiment bruges der som noget nyt indenfor feltet det jordalkalimetallignende grundstof ytterbium. Produktionen af ultrakoldt ytterbiumensembler foregår med en to-kammeropstilling som beskrives i detaljer i specialet. De to kamre er en todimensional magnetooptisk fælde som kilde til kolde atomer og et videnskabskammer, som indeholder en anordning til elektrisk feltkontrol, til præcis kompensation af elektriske felter som er nødvendig for at undgå energiniveauforskydninger og -udbredning af de yderst polariserbare Rydbergatomer. Præstationen af disse kritiske komponenter bliver kvalitativt prøvet med omfattende numeriske simuleringer. Endvidere bliver opstillingen af det fuldstændige lasersystem diskuteret. Der er især lagt fokus på frekvensstabiliseringen til en ultrastabil højfinessekavitet, som karakteriseres ved hjælp af beatsignalet mellem to lasere, der begge er låst til kaviteten, og som giver en linjebredde af beatsignalet, der er mindre end 100 Hz.

CONTENTS

INTRODUCTION

This is an experimental thesis in the field of nonlinear quantum optics. The core goal of this research area is the creation of strong nonlinearities in optical materials which enable effective interactions between individual photons [1]. On a fundamental level, this allows the investigation of exotic quantum many-body states of light such as photon liquids and photon crystals [2–5] but also paves the way for quantum computation [6] and quantum simulation [7], as direct scientific applications. This opens up new insights on an elementary basis of quantum physics and on the other hand, could establish new technologies for high-speed information processing based on optics [8].

The central problem of nonlinear quantum optics is the enhancement of the tiny atom-photon scattering cross-section. In general, the coupling of a light field to a single atom is very weak which has the consequence of low optical nonlinearities, thus, nonlinear effects as spontaneous parametric down/up conversion only occur at high intensities [9]. One approach to increase these nonlinearities is to confine light temporally and spatially in a cavity [10] or in a waveguide [11].

However, a different approach is to exploit the long-range, dipole-dipole interactions of Rydberg atoms [12, 13] combined with the technique of electromagnetically induced transparency (EIT) to create effective interactions between individual photons [14]. Rydberg states have at least one valence electron excited to a high principle quantum number [12]. They exhibit exaggerated properties in terms of their size, polarizability, lifetime and strong interaction with other atoms which is tunable from van-der-Waals to dipole-dipole interaction [15]. An important manifestation is the Rydberg blockade mechanism in which a second Rydberg excitation is suppressed for nearby atoms due to an energy shift of their Rydberg levels [16]. Based on that, entanglement of an entire ensemble of atoms and coherent manipulation by a single photon can be realized [17, 18]. The second key technique is EIT describing the optical phenomenon that a two-photon transition renders an initially opaque medium transparent by means of destructive interference of the quantum mechanical transition amplitudes [19]. A photon entering a medium under induced transparency conditions is excited to a quasi-particle termed as dark-state polariton which exhibits both photonic and matter character [20]. The dark-state polariton features intriguing properties in that the group velocity can be reduced significantly to million times slower than the speed of light in vacuum [21].

The combination of both concepts maps the interaction of the Rydberg atoms onto the optical transition. A so called Rydberg-polariton propagates slowly through the medium whereas the excitation of a second Rydberg-polariton nearby is suppressed by the Rydberg blockade mechanism. As a consequence, the photon statistics of the transmitted light which characterizes whether the light is classical or non-classical can be changed. First time proposed in 2005 [14] and experimentally realized in 2010 [22] a complete new control and manipulation of single photons and generation of non-classical light opened up. In the following years several experiments were performed leading to the realization of optical materials which are nonlinear to single photons by strongly interacting Rydberg atoms [23], the implementation of coherent storage of optical photons by means of Rydberg-polaritons [24], the creation of polarization-entangled photon pairs, i.e. bound states of two photons [25] and even up to three-photon correlations [26]. In parallel, a thorough theoretical framework was developed [2, 3, 27–29] which led to a deep understanding of the underlying mechanisms .

Almost all Rydberg atom experiments in the last decade are performed with alkali atoms due to their simplicity, i.e. their similarity to the hydrogen atom. However, in the last years a trend towards the usage of alkaline-earth-like atoms is observable [30–34]. This movement is motivated by the more complex internal structure of these atomic species which could enable a new platform for studying Rydberg physics phenomena. The presence of two valence electrons allows the production of both singlet and triplet states which exhibit a diversity of attractive and repulsive interactions. Furthermore, the excitation of one electron to a Rydberg state leaves an optically active core ion offering several manipulations of the second valence electron [35]. Excitation of the second valence electron into low orbital momentum quantum number states leads to autoionization caused by single violent electron-electron collisions [36]. However, excitation into high orbital quantum number states does not induce autoionization allowing for instance optical imaging of Rydberg states. Moreover, the second valence electron admits the possibility of simultaneously trapping of ground and Rydberg states [37].

ABOUT THIS THESIS

This thesis reports on the setup of a new developed apparatus for experiments on ultracold ytterbium Rydberg atoms. The experiment aims for studying nonlinear quantum optics with the novel approach of exploiting the advantages of ytterbium to create a large, free-space medium in which many-body phenomena of strongly interacting Rydberg-polaritons can be investigated. Further, it is intended to explore the novel field of alkaline-earth-like Rydberg physics.

The planned ytterbium machine comprises a two chamber approach. This includes a two-dimensional magneto optical trap (2D MOT) as a source of cold atoms where the 2D MOT is loaded directly from a stream of atoms emitted from dispensers. Numerical simulations of atoms in a 2D MOT are performed in order to gain an intuitive understanding of the performance but also to analyze protection measures in terms of optical deterioration of the vacuum chamber exposed to ytterbium atoms.

Further design goal is extremely precise electric field control and field ionization for detecting ionized Rydberg atoms. The exaggerated sensitivity of Rydberg atoms requires suppression of external field fluctuations yielding increased coherence times of the Rydberg states. Building on the existing knowledge of the neighboring experiment a similar electric field control design is chosen which provided exceptional results in terms of stability and tunability of electric fields [38–40]. Numerical simulations are performed indicating that with the chosen setup similar suppression of electric stray fields and successful detection of Rydberg ions on a microchannel plate is achievable.

Precise Rydberg spectroscopy requires high stabilization of the laser system. The radiative lifetime of the Rydberg atoms scales with the principle quantum number n^3 which demands control of the excitation laser linewidth typically down to kHz to address the proper Rydberg state. An ultrastable, high-finesse cavity is used as a passive reference frequency providing the necessary stability and precision of the lasers.

This thesis is structured as follows. The first chapter 1 introduces alkaline-earth-like atoms and in particular the species ytterbium with its relevant properties along with prospects ytterbium could offer for Rydberg quantum optics experiments. The chapters 2, 3, 4 discuss the design of the experiment and simulations on which the design decisions are founded. In particular, chapter 2 introduces the complete setup and a description of a future experiment to give the reader an overview. Chapter 3 concentrates on design decisions of the 2D MOT chamber while chapter 4 presents the electric field control design. The last chapter 5 characterizes the laser system, especially focused on the laser locking system to an ultrastable reference cavity. The

conclusion chapter 6 summarizes the results and gives a survey of the current status of the experiment and a brief plan on the next steps towards the realization of ultracold ytterbium Rydberg atoms.

1

ULTRACOLD YTTERBIUM FOR NONLINEAR QUANTUM OPTICS

For almost two decades now, alkaline-earth-like elements have drawn great attention for ultracold quantum optics experiments. In particular, the element ytterbium (Yb) stands out with remarkable properties exploited in broad applications. Pioneering work was done by the group of Y. Takahashi from Kyoto who were the first to observe degenerate Bose and Fermi gases of Yb [41, 42], followed by a strong development towards the investigation of many-body physics in optical lattices for quantum computation [43–47], even with subwavelength spatial structure [48] and also the realization of a Mott insulator [49]. Furthermore, the narrow clock transition of Yb also allows the construction of extremely precise frequency standards for quantum metrology, not for nothing is the most precise atomic clock to date based on Yb [50] but also transportable atomic clocks are built for testing gravitational theory [51].

The unique features of alkaline-earth-like atoms offer versatile tools for investigating new realms of Rydberg atom mediated nonlinear quantum optics. In contrast to alkali atoms, the two valence electrons admit the possibility of singlet and triplet Rydberg states [52]. The availability of broad and narrow transitions offer advantages for laser cooling [53] and for applications for Rydberg dressing [30]. Furthermore, the wavelength matching of the two-photon transition from the ground to Rydberg state minimizes dephasing processes [54]. In this chapter, a brief overview of the relevant properties of Yb is given, followed by a prospect for nonlinear quantum optic experiments based on Yb.

1.1 YTTERBIUM PROPERTIES

Yb is a rare-earth element of the lanthanide series with proton number $Z = 70$. Its full electronic structure is $[\mathrm{Xe}]4f^{14}6s^2$ which is mainly determined by the two valence electrons in the $6s$-shell. Therefore, its optical properties are quite similar to alkaline-earth atoms. It is a soft, malleable and ductile element and has its melting point at 824 °C and boiling point at 1196 °C [55]. The atomic source requires typically temperatures between 400 °C and 500 °C to produce a sufficient flux. Another important property of Yb is its low vapour pressure at room temperature $p_{\mathrm{Yb,RT}} \sim 10^{-21}$ mbar which is orders of magnitudes smaller compared to rubidium $p_{\mathrm{Rb,RT}} \sim 10^{-7}$ mbar, a standard element used in cold atom experiments. Hence, Yb that collides with a surface does not evaporate off but sticks to it. This requires several precautions

Table 1.1: Seven stable isotopes of Yb. The abundances are from [59] and the masses from [60].

ISOTOPE	MASS [u]	ABUNDANCE	NUCLEAR SPIN	STATISTICS
^{168}Yb	167.933 897	0.12 %	0	bosonic
^{170}Yb	169.934 761 8	2.98 %	0	bosonic
^{171}Yb	170.936 325 8	14.09 %	1/2	fermionic
^{172}Yb	171.936 381 5	21.68 %	0	bosonic
^{173}Yb	172.938 210 8	26.10 %	5/2	fermionic
^{174}Yb	173.938 862 1	32.03 %	0	bosonic
^{176}Yb	175.942 571 7	13.00 %	0	bosonic

in order to avoid deterioration of optical access by coating the viewports with Yb atoms. Several groups report fast degradation of optical access of viewports which are exposed to Yb flux [56, 57].

A remarkable feature of Yb is the high number of stable isotopes. It has seven stable isotopes of which two are fermions ^{171}Yb,^{173}Yb whereas five are bosons ^{168}Yb, ^{170}Yb, ^{172}Yb, ^{174}Yb, ^{176}Yb. Important properties are summarized in table 1.1. Interestingly, the ground states of all alkaline-earth atoms and of the lanthanide Yb have total angular momentum $J = 0$ and the bosonic isotopes have nuclear spin $I = 0$ [58], highlighting that the Yb electron structure closely resembles that of alkaline-earth atoms. However, the fermionic isotopes ^{171}Yb and ^{173}Yb have nuclear spin $I = 1/2$ and $5/2$, respectively.

Electronic Structure

The electronic structure of Yb resembles the one of alkaline-earth atoms which again is similar to helium due to the presence of two valence electrons. The level scheme with releveant states and transitions is shown in Fig. 1.1. Each level is denoted by $^{2S+1}L_J$, with the total spin S, the total orbital angular momentum L and the total angular momentum $J = L + S$ [61]. Two distinct level manifolds are formed by the arrangement of the two valence electrons with total spin $S = 0$ known as singlet states and $S = 1$ noted as triplet states. The two manifolds connect via narrow optical transitions, termed as intercombination transitions, which are electric dipole forbidden for pure LS-coupling. However, the high Z number of Yb creates spin-orbit interaction between the $^1P_1$ and $^3P_1$ which leads to a finite dipole coupling of the ground state $^1S_0$ and the triplet state $^3P_1$ [61]. On the other hand, the transitions within the manifolds are broad and mainly in the visible spectrum.

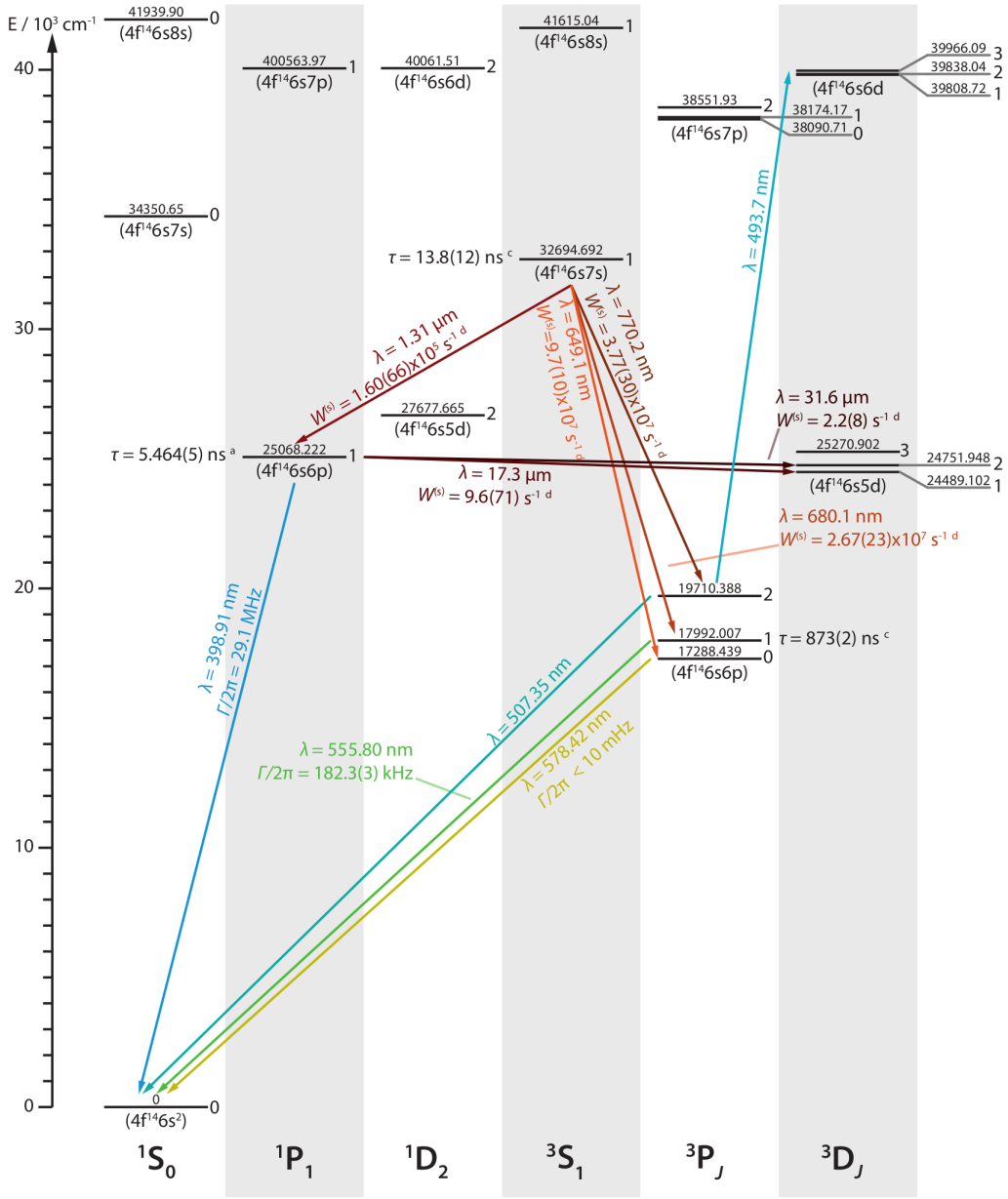

Figure 1.1: Level diagram of ^{174}Yb. The relevant energy levels and transitions for mainly cooling Yb atoms are illustrated, taken from [56].

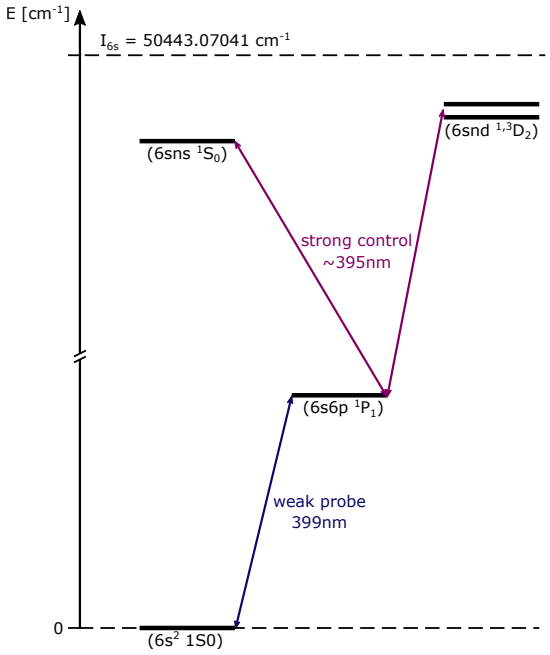

Figure 1.2: Two-photon transition from the ground to Rydberg state. The ground state is coupled with a weak, single photon probe laser to the intermediate state. The Rydberg state is excited by strong control laser.

In particular, the attention is concentrated on two transitions: the broad, singlet ${}^1S_0 \to {}^1P_1$ and the narrow, triplet ${}^1S_0 \to {}^3P_1$ transition, typically exploited for cooling. The singlet transition has a wavelength $\lambda_s = 398.9\,\mathrm{nm}$ in the near ultra-violet but still visible as purple-blue in the optical spectrum. It is mainly used for magneto-optical trapping and absorption imaging owing to its broad linewidth $\Gamma_s/2\pi = 29.12\,\mathrm{MHz}$ [62], but has a high saturation intensity $I_{\mathrm{sat}} = 2\pi^2\hbar c/(3\lambda^3)\Gamma_s = 59.97\,\mathrm{mWcm^{-2}}$ [63]. It is an almost closed cycle with a very weak radiative decay channel from $6s6p\ {}^1P_1 \to 5d6s\ {}^3D_{1,2} \to 6s6p\ {}^3P_{0,1,2}$ with lifetimes 329 ns and 460 ns, respectively [64, 65]. However, the loss of atoms via this decay channel is insignificant since efficient cooling is still possible without a repump laser [44, 56, 57]. The triplet transition ${}^3P_1$ has a wavelength 555.8 nm noticed as a bright green color to which the eye is extremely sensitive. With a linewidth $\Gamma_p/2\pi = 182.3\,\mathrm{kHz}$ and a saturation intensity $I_{\mathrm{sat}} = 0.14\,\mathrm{mWcm^{-2}}$ a low Doppler temperature $T_D = \hbar\Gamma_p/2k_B = 4.4\,\mu\mathrm{K}$ can be readily achieved. A very weak magnetic dipole decay channel from the ${}^3P_1$ state to the ${}^3P_0$ states exists [66] but is negligible for the experiments we have in mind.

There are many ways to excite the ground state atom to a Rydberg state ranging from single- to multi-photon transitions. A single-photon transition would require ultra-violet wavelengths since the first ionization limit is $I_{6s} = 50\,443.070\,41\,\mathrm{cm^{-1}}$ [67]. Even though only one laser is necessary the production of ultra-violet light is difficult and the Rydberg excitation line is Doppler-broadened. Instead, a two-photon transition via an intermediate level is used for exciting Rydberg states, illustrated in

Fig. 1.2. Both wavelengths are in the optical spectrum and with counterpropagating beams Doppler shifts can be countered. Besides these technical advantages, the two-photon transition allows to make use of EIT. Further advantages in regards of nonlinear quantum optics are discussed in the following section.

More detailed descriptions of Yb properties can be found in the following PhD theses [44, 56, 68].

1.2 NONLINEAR QUANTUM OPTICS MEDIATED BY RYDBERG ATOMS

In nonlinear quantum optics the nonlinearity becomes significant even on the level of individual photons. The key figure of merit of the strength of the nonlinearity is the blockaded optical depth $OD_\mathrm{b} = (2r_\mathrm{b}/L)OD$ with the diameter of the blockaded sphere $2r_\mathrm{b}$, the length L of the optical medium and the optical depth OD. To enter the quantum nonlinear regime $OD_\mathrm{b} \geq 1$ is required. However, the limitation of the atomic density sets a fundamental restriction of the OD_b without affecting the coherence or the life time of the Rydberg atoms [39, 69]. The possibilities of alkaline-earth-like atoms, and in particular Yb, to exceed the limitations of alkali atoms and to offer new aspects for nonlinear quantum optics experiments mediated by Rydberg atoms are outlined below.

— *Simple energy level scheme:* The bosonic isotopes of alkali-earth atoms and Yb have a relatively simple energy level structure compared to alkali atoms. The ground state is insensitive to magnetic fields due to the vanishing total angular momentum $J = L + S$ and nuclear spin I. The lack of hyperfine structure precludes the requirement of a repump laser, i.e. optical pumping, for cooling the atoms, as it is typically the case for alkali atoms, since the decay into different lower hyperfine states does not take place.

— *Cooling transitions:* The level structure of Yb offers two practical, almost closed-cycle cooling transitions: The dipole allowed ${}^1S_0 \rightarrow {}^1P_1$ singlet transition and the semi-forbidden triplet transition ${}^1S_0 \rightarrow {}^3P_1$. While the singlet transition can be used for slowing and magneto-optical trapping large numbers of atoms [70] the triplet transition can be exploited for achieving Doppler temperatures below 10 µK [41] lower than for alkali atoms. Typically, alkali atoms require additional cooling techniques resulting in a high loss of atom numbers to achieve such cold temperatures. Hence, this is a promising starting point for attaining a high optical depth with Yb.

— *Rayleigh length:* Limiting factor for the length of a Rydberg EIT medium in free-space is the wavelength of the probe light. Typically, the atomic cloud is positioned in the focus of the probe beam which diverges on the length scale

of the Rayleigh length $z_R = \pi w_0^2/\lambda$ with the waist w_0 and the wavelength λ of the probe beam. In order to excite Rydberg states with a reasonable probability the diameter of the probe beam requires to be smaller than the blockade radius $2w_0 < r_b$, meaning that $w_0 < 10\,\mu m$ for all previous experiments with alkali atoms. In contrast to alkali atoms which have probe beam wavelengths in the infrared, Yb offers a near ultra-violet wavelength allowing a large EIT-medium in which interactions of a large number of Rydberg-polaritons can be investigated.

— *Long coherence times:* Dephasing mechanisms in photon storage techniques based on collective Rydberg excitations stem mainly from thermal atomic motion and decoherence. The collective Rydberg excitation is described as [71]

$$|R\rangle = \frac{1}{\sqrt{N}} \sum_{j=1}^{N} e^{i(k_c - k_p) r_j} |g_1, \ldots, r_j, \ldots, g_N\rangle ,$$

with counterpropagating probe k_p and control beam k_c reduced to one dimension, the position r_j of atom j and the state $|g_1, \ldots, r_j, \ldots, g_N\rangle$ with all atoms in the ground state $|g\rangle$ except the atom j in the Rydberg state $|r\rangle$. The phase factor

$$(k_c - k_p) r_j = 2\pi \left(\frac{1}{\lambda_c} - \frac{1}{\lambda_p} \right) vt =: \frac{t}{\tau_{coh}}$$

with the mean velocity of the atoms v, sets the upper limit of the coherence time scale τ_{coh}. While the affect of thermal atomic motion can be reduced by cooling the atoms the decoherence results from the wavelength mis-match of the two-photon transition from the ground to Rydberg state [54]. In Yb, the upper limit of the coherence time scale for temperatures 10 µK close to the Doppler temperature of the triplet transition is $\tau_{coh,Yb} = 80\,\mu s \gg 2\,\mu s = \tau_{coh,Rb}$ significantly larger compared to rubidium, yielding longer coherence times.

— *P-wave shape resonance:* The formation of Rydberg molecules takes place at high blockaded optical depths due to increased scattering of the slow Rydberg electron from neutral atoms. The increase of bound atoms causes a shift and an asymmetric broadening of the Rydberg line. This density-dependent dephasing mechanism sets a fundamental limit for Rydberg quantum optics experiments [72, 73]. More specific, the scattering of a Rydberg electron from a ground state atom can be described by Fermi's pseudopotential which includes s- and p-wave scattering contributions [74]. In alkali atoms, the occurence of a strong p-wave shape resonance causes a steep dip in the molecular potential for small internuclear distances. This p-wave shape resonance is not present for instance for strontium [75]. It is anticipated that the p-wave shape resonance is non-existing for Yb potentially opening a new density limit for Rydberg quantum optics experiments.

— *Fermionic isotopes:* Alkaline-earth-like atoms offer a multitude of stable isotopes, both bosons and fermions. In constrast to their bosonic counterparts, identical fermions with short-range interaction do not collide with each other at low temperatures since s-wave scattering between identical fermions is inhibited due to the antisymmetry of the wavefunction [76]. However, the large elastic collision rate of the fermionic isotope ^{173}Yb is sufficient to achieve to quantum degeneracy of identical fermions by evaporative cooling [42]. Hence, Yb could offer a new playground of Rydberg-EIT with fermionic atom species.

2

EXPERIMENT SCHEME

In this chapter, the technical design of the experiment setup is presented. The setup consists of two key parts, the 2D MOT chamber in which atoms are transversely loaded in a 2D MOT and the ultra-high vacuum science chamber in which the atoms are trapped in a 3D MOT. First, the overall experiment design is presented, followed by a detailed discussion of the two central parts, the 2D MOT chamber and the science chamber. The last section gives an overview of the scheme of a future experiment, however not realized yet in the framework of this thesis. To the submission date of this thesis the experiment is not assembled yet!

2.1 COMPLETE EXPERIMENT SETUP

A new experiment for studying nonlinear quantum optics with Yb is designed and partly constructed during this thesis. A conceptual approach of a 2D MOT as a source of cold atoms subsequently loading a 3D MOT is chosen, explained in detail in section 2.2 and2.3. Inpsirations are taken from the first 2D MOT for Yb [56] and a 2D MOT for lithium atoms [77]. The design with its key components is shown in Fig. 2.1 as a CAD model.

Achieving ultra-high vacuum in the science chamber depends on the choice of material, the assembly, depumping and purification. In order to achieve these low pressures the vacuum chamber of cold atomic experiments is often split into two regimes. One region with a high background pressure of the species that is dealt with and the second region to which the atoms are transferred. The transportation of atoms can be examined by spatially moving the magnetic trap potential [78], by trapping atoms in the focus of an infrared laser [79], by using a Zeeman slower [80] or a 2D MOT [77].

Unlike alkali atoms, Yb can not be loaded practically from a background gas due to the low vapor pressure (see chapter 1). Yb sticks to any surface it gets in contact with and therefore degrades the optical access in short period of time. Thus, Yb is loaded from a stream of atoms experimentally accomplished by using either a Zeeman slower [41, 70, 81] or a 2D MOT [82] as a source of atoms in an initial cooling stage. The 2D MOT approach has the advantage of a simple and compact setup with potentially similar loading rates as for Zeeman slowers [82]. It does not require an atomic oven which are usually operated at temperatures in the range 100 °C – 500 °C [83]. In fact,

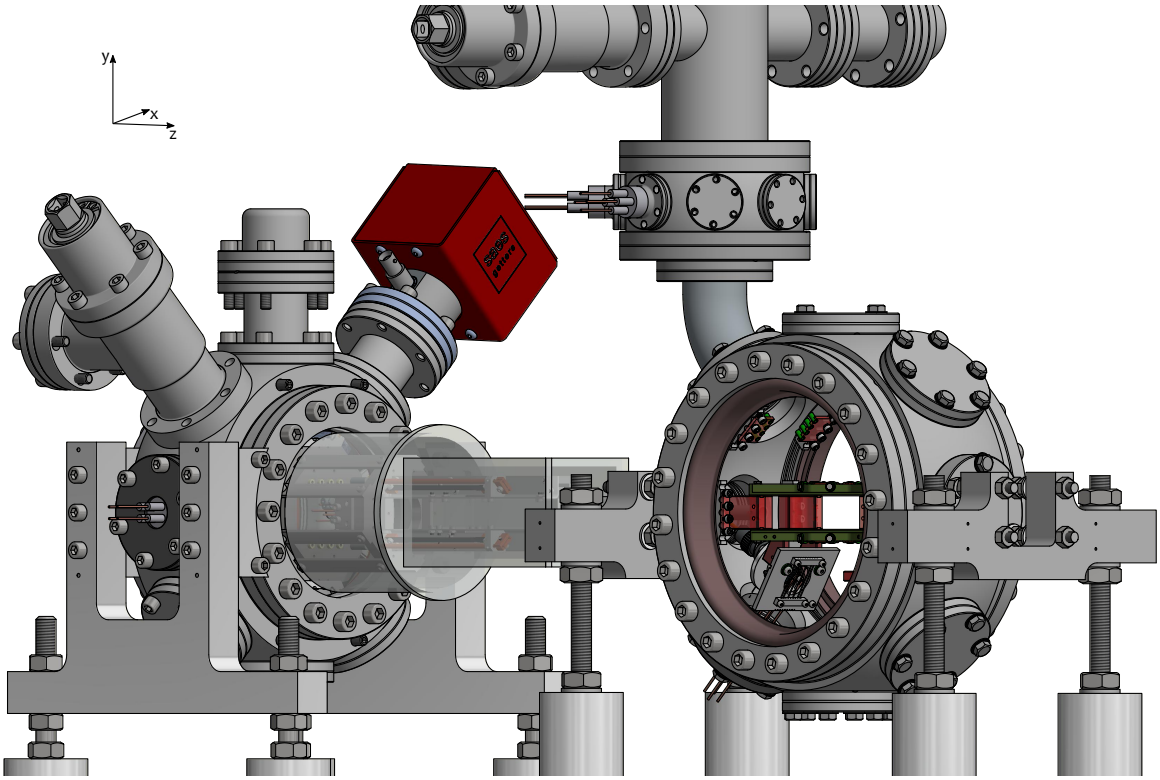

Figure 2.1: CAD model of the complete experiment setup. The setup consists of a two chamber approach including a 2D MOT as a source of cold atoms created in the glass cell. Subsequently, the transversely cold atomic beam is transferred to the science chamber (spherical octagon). An electric field control is mounted inside the science chamber. Each chamber has a vacuum pump, a valve and an ion gauge connected. The mounts on the bottom and the vacuum pump on top are cut off. The magnet coils for creating the magnetic field gradient required for the MOT and the compensation coils are not shown.

dispensers[1] are used for loading the 2D MOT. These small reservoirs are heated with a current of approximately 7 A to sublimate the Yb atoms from the compound form. The small size of the dispensers allow the 2D MOT to be set in glass cell. Moreover, The flux of atoms into the science chamber depends on the intensity of the laser light in the 2D MOT which can be controlled via acousto-optical-modulators (AOMs) or mechanical shutters, hence no mechanical in-vacuo shutters are needed. The flux of atoms during the cycle of an experiment can be switched off reducing distortions of longitudinally hot background atoms. Both chambers are connected via a differential pumping stage to ensure ultra-high vacuum in the science chamber. However, a drawback of the 2D MOT approach is the requirement of relatively high laser power since the broad singlet transition $\Gamma/2\pi = 29.1\,\mathrm{MHz}$ should be saturated for sufficient transverse cooling.

The emission of Yb in the 2D MOT chamber leads to reduction of vacuum pressure which should be prevented from affecting the science chamber. Therefore, the 2D MOT chamber and the science chamber are separated by a differential pumping stage to maintain a high pressure ratio. As it is inefficient to pump one chamber through the differential pumping stage each chamber has a vacuum pump[2] connected. The vacuum pump of the 2D MOT chamber is attached to the sphercial octagon to which the glass cell is mounted while the pump of the science chamber is placed above the chamber in the T-cross configuration. A vacuum pressure of $10^{-11}\,\mathrm{mbar}$ is aimed in the science chamber to achieve sufficient lifetimes of atoms in the MOT. Therefore, the diameter d of the differential pumping stage must be small since the pressure ratio of the chambers scales with d^3 [84]. However, a lower diameter decreases the flux of Yb atoms into the science chamber. As a trade-off, the diameter of the differential pumping stage is chosen $d = 7\,\mathrm{mm}$ with a length 150 mm yielding a pressure ratio of ~ 300 between the chambers. Given the length of the differential pumping stage, the distance of the end of the 2D MOT to the center of the science chamber is only 219 mm. Further, the chosen diameter of the differential pumping stage allows a push and imaging beam along the atomic axis.

We justified the horizontal orientation of the complete setup in contrast to for instance [56] by planning to use a two-color MOT [70] in the science chamber (discussed in detail in section 2.4). The advantage of exploiting the narrow intercombination transition for the MOT in the science chamber is the significantly low Doppler temperature $T_D = \hbar\Gamma_t/2k_B = 4.4\,\mu\mathrm{K}$. However, this comes on the cost of a small capture velocity of roughly 2 m/s. Atoms with that velocity require a traveling time of 30 ms through the differential pumping stage. Hence, the trajectory of the atoms before they arrive in the science chamber is changed discernibly due to gravity and transverse heating. To avoid losses due to these effects a two-color MOT can be implemented

1 Alfavacuo 3mm S-type AS-3-Yb-0500
2 Science chamber: SAES GROUP NEXTorr D500; 2D MOT chamber: SAES GROUP NEXTorr Z200

[70] which increases the capture velocity of the 3D MOT up to roughly 40 m/s. Atoms in these velocity classes are weakly affected by gravity and transverse heating. Thus, we anticipate that the horizontal orientation simplifies optics alignment without the reduction of atom flux in the science chamber.

2.2 2D MOT CHAMBER

In this section, a motivation for the design of the 2D MOT chamber is provided. The design is predominantly worked out by the post-Doc Simon Ball who worked as well on the project during this thesis. However, several design decisions are based on numerical simulations implemented in the scope of the thesis, see chapter 3. The shown magnetic field numbers in this section are based on a PYTHON script written by Simon. The formulas can be found here [85, 86].

Main part of the 2D MOT vacuum system is a double-ended Borosilicat glass cell[3] mounted on a stainless steel spherical octagon[4] of which the two DN100 ports define the symmetry axis. The glass cell consists of a rectangular cuboid with inner dimensions (120 mmx50 mmx50 mm) through which retroreflected MOT beams pass. The connection to the spherical octagon is achieved by gluing the corresponding flange on the cuboid while on the other end a glass-metal transition to a DN16 flange is implemented. The inner part of the 2D MOT chamber is shown in Fig. 2.2 but rotated vertically.

Protecting the glass cell from degradation of the optical access from ytterbium atom deposition due to the low vapor pressure is crucial. It transpires that cleaning the cell is a delicate issue. Evaporating Yb from surfaces requires much higher temperatures than the glass cell would allow. The epoxy glue used for bonding the glass cell prohibits treatment with strong acid to remove Yb from the glass surface. Stainless steel apertures are mounted in front of the emission slit of each dispenser such that the emission angle is constrained to the opposed dispenser, illustrated in Fig. 2.2b, with the emission angle sketched in yellow. Note that this is only true when the 2D MOT is turned off. The 2D MOT force changes the trajectories of the atoms significantly, explained in detail in chapter 3. Additional protection is provided by anti-reflection coated glass plates clamped in between of the apertures. These plates can be easily re-manufactured and replaced in the case of degradation.

Magnetic fields

A cylindrical quadruple magnetic field with a magnetic gradient of approximately 50 G/cm [56] is generated for the 2D MOT by permanent magnets[5]. The magnetic

3 Custom fabrication from JAPAN CELL
4 KIMBALL PHYSICS MCF600
5 ECLIPSE magnets N750-RB

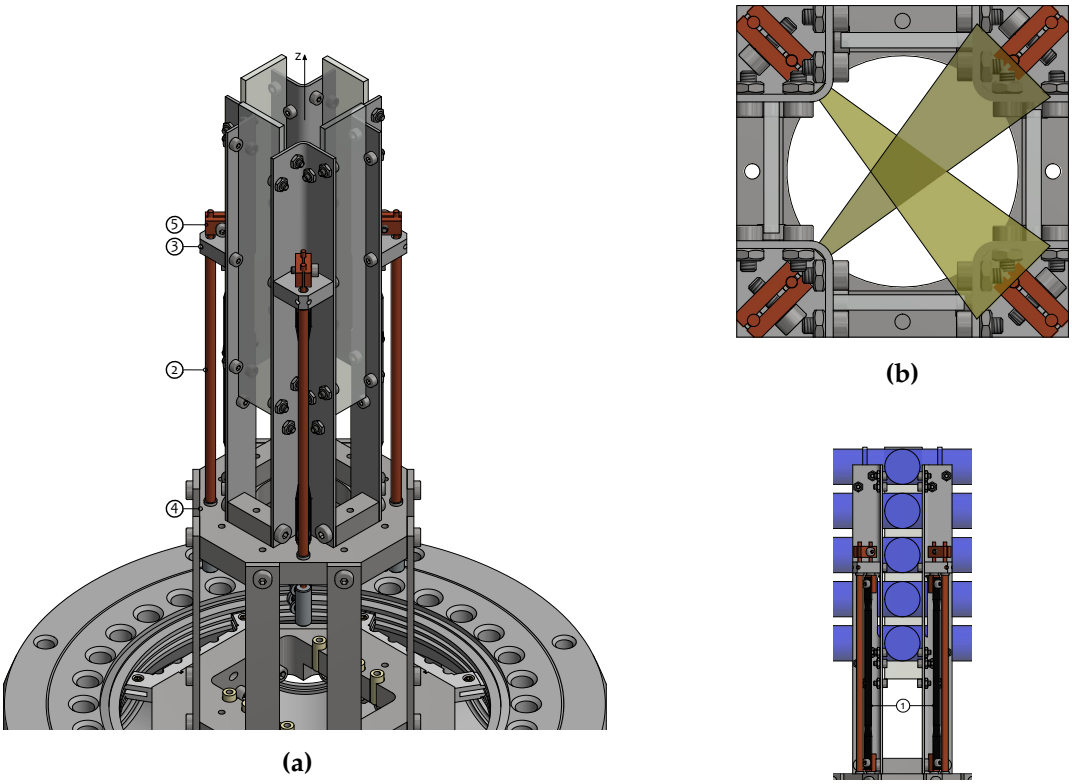

(a) **(b)** **(c)**

Figure 2.2: Internal parts of the 2D MOT chamber. **(a)** The 2D MOT chamber internal parts are rotated vertically. The copper rods ② (in brown) control the vertical and rotational degree of movement of the dispensers ① (in black, see **(c)**) and provide the current supply. **(b)** The top view of the internal parts is displayed with the emission angle of upper left and lower left dispenser set by an aperture. All four dispensers can be operated individually. The apertures are chosen such that the emission does not cover the shielding glass plates. **(c)** The side view of the internal parts is displayed with the front shielding glass plate hidden. The long shielding glass plates allow an elongated cooling volume (blue).

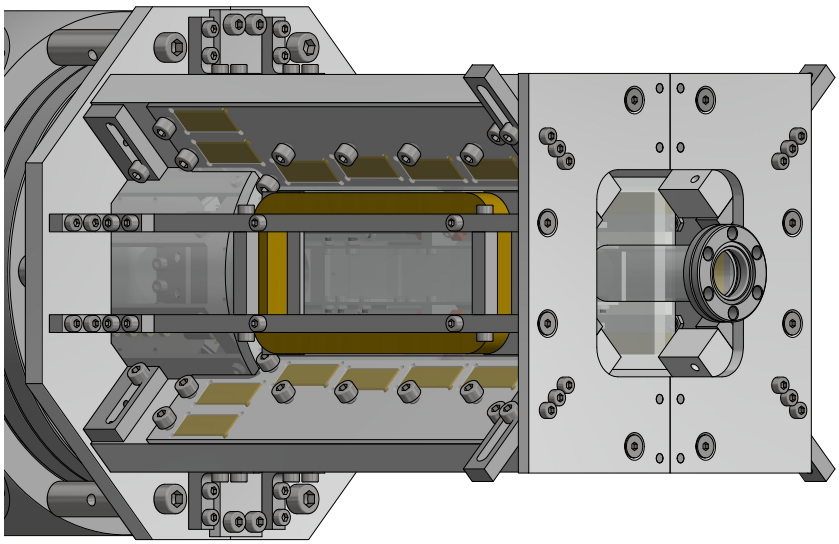

Figure 2.3: CAD model of the magnet cage enclosing the glass cell. The yellow rectangulars represent the permanent magnets. A lid encloses the magnets but is made transparent due to visibility reasons. The yellow rectangular frame illustrates the bias coils for compensating constant magnetic fields.

field design is shown in Fig. 2.3. This solution is motivated by Walraven's group from Amsterdam [77]. Permanent magnets simplify the application of high field gradients which are required due to the broad linewidth of the trapping transition (see chapter 3). The construction is straight forward. It occupies less space and needs no water cooling compared to a set of rectangularly shaped coils operated at high currents. The maximum achievable gradient with this setup is 70.5 G/cm. However, typical gradients are 50 G/cm [56]. A magnetic field gradient 53.4 G/cm is feasible by stacking the magnets. The magnetic field gradient at the center position of the science chamber falls off to 0.076 G/cm. Hence, we expect a minor reduction efficiency of the 3D MOT due to the presence of the 2D magnetic field gradient.

The magnets are made out of Neodymium. Both, Walraven's group [77] and Weidemüller's group from Heidelberg [87] report a typical magnetization of 8.8×10^5 A/m for a single magnet. Each set consists of three stacks magnets to generate a 53.4 G/cm magnetic field gradient.

The magnetic cage can be assembled independently of the 2D MOT chamber and subsequently put over the glass cell. It is mounted on the spherical octagon of the 2D MOT chamber. The magnets are placed in a cross configuration to generate the magnetic field gradient with a zero magnetic field axis along the atomic beam. Out of protection reasons a lid is bolted on top of the stack of magnets (transparent in Fig. 2.3). The position is adjustable in the direction pointing towards the atom beam line. The bias coils used for compensating constant magnetic fields are also mounted on the magnetic cage. Each coil is made out of 60 windings with a 1 mm diameter

Kapton isolated copper wire. Taking into account the distance and the dimensions of the coils it leads to a magnetic field at the symmetry axis of the atomic beam of 2.8 G/A.

2.3 SCIENCE CHAMBER

The central component of the experimental apparatus for Yb Rydberg physics is the science chamber.

The main part of the science chamber is the electric field control. It is mounted by four groove grabbers[6] centrally in the octagon. It is constructed such that the optical access given by the large viewports of the spherical octagon is reduced minimally. The electric field control is discussed in detail in chapter 4.

The science chamber is a stainless steel 316L spherical octagon[7] with six DN40 and two DN160 flange connections and a width of 70.6 mm, shown in Fig. 2.4. The internal structure of the science chamber with illustrated laser beams is shown as well as the configuration of the magnetic field coils (yellow). The DN160 viewports[8] are made out of UV grade fused silica with an anti-reflection coating at 394 nm, 399 nm, 532 nm, 556 nm, 578 nm and 1064 nm for the Rydberg laser, the probe and imaging beam, an optional magic wavelength trap [88], the 3D MOT laser, an optional clock laser [89] and the optical dipole trap laser, respectively. A description of the lasers and their purpose used in the experiment to date can be found in chapter 5. The finite thickness of the viewports allows optical elements to be placed not closer than 50.6 mm along the probe beam axis.

The same coating is applied to a re-entrant UV grade fused silica viewport ③ on the horizontal atomic beam axis used for high-resolution imaging. The viewport has an in vacuum-length of 50 mm and an inner diameter 1.4 inch = 35.6 mm. This allows the insertion of a standard 1 inch THORLABS tube to place a lens close to the trapped atoms. The distance is constrained by the electric field control and is 48 mm. The numerical aperture $\mathrm{NA} = n \sin(\arctan(d/2f)) = 0.233$, with the refractive index n, the focal length $f = 48\,\mathrm{mm}$ and the diameter of the lens d, is limited by the first lens and yields a maximum resolution $R = \lambda/2\mathrm{NA} = 0.86\,\mu\mathrm{m}$ when imaging on the blue singlet transition $\lambda = 399\,\mathrm{nm}$.

The differential pumping stage ④ is highlighted in Fig. 2.4. The outer surface of the tube is welded to the inside of a custom made bellow[9] which connects the glass cell with the science chamber. The bellow is used for stress relief in the glass cell.

6 KIMBALL PHYSICS MCF800-GrvGrb-C01
7 KIMBALL PHYSICS MCF800
8 MPF TECHNOLOGIES Q21173-6
9 KIMBALL PHYSICS

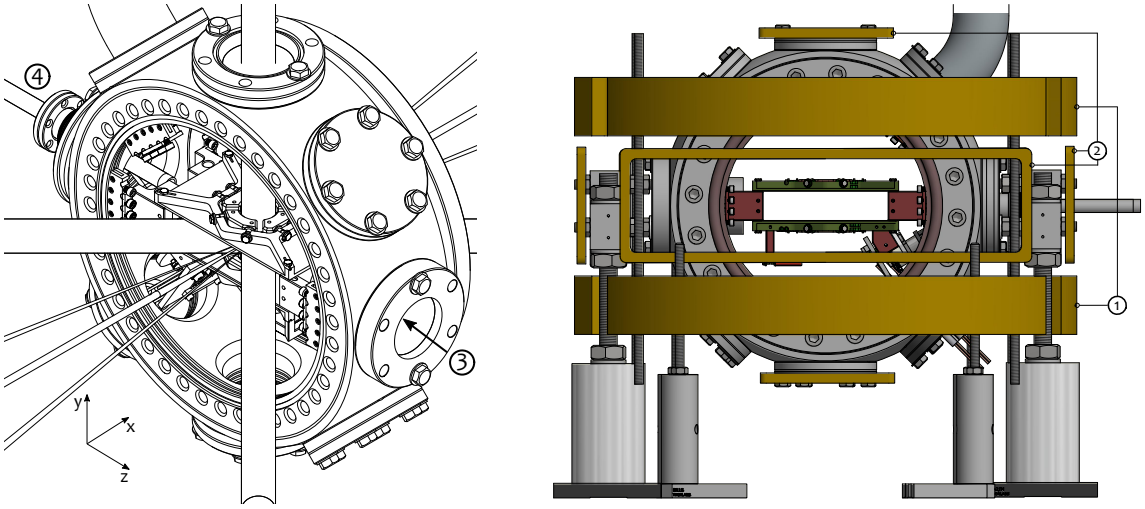

(a) **(b)**

Figure 2.4: CAD Model of the science chamber. **(a)** The science chamber is shown with the internal structure and with the laser beams. The probe (blue), MOT (green) and optical dipole trap beams (red) overlap in the center of the electric field control. The viewport is hidden to make the internal structure more clear. The re-entrant viewport ③ and the differential pumping stage ④ are highlighted. **(b)** The science chamber is shown with the magnetic coils (yellow). For the sake of visibility, the mounts of the bias coils ② are hidden. The MOT coils ① are mounted on THORLABS mounts.

Magnetic fields

The narrow intercombination transition which is used for cooling the atoms in a 3D MOT requires significantly smaller magnetic field gradients compared to the broad singlet transition exploited for initial transverse cooling in the 2D MOT. Based on [56, 70] a gradient 5 G/cm is sufficient to achieve maximum capture velocities. The symmetry axis of the MOT coils ① is aligned with the vertical MOT beam axis. The MOT coils[10] are made of rectangular (4 mm x 4 mm) hollow core (2.5 mm cooling channel) Kapton isolated copper wire. 8 layers of 8 winding turns with an inner diameter 230 mm and an outer diameter 344 mm give magnetic field gradients 10 G/cm, 5 G/cm axially and radially, respectively, at nominal currents of 26 A. The coils are bonded with in-vacuum Araldit F socketing. Holes are bored in the socketing to mount them a at a fixed distance of 96 mm in respect to each other. The lower coil is mounted on the optical table. The compensation coils ② are used for shifting the magnetic field by a constant offset.

2.4 EXPERIMENT SEQUENCE

In this section, the sequence of a future experiment is explained. The author would like to emphasize that the setup of the complete vacuum chamber is not assembled to the submission date of the thesis but this description shall give the reader an overview of the experiment scheme in order to put the technical design in perspective with the physics we have in mind.

The experiment starts with loading atoms in the 2D MOT via the broad $\Gamma/2\pi =$ 29.1 MHz singlet transition ${}^1S_0 \rightarrow {}^1P_1$. Four orthogonal pairs of retroreflected, counter propagating laser beams are shone into the glass cell of the 2D MOT chamber. The design of the cooling regions is described in section 3.2. The combination of a two-dimensional quadruple magnetic field and laser light creates a restoring force along the line of the zero magnetic field. Whereas, the velocity along the atomic beam axis is not actively reduced. Hence, two counterpropagating atomic beams travel along the z-direction while being compressed transversely. To gain a quantitative understanding of atom trajectories in a 2D MOT numerical simulations are performed, discussed in chapter 3.

The atoms are transferred to the science chamber through the differential pumping stage. In order to achieve higher loading efficiency the opportunity of implementing a push beam can be realized due to optical access along the atomic beam axis. Indeed, different groups report varying performance of push beams on both the broad 399 nm singlet transition [56] and the narrow 556 nm triplet transition [90].

10 Oswald Elektromotoren GmbH

In the science chamber, the atoms are trapped and cooled in a 3D MOT via the narrow intercombination line. This has the advantage over the singlet transition of a lower Doppler temperature and closed cooling cycle [80]. Specifically, the Doppler temperature of the triplet transition is $T_D = 4.4\,\mu K$ similar to sub-Doppler temperatures achieved with alkali atoms and well suited as a starting point for evaporative cooling. However, the capture velocity in a MOT solely operated at the intercombination line is only $v_c = 2\,m/s$ [80]. Hence, only a small portion of atoms can be trapped but those possess low temperatures.

In order to increase the loading rate and the steady state atom number two methods can be exploited: the light of the triplet cooling laser is spectrally broadened via modulation with an AOM [80] and in addition a two-color MOT can be used [70] The laser frequency can be spectrally broadened by passing the light twice through an AOM. The AOM is modulated rapidly with an alternating frequency. As a consequence, additional frequency components are modulated on the laser, effectively increasing the capture velocity [70, 91]. To increase the loading rate even further the triplet and singlet transitions can be spatially arranged in a core-shell configuration termed as a two-color MOT [70]. The basic idea is to create a shell beam, i.e. a beam with zero intensity in the center, of the singlet transition. This beam is overlapped with the core beam of the triplet transition. Due to the shell singlet transition fast velocity classes are addressed and can be cooled. Subsequently, the atoms enter the core volume of the triplet transition in which they get cooled to significant low temperatures. Hence, this scheme allows to take advantage of both cooling transitions: The singlet transition increases the capture velocity significantly and thus the number of atoms which can be trapped while the triplet transition in the core leads to extreme low temperatures.

In the next step, the atoms are loaded in a far red-detuned, crossed optical dipole trap [41, 92] eventually followed by further cooling techniques in the dipole trap as e.g. evaporative cooling [93]. When the atoms have reached the finale temperature the actual nonlinear quantum optics experiments are performed. Therefore, the dipole trap is positioned in the focus of a single photon probe beam at a wavelength 399 nm and coupled to a Rydberg state by overlapping the probe beam with a strong, counterpropagating control beam at a wavelength $\sim 395\,nm$. Subsequently, the single photons of the probe beam are detected with single photon counter modules. The electric field control allows the ionization of the Rydberg atom. Further on, by means of steering electrodes the ions can be detected on a microchannel plate.

3

TWO-DIMENSIONAL MAGNETO-OPTICAL TRAP

A 2D MOT serves as source of cold atoms for subsequently loading a 3D MOT. Several of the design decisions shown in section 2.2 are based on atom trajectory simulations in a 2D MOT. First, the basic principle of a two-dimensional MOT is explained. This is followed by a description of the technical design of the 2D MOT optics, however not yet assembled to the date of the submission. Third, the results of the simulations are presented.

3.1 PRINCIPLE OPERATION OF A 2D MOT

The basic concept of a 2D MOT is to trap atoms in two-dimensions while the motion in the third dimension is not actively cooled. This allows the creation of a collimated atomic beam as a source of transverse cooled atoms for loading a 3D MOT [94].

A 2D MOT consists of pairs of counterpropagating laser beams in combination with an elongated magnetic quadrupole field which generates a zero magnetic field line. This creates a radial restoring force towards the zero magnetic field line. Atoms entering the cooling volume are compressed radially creating two counterpropagating atomic beams since no cooling force acts in the direction perpendicular to the laser beams.

Atoms entering the 2D MOT cooling volume have to satisfy three criteria in order to contribute to the flux in the science chamber [95]. First, the initial velocity of the emitted atom must be smaller than the radial capture velocity. Second, the cooling time must be long enough such that the divergence of the atomic beam is sufficiently small to exit the differential pumping stage (as presented in chapter 2). And third, the mean free path must be larger or equal to the distance an atom covers in the 2D MOT. Otherwise, the atom is lost from the collimated beam by collisions with hot background atoms. However, this effect is less pronounced in this setup for ytterbium than in alkali atom 2D MOTs since the ytterbium atoms are not loaded from a hot background gas but from a background stream.

A key figure of merit in a 2D MOT is the cooling time which determines the divergence of the atomic beam. Atoms emitted at angles almost parallel to the zero magnetic line – defined as the z-direction – are not sufficiently compressed due to the low exposure time to the cooling light. The cooling time τ is therefore defined as the ratio of the distance z an atom travels in the cooling region and the longitudinal

velocity v_z yielding $\tau = z/v_z$. This pre-filtering of atoms with too high longitudinal velocities leads to a shift of the velocity distribution to values lower than the thermal distribution at room temperature even though no active longitudinal cooling takes place.

3.1.1 *Theoretical Background of a 2D MOT*

In order to understand the operation of a 2D MOT quantitatively a brief introduction to the magneto-optical force acting on the atoms is given. In particular, the differential equation for simulating the atom trajectories in the 2D MOT is determined.

Consider an atom exposed to a light field. The atomic response to the force exerted by photons can be either dissipative or conservative [96]. In a MOT the dissipative force is exploited which stems from absorption and reemission of photons by directing the photon momentum $\hbar\mathbf{k}$ on the atom. However, the incoherent reemission due to relaxation in the ground states takes place in all directions. Consequently, the motion of the atom is reduced at the optical pumping rate.

An optical molasses, i.e. strong damping of atomic motion to equilibrium exhibiting Brownian motion, is generated by exploiting the dissipative force in a directive manner. Consider the one-dimensional case of a two-level atom with energy difference ω_0 between the ground and excited state and a linewidth Γ. The atom interacts with planar waves from both directions at frequency $\omega = kc$ and frequency detuning $\Delta = \omega - \omega_0$. The atom possess thermal energy corresponding to a velocity $v(t)$. In the propagation direction of the laser the atom experience a Doppler shift $kv(t)$. The laser induced coupling of the ground and excited state is characterized by the constant laser intensity I with respect to the saturation intensity I_{sat} of the atomic transition. The ratio is expressed as $s = I/I_{\text{sat}}$. The average force of photons on a moving atom is [97]

$$F = \sum_{j=0}^{N=1} -(-1)^j \frac{\hbar k \Gamma}{2} \frac{s}{1 + I_{\text{rat}} + 4\left(\frac{\Delta + (-1)^j k v(t)}{\Gamma}\right)^2}. \tag{3.1}$$

The case $j = 0(1)$ corresponds to a plane wave traveling in negative (positive) direction. This force is often referred to as radiation pressure force [98].

The dissipative force can be used to reduce the atomic motion and to narrow their velocity distribution. However, it does not confine the atoms spatially. This can be achieved by combining optical molasses with a magnetic field gradient with the strength G. The magnetic field gradient induces a spatial dependent Zeeman shift. Two incident counterpropagating beams with σ^+ and σ^- polarization couple to

different atomic states, hence the dominant force pushes the atoms to the center of the trap. The resulting magneto-optical force is [99]

$$F = \sum_{j=0}^{N=1} -(-1)^j \frac{\hbar k \Gamma}{2} \frac{s}{1 + s + 4\left(\frac{\hbar\Delta + (-1)^j \hbar k v(t) + (-1)^j \mu G x(t)}{\hbar\Gamma}\right)^2}, \tag{3.2}$$

with the magnetic moment $\mu = g_L \mu_B / \hbar$ for the corresponding transition. Here, g_L is the Lande factor and μ_B is the Bohr magneton. The singlet transition $6s^2\ {}^1S_0 \rightarrow 6s6p\,{}^1P_1$ of ^{174}Yb is exploited for the 2D MOT as explained in section 2.4 and the Lande factor reads $g_L = 1.035$ [100].

In practice, the intensity I is spatially dependent, i.e. $I = I(x)$, and follows a Gaussian profile (here in one-dimension) yielding

$$s = \frac{I_0}{I_{sat}} e^{-\frac{2x(t)^2}{w_0^2}} = s_0 e^{-\frac{2x(t)^2}{w_0^2}}, \tag{3.3}$$

with the peak intensity I_0 of the incident laser, the saturation intensity of the atomic transition I_{sat} and the ratio $s_0 = I_0 / I_{sat}$. In order to calculate atom trajectories Newtons equation of motion in three dimensions are solved. Therefore, the intensity profile must be extended to three dimensions. Furthermore, as explained in the next section 3.2 the optical setup consists of N circular cooling volumes along the atomic beam axis with distance d yielding an intensity profile

$$s_{row} = \sum_{j=0}^{N} s_0 e^{-\frac{2x(t)^2}{w_0^2}} e^{-\frac{2y(t)^2}{w_0^2}} e^{-\frac{2(z(t)-jd)^2}{w_0^2}}. \tag{3.4}$$

By replacing s with s_{row} in equation (3.2) Newtons equation in three-dimensions are obtained and read

$$m_{Yb} \ddot{\mathbf{x}}(t) = \mathbf{F}_{2DMOT} = \begin{pmatrix} F_x \\ F_y \\ 0 \end{pmatrix}. \tag{3.5}$$

The z-component of the force is zero since no active cooling takes place in that dimension. The gravitational force is neglected since the contribution to the trajectory of an atom is minor.

3.2 2D MOT OPTICAL SETUP

As discussed in the previous section 3.1, atoms with too high longitudinal velocity cannot be sufficiently cooled and are filtered out by the aperture of the differential pumping stage. The cooling time along the atomic beam direction can be increased by expanding the cooling volume in z-direction.

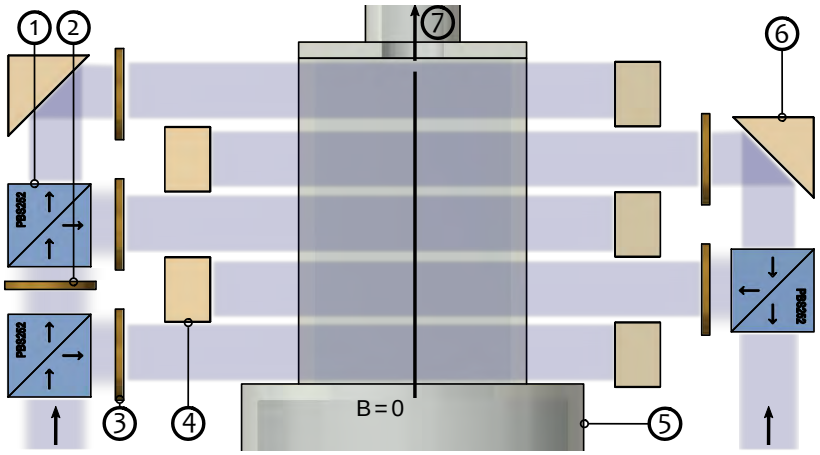

Figure 3.1: Top view of the optical setup of the 2D MOT. The cooling light is split into consecutive cooling regions using polarization optics, i.e. polarizing beam splitters ①, half waveplates ②, quarter waveplates ③ and rectangular prisms ④, ⑥. The Cooling light (blue) is distributed from both sides of the glass cell ⑤. The direction of the differential pumping stage ⑦ and the zero magnetic field axis $B = 0$ is illustrated.

This can be achieved by using either elliptical beams [95, 101, 102] or a row of circular beams [71, 103]. Elliptical beams have the advantage of a continuous cooling region but on the cost of large, often custom-made made optics. Instead, five circular, consecutive cooling regions are chosen, shown in Fig. 3.1. The optics require less space with the additional degree of freedom of adjusting the intensity in each cooling beam. Atoms emitted close to the aperture of the differential pumping stage experience a shorter cooling time. Hence, the atomic beam is less compressed resulting in loss by the aperture. This can be countered by an increased intensity close to the differential pumping stage. The non-cooling area in which the laser beams barely overlap is significantly reduced in this setup compared to [71, 103]. The regions' center is separated solely 20 mm. Hence, we expect a reduction of atom loss due to the decreased discontinuity of the cooling regions.

The cooling light with a diameter of 18 mm is distributed via a PBS ① and circularly polarized by a quarter waveplate ③. Rectangular prisms ④,⑥ are used to retroreflect the light omitting the requirement of quarter-waveplates for reflection due to double-reflection on the prism. Half-waveplates ② allow the adjustment of the intensity in each cooling region.

3.3 ATOM TRAJECTORIES

Numerical simulations of the atom trajectories governed by the differential equation (3.5) are performed. Based on these simulations several measures are made to reduce

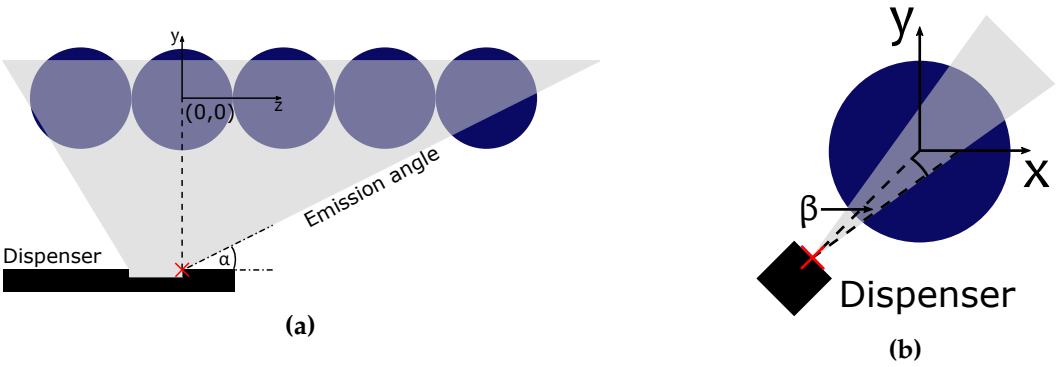

Figure 3.2: Schematics of the setup the simulations are based on. **(a)** The emission angle of atoms out of the dispenser (grey) constrained by the aperture is illustrated in the zy-plane. The five cooling regions are sketched in blue. The center of coordinates is shown. The red cross marks the coordinates $(z, y) = (0\,\text{mm}, -14.44\,\text{mm})$. . **(b)** The same setup is presented but projected on the xy-plane. The red cross marks the coordinates $(x, y) = (-14.44\,\text{mm}, -14.44\,\text{mm})$.

the degradation of optical access of the glass cell due to the coating of ytterbium atoms. Additionally, the simulations serve the purpose to gain an intuitive understanding of the atom trajectories in a 2D MOT which differ significantly from a typical 3D MOT.

The three-dimensional numerical simulations are implemented in MATHEMATICA. The solutions to the ordinary differential equation are obtained for variable initial velocities. The initial spatial position of the atoms is set by the position of the dispenser. Schematics of the setup and the corresponding coordinate system is shown in Fig. 3.2.

The choice of the parameters for the simulations is based on the experimental values from [56]. The magnetic field gradient is $G = 54\,\text{G/cm}$ with a detuning of the singlet transition $\Delta = -1.2\Gamma$. The singlet transition $\lambda = 398.91\,\text{nm}$ with a linewidth of 29.1 MHz is used. Available power for each circular cooling beam in our experiment is estimated to 80 mW with a $1/e^2$-beam diameter $2w_0 = 18\,\text{mm}$ while the saturation intensity of the broad singlet transition is $I_{\text{sat}} = 59.97\,\text{mWcm}^{-2}$. Hence, the ratio of laser intensity and saturation intensity of the singlet transition is $s_0 = 1.34$. The number of cooling volumes in the simulations is chosen as $N = 4$, the fifth cooling volume is dedicated to the atoms traveling in the opposed direction of the science chamber which can be turned with a push beam, therefore not considered in the simulations. The distance of the Gaussian beam centers is $d = 0.02\,\text{m}$.

The capture velocity in one dimension for a Gaussian beam profile with the above mentioned parameters is calcualted to $v_{c,1D} = 39.8\,\text{m/s}$ which is in good agreement with [70].

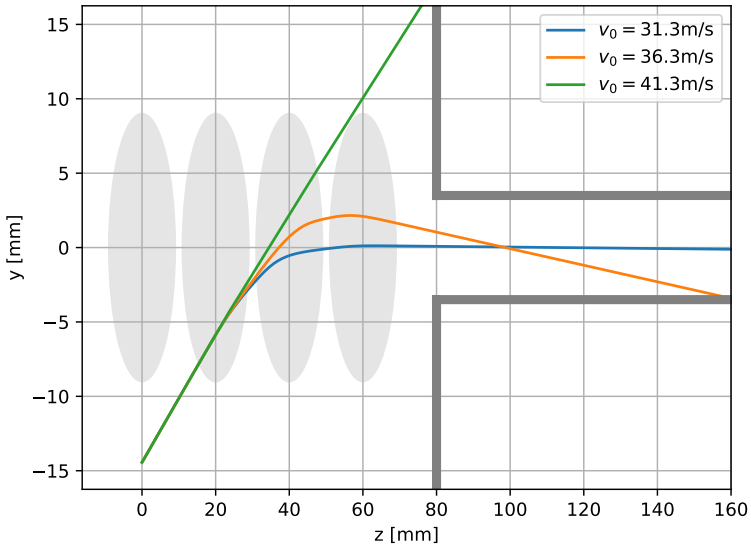

Figure 3.3: Simulated trajectories of Yb atoms projected on the yz-plane. Three different particle trajectories with initial conditions $\mathbf{v}_0 = v_0(1, 1, \cot\alpha)^T$ under a fixed emission angle α are shown. The initial velocity in x-direction is the same as in y-direction due to simplicity. The grey lines indicate the aperture of the differential pumping stage. The circles highlight the cooling regions.

3.3.1 *Emission Aperture*

The dependence of the interaction time of the atoms with the cooling light such that the divergence of the atomic can be compressed sufficiently is shown in Fig. 3.3. The cooling time is reciprocal to v_z, hence atoms emitted almost parallel with respect to the z-direction solely increases the loss rate due to collisions with the collimated atomic beam and degrade the optical access of the glass cell due to deposition.

Here, the emission of atoms with initial conditions $\mathbf{v}_0 = v_0(1, 1, \cot\alpha)^T$ is considered with a fixed angle α and v_0 the remaining degree of freedom. Slow velocities (blue) are sufficiently cooled in the radial direction. Hence, these atoms can be transferred through the differential pumping stage. Atoms with velocities close to the one-dimensional capture velocity $v_{c,1D}$ cannot be compressed enough. Even though they enter the differential pumping stage they are lost on the inner wall. This is caused by the reduction of the intensity due to the Gaussian beam profile. The lower attractive force towards the zero magnetic field line leads to a non-vanishing divergence. Hence, it is crucial to minimize the distance of the regions' center. Velocity classes above $v_{c,1D}$ are affected negligibly by the trapping force (green). These travel straight through the cooling volume.

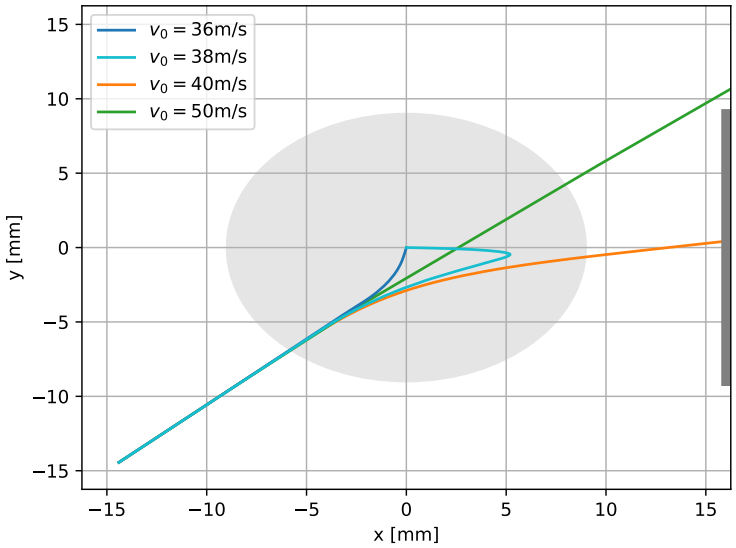

Figure 3.4: Simulated Trajectories of Yb atoms projected on the yx-plane. Four trajectories with initial conditions $\mathbf{v}_0 = v_0(1, \tan(45° - \beta), 0)^{\mathrm{T}}$ with a fixed emission angle β are shown. The velocity in z-direction is chosen to 0 m/s due to simplicity. The trajectories can be classified in three categories. First, atoms that are trapped radially (blue), second atoms whose trajectory is influenced from the MOT force but not trapped (orange) and third, atoms which are too fast to experience the MOT force (green). The grey line indicates the shielding glass plate (see Fig. 2.2a). The circle points out the cooling region.

The shallowest angle in the yz-plane with respect to the z-axis is chosen to $\alpha = 23°$ as a compromise of a large atom number entering the cooling volume and minimizing deposition of Yb on the glass cell.

3.3.2 *Shielding Glass Plates*

Atoms escaping the cooling volume radially can lead to deposition on the glass cell and thus degrading the optical access of the MOT beams. These atom trajectories are investigated in the xy-plane perpendicular to the atomic beam axis in Fig. 3.4.

Due to simplicity the velocity in z-direction is chosen to be 0 m/s. The emission of atoms with initial conditions $\mathbf{v}_0 = v_0(1, \tan(45° - \beta), 0)^{\mathrm{T}}$ is considered while the emission angle β is fixed and v_0 is the remaining degree of freedom. The velocity v_0 of the atoms is step-wise increased starting from below $v_{\mathrm{c,1D}}$. The trajectories can be classified in three categories. First, atoms that are trapped radially (blue). Both velocity components are below the radial capture velocity, hence the atoms are compressed in the center of the of the cooling volume. The second category consists

of atoms which possess velocity components both below and above the radial capture velocity (orange). The component below the capture velocity is reduced by the cooling force while the other component is affected slightly. The trajectory is bend such that these atoms hit the glass cell surface on which the MOT beams incident. As a consequence, the optical access of the glass cell degrades. Indeed, this category exists for any finite emission angles. The third category possess velocities larger than the radial capture velocity (green). Hence, their trajectory is slightly influenced by the trapping force and they travel straight through the cooling volume.

In order to minimize the degradation the aperture is chosen such that the emission angle is maximally $\beta = 3.7°$. However, additional protection is provided by shielding glass pates (grey line) in Fig. 3.4 since the degradation of the glass cell surface due to atoms of the second category is inevitable. These are cheap, easily to fabricate and replace.

4

ELECTRIC FIELD CONTROL

In this chapter the design of the in-vacuum electric field control is discussed. It is motivated from the neighboring experiment in the same group but with several changes due to a different setup. These changes are based on simulations of the electric field at the position of the trapped atoms and particle trajectories onto a microchannel plate[1] (MCP). The first section contains the theoretical background of Rydberg atoms in electric fields. In the following sections the simulations of the electric field and the ion trajectories is presented.

4.1 THEORETICAL BACKGROUND OF RYDBERG ATOMS IN ELECTRIC FIELDS

Frequency shifts of atomic levels due to electrical fields are known as the Stark effect. There is a distinction between the linear and quadratic Stark effect discussed below. Further, the required field for ionization of Rydberg atoms is derived.

4.1.1 *Stark Shift*

The presence of a weak dc-electric field $\mathbf{E}$ interacting with an atom can be treated quantum mechanically by means of time-independent perturbation theory. The complete Hamiltonian of the system reads

$$\mathcal{H} = \mathcal{H}_0 + \mathcal{H}_1, \tag{4.1}$$

with the unperturbed Hamiltonian $\mathcal{H}_0 = -\hbar/(2m)\nabla^2 + V(\mathbf{r})$ and the perturbation $\mathcal{H}_1 = -e\mathbf{E}\cdot\mathbf{r}$, with the mass m and the elementary charge e. Consider that the full solution of the isolated system $\mathcal{H}_0$ is known

$$\mathcal{H}_0 \left|\psi_{0,\mathrm{n}}\right\rangle = E_{0,\mathrm{n}} \left|\psi_{0,\mathrm{n}}\right\rangle, \tag{4.2}$$

1 Hamamatsu F4655-13

with eigenstates $|\psi_{0,n}\rangle$ and eigenvalues $E_{0,n}$. Following standard quantum mechanics textbooks [104–106] the eigenvalues E_n of the complete system in second order perturbation theory reads

$$E_n = E_{0,n} + \epsilon_{1,n} + \epsilon_{2,n} \tag{4.3}$$

$$= E_{0,n} + \langle\psi_{0,n}|\mathcal{H}_1|\psi_{0,n}\rangle + \sum_{k,k\neq n} \frac{|\langle\psi_{0,n}|\mathcal{H}_1|\psi_{0,k}\rangle|^2}{E_{0,n} - E_{0,k}} \tag{4.4}$$

Here, it is assumed that the eigenvalues $E_{0,n}$ are non-degenerate. The first order term $\epsilon_{1,n}$ does not contribute to the energy shift due to symmetry arguments [104]. Hence, the energy shift of the complete system is proportional to $|\mathbf{E}|^2$ with respect to the unperturbed energy $E_{0,n}$. This is known as the quadratic Stark effect.

In a more intuitive picture, the quadratic Stark effect stems from an induced electric dipole moment. It can be shown that atoms which have no l-degeneracy do not possess an electric dipole moment [104]. The applied electric field $\mathbf{E}$ induces an electric dipole moment of the form $\mathbf{p} = \alpha\mathbf{E}$, with the polarizability α. Hence, the interaction potential reads $V = -1/2\mathbf{p}\cdot\mathbf{E} = -1/2\alpha|\mathbf{E}|^2$.

However, the linear Stark effect is a quantum mechanical effect stemming from the degeneracy of the angular quantum number l. In order to treat that problem mathematically the above mentioned perturbation theory fails since terms in equation (4.4) diverge. Therefore, time-independent degenerate perturbation theory is applied. Following that approach leads to the energy E_n depending linearly on the applied electric field $|\mathbf{E}|$ [104]. Thus, the electric field lifts the degeneracy of the angular quantum number l due to the perturbation of the electric field to the Coulomb potential of the core. The linear Stark effect is mainly observed in the hydrogen atom since it requires that the angular quantum number degeneracy breaks by the external electric field while in other atoms internal fields due to higher electron numbers already break that symmetry. This becomes important for Rydberg atoms since they can be treated as hydrogen-like atoms.

4.1.2 *Ionization of Rydberg States*

Since Rydberg atoms are states with a valence electron in a high principle quantum number n their interaction with an electric field can be treated in a classical manner. The interaction of the highly excited electron and the core is described by the Coulomb potential

$$V_{\text{Coulomb}}(r) = -\frac{e^2}{4\pi\epsilon_0 r}, \tag{4.5}$$

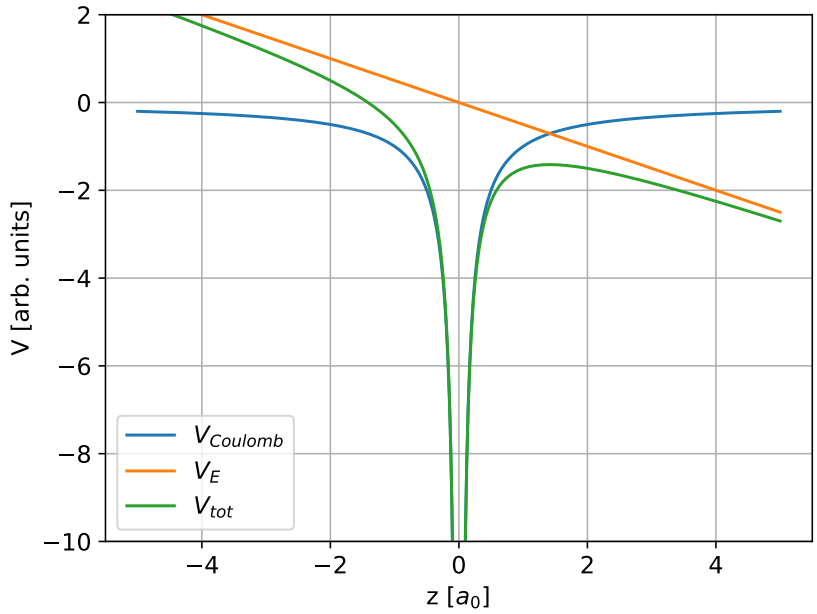

Figure 4.1: Potential of the Rydberg electron. The potential of the electric field V_{E}, the coulomb potential V_{Coulomb} and the superposition V_{tot} is shown.

with the vacuum permittivity ϵ_0. The potential of the external dc-electric field assumed to point in the z-direction is of the form

$$V_{\mathrm{E}} = -e|\mathbf{E}|z. \tag{4.6}$$

Hence, the total potential of the Rydberg electron is a superposition of the Coulomb potential and the potential of the electric field

$$V_{\mathrm{tot}}(r) = -\frac{e^2}{4\pi\epsilon_0 r} - e|\mathbf{E}|z, \tag{4.7}$$

shown in Fig. 4.1. Only Rydberg states with an energy lower than the total potential are classically bound.

Ionization takes place if the binding energy of the Rydberg electron is larger than the total potential. The binding energy of the Rydberg electron is $E_{\mathrm{B}} = -R_{\mathrm{y,atom}}/n^{*2}$, with the Rydberg constant $R_{\mathrm{y,atom}}$ for the specific species and the effective principal quantum number $n^* = n - \delta_{\mathrm{nlj}}$, where δ_{nlj} is the quantum defect, which takes into account that the core of the Rydberg atom differs from the hydrogen atom. The total potential possess a local maximum which is determined by

$$z_{\mathrm{local,max}} = \sqrt{\frac{e}{4\pi\epsilon_0|\mathbf{E}|}}. \tag{4.8}$$

Putting this together, the condition for ionization reads

$$E_{\mathrm{B}} \geq V_{\mathrm{tot}}(z_{\mathrm{local,max}}) \tag{4.9}$$

and yields the required electric field

$$|\mathbf{E}| \geq \frac{\pi\epsilon_0}{e^3}\frac{R_{\mathrm{y,atom}}^2}{n^{*4}}. \tag{4.10}$$

In particular, the Rydberg constant for Yb is [67]

$$R_{\mathrm{Yb}} = R_{\mathrm{y}}\frac{m_{\mathrm{Yb}}}{m_{\mathrm{Yb}} + m_{\mathrm{e}}} = 10\,973\,696.959\,\mathrm{m}^{-1}, \tag{4.11}$$

with the Yb mass m_{Yb}, the Rydberg constant R_{y} and the mass of the electron m_{e}. The effective principal quantum number for the $6sns\ {}^1S_0$ series with $23 \leq n \leq 80$ is approximately

$$\begin{aligned} n^* &= n - \delta_{\mathrm{n00}} \\ &= n - \left(\delta_0 + \frac{\delta_2}{(n-\delta_0)^2} + \frac{\delta_4}{(n-\delta_0)^4}\right), \end{aligned} \tag{4.12}$$

with $\delta_0 = 4.278\,337$, $\delta_2 = -5.625$ and $\delta_4 = 91.65$ [67].

4.2 ELECTRIC FIELD CONTROL DESIGN

The large polarizability of Rydberg atoms offers strong interactions with surrounding atoms. However, the high sensitivity requires precise control of any external fields in order to avoid line broadening and dephasing of the Rydberg states. Hence, shielding of stray fields is one main purpose of the electric field control design. Furthermore, any dc-electric field applied to the atom induces a Stark shift and splitting of the energy levels. The design used in this experiment offers compensation of energy shifts caused by dc-electric fields. The possibility to ionize the Rydberg atoms in addition with the detection on a MCP enables the monitoring of the number of Rydberg atoms which provides diagnostics and data acquisition for better control of the experiment. In addition, the ionization ensures that no atoms remain in a Rydberg state at the start of a following experiment.

The initial design of the electric field control is established in the scope of Johannes Schmidt's master thesis [107] and motivated by the design from Robert Löw [108]. The developed design for this experiment is shown in Fig. 4.2. Large grounding plates (dark green, 100 mm × 55 mm × 2 mm) shield the atoms from stray fields. However, sufficient optical access for 18 mm MOT beams is ensured. The Löw configuration of the electrodes ①-⑧ allows compensation of electric field gradients in any direction. The steering electrode ⑨ is used to guide the ionized Rydberg atoms on the MCP (A) which is held at a high, total negative voltage of −2.5 kV. In order to reduce the stray fields of the MCP a mesh (B) consisting of six stainless steel wires with diameter 500 µm is mounted between the center of the electric field control and the MCP. All

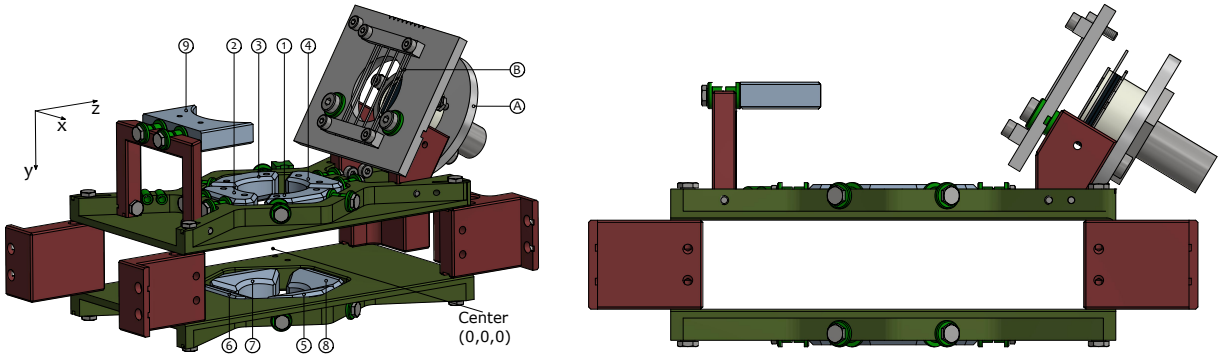

(a) **(b)**

Figure 4.2: CAD model of the Electric field control design. It is shown **(a)** from an angled view and **(b)** from the side. In light green the ceramic components are shown. All other pieces are made out of stainless steel 316L. The compensation and steering electrodes are highlighted in light blue.

electrodes are electrically decoupled from the grounding plate by ceramic components (light green) and mounted with M2 srews to the field plates. Kapton isolated copper wire connects the electrodes to electrical feedthroughs.

The chosen material of the electric field control is stainless steel 316L due to its low out-gassing rate and low magnetization.

4.3 ELECTRIC FIELD SIMULATIONS

The presented design is based on electric field simulations which verify that the stray fields mainly generated by the MCP are sufficiently low.

The simulations of the electric field and the ion trajectories (section 4.4) are calculated with the software program SIMION 8.1. It is an electron and ion optics program suitable for electric and magnetic field calculations, ion trajectory calculations and more. Any geometry modeled in a CAD file can be imported by SIMION. The software uses finite difference methods to find solutions to the required differential equations. In particular, the Laplace equation $\nabla^2\phi = 0$ with the potential ϕ in electrostatic fields is solved under Dirichlet boundary conditions in a finite volume. Due to computational time constrains the discretization is limited to volumes of $(200\,\mu m)^3$.

The electric field simulations are shown in Fig. 4.3. Each figure contains the total electric field strength cut through the center in the respective $xy-, xz-, yz-$plane. The center point of the electric field control is defined as the position of the atomic cloud trapped in the MOT. Three different cases of stray fields at the center are discussed in which it is shown that a homogeneous electric field can be generated with the presented design of the electric field control. The first row highlights the stray fields generated by the MCP. Due to the high total supply voltage of 2.5 kV

a grounded mesh is placed in front of the MCP in order to reduce the stray field. It transpires that charging the mesh slightly positive with 2.48 V leads to further reduction of the MCP stray fields (second row). By adjusting the voltage of the compensation electrodes typically in the range of 10 mV-100 mV [107] the electric field gradient can be further flattened. With the available voltage source[2] compensation of dc-electric fields down to $10\,\mathrm{V}/(2\cdot 10^{16}\,\mathrm{bit}) = 153\,\mu\mathrm{V/bit}$ resolution could be in principle achieved. The electric field strength and the homogeneity of the electric field must be compared to the induced Stark shift of a Rydberg state $\Delta_{\mathrm{Stark}} = 1/2\alpha E^2$ with the polarizability α of Yb. To the authors knowledge, so far dipole-dipole and quadrupole-quadrupole interactions between pairs of Rydberg atoms for Yb are calculated [52] but the polarizability of Yb for a specific Rydberg state is not published. Therefore, as a reference, the Stark shift of a Rb Rydberg state excited to $n^* \simeq 100$ is used which is roughly $\Delta_{\mathrm{Stark}} \simeq 100\,\mathrm{Hz}$ for an external field $10^{-5}\,\mathrm{V/mm}$ [109]. The third row shows the electric field generated by applying a voltage of 500 V to the ionization electrodes ⑥,⑧ which is limited by the available power supply[3].

The maximum applicable voltage of 500 V sets the lowest principle quantum number n possible to ionize. The electric field generated at the center by applying 1 V to the electrodes is calculated with SIMION:

Electrode ⑥,⑧ positive:

$$E(U) = 0.0155/\mathrm{mm}\cdot U[\mathrm{V}], \tag{4.13}$$

Electrode ①,③ positive, electrode ⑥,⑧ negative:

$$E(U) = 0.0352/\mathrm{mm}\cdot U[\mathrm{V}], \tag{4.14}$$

Electrode ①-④ positive, electrode ⑤-⑧ negative:

$$E(U) = 0.0705/\mathrm{mm}\cdot U[\mathrm{V}]. \tag{4.15}$$

The required electric field to ionize a Rydberg state with priniciple quantum number n is described by equation (4.10). In Fig. 4.4 the dependency of the ionization field on the principle quantum number is shown. The maximum electric field at the center is $E_{\mathrm{max,ion}} = 7.75\,\mathrm{V/mm}$. Thus, the lowest Rydberg state possible to ionize is $n = 50$.

4.4 ION TRAJECTORY SIMULATIONS

The position of the MCP is chosen such that ionized Rydberg atoms can be detected on the MCP and is verified by ion trajectory simulations.

In order to verify the ionization of Rydberg states experimentally the ions are detected on a MCP. By ramping up the voltage of electrodes ⑥,⑧ a sufficient electric field strength in the center of the field control is created to ionize Rydberg states.

2 MEASUREMENT COMPUTING USB3112
3 APPLIED KILOVOLTS HP0.5PAA025

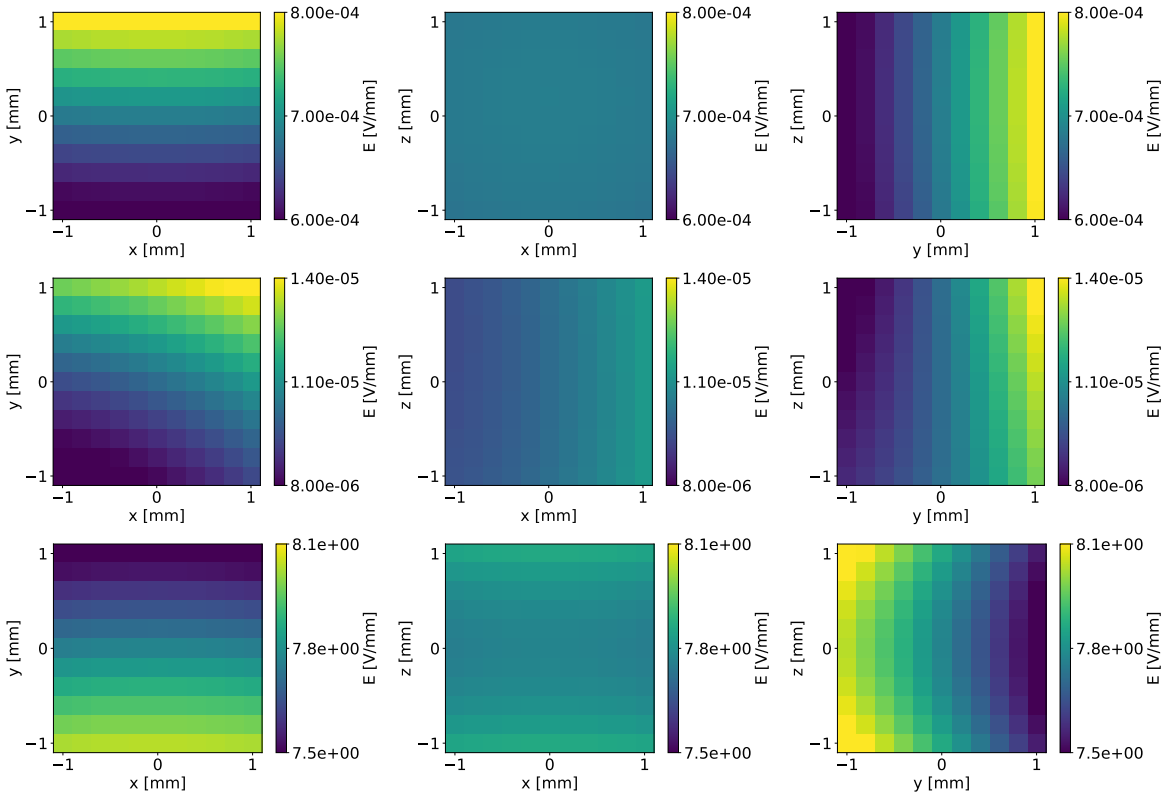

Figure 4.3: Electric field simulations on a grid with discretization 0.2 mm. The **first**, **second** and **third column** contains a cut through the **xy**-plane, **xz**-plane and **yz**-plane of the total electric field, respectively. **First row:** The electric field of the MCP at the position of the atomic cloud is shown. **Second row:** By applying a small positive voltage 2.48 V to the mesh in front of the MCP, the electric field can be reduced down 10^{-5} V/mm. **Third row:** The electric field for maximally applied voltage of 500 V on the electrodes ⑥,⑧.

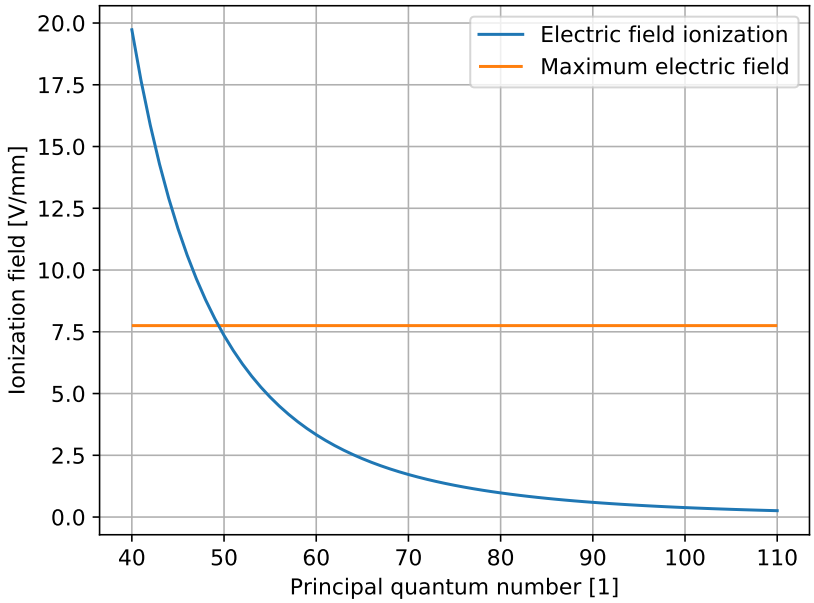

Figure 4.4: Required electric field for ionizing Rydberg states with principle quantum number n. The constant (orange) line corresponds to the maximum electric field generated at the position of the atoms with the available power supplies.

Subsequently, the ions are accelerated vertically upwards. Since the MCP is not directly in line-of-sight to the atomic cloud the ions are deflected on the MCP by a steering electrode (⑨ in Fig. 4.2) set to 310 V. Even though the MCP is highly negatively charged, hence attracts the ions, a steering electrode is required due to the electric field shielding of the MCP.

The ion trajectory simulations are examined with SIMION, shown in Fig. 4.5. An atomic cloud with spherical radius 500 µm and equally distributed atoms inside the sphere is positioned in the center of the electric field control. An initial temperature of 10 µK of the atoms is assumed which is slightly higher than the Doppler temperature of the narrow triplet transition exploited to magneto-optically trap the atoms. This leads to an initial velocity approximately 0.1 µm/µs. A standard deviation of 0.4 µm/µs is assumed.

The voltage of electrodes ⑥,⑧ is set to maximum 500 V while the voltage of electrodes ①,③ is set to −10 V. A negative voltage of −10 V is chosen to expand the atomic cloud during the time of flight vertically upwards such that the ions hitting the MCP are distributed equally over the whole area. Thus, the lifetime of individual microchannels can be extended.

The commitment to place a mesh in front of the MCP is necessary to reduce stray fields but has the consequence of lower detection efficiency. By placing an obstacle in the form of six wires in front of the MCP the cross section effectively decreases since ions can be lost on the wires. Thus, the stray field reduction comes on the cost of

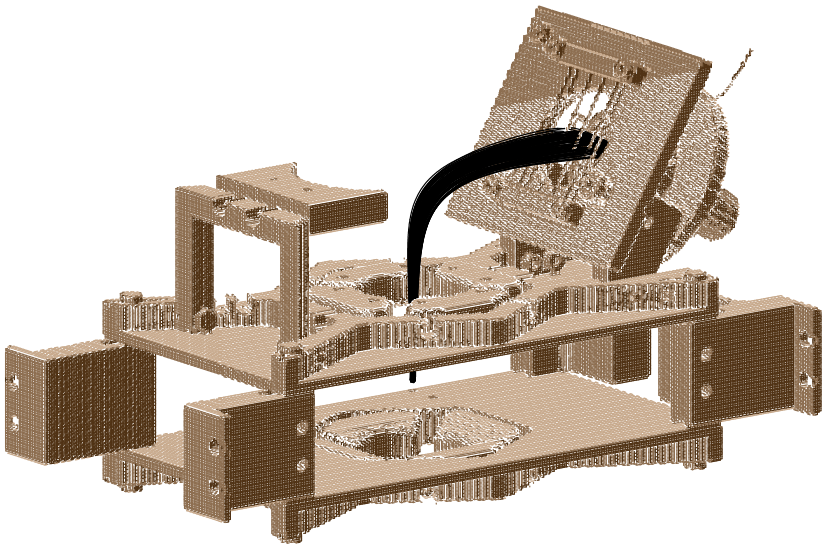

Figure 4.5: Simulated ion trajectories steered on the MCP. A filled sphere of radius 500 µm with 1000 ions is positioned in the center of the electric field control. An ionization voltage 500 V is applied to the base electrodes ⑥,⑧ accelerating the ions vertically upwards. The steering electrode ⑨ is set to 310 V deflecting the ions on the MCP. In order to reduce the loss of ions on the mesh it is ramped up from 2.48 V (see Fig. 4.3) to 30 V.

efficiency decline. This is visualized in Fig. 4.6a where the orange stripes are the ions lost on the mesh. However, the loss of efficiency can be countered by ramping up the voltage on the mesh to roughly 30 V simultaneously with the ionization electrodes. Doing that results in a reduction of particles lost on the mesh from 9.9 % with a grounded mesh to 7.5 % with 30 V applied to the mesh. Nevertheless, a reduction of ion loss can be observed one has to keep in mind that these are numerical simulations. In practice, the electric fields can differ slightly by non-perfect surface machining, the copper wires attached to the electrodes, the glass ceramics and more influences. Hence, the applied voltage on the mesh must be optimized later on experimentally but the simulations provide a ballpark number as a starting point.

It turns out that the presence of the mesh has a positive outcome in terms of a lensing effect leading to a spreading of the ion beam on the MCP. This is shown in Fig. 4.6b. Since the focal point is in front of the MCP the ion beam diverges before hitting the MCP. Therefore, not only a single microchannel is hit but the ions get distributed over the area of the MCP, hence increasing the lifetime of this device. However, the effect of the mesh only holds in the horizontal direction but the vertical direction of the ion beam can be adjusted by varying the voltage on the steering electrode.

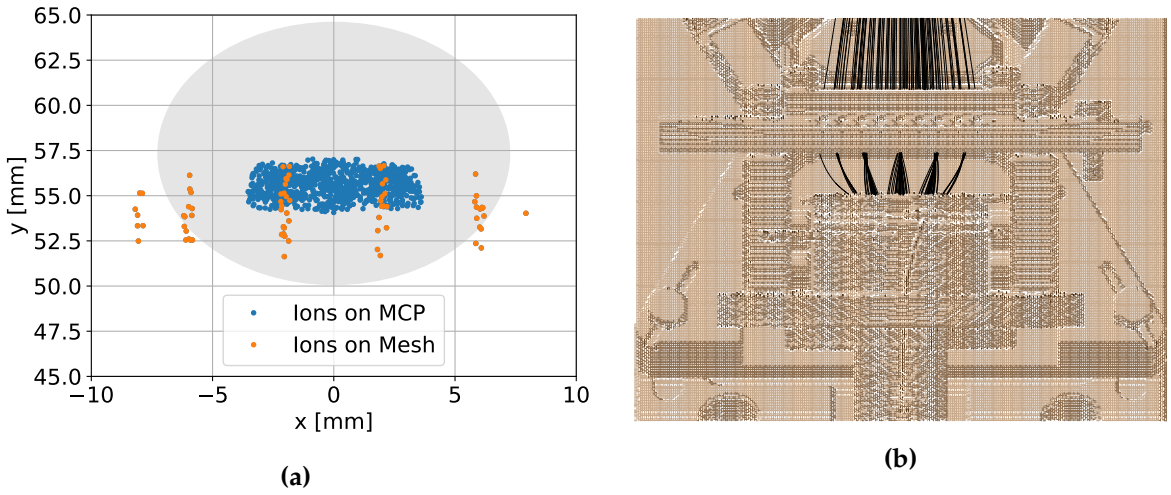

Figure 4.6: Simulated ion trajectories visualizing the influence of the mesh. **(a)** The cross section of the MCP is illustrated in grey. Ions which are detected from the MCP are colored in blue while ions lost on the grid are marked in orange. **(b)** The lensing effect of the mesh is shown due to a potential difference of the MCP and the mesh.

5

CHARACTERIZATION OF THE LASER SYSTEM

This chapter provides an overview of the overall laser setup for the new Yb experiment with a description of each part of the laser system. In particular, in the framework of this master thesis the focus is placed on the setup of three lasers independently coupled to a high-finesse, ultrastable laser cavity. A detailed characterization of the cavity setup is provided, followed by an analysis of the obtained sub-100 Hz beat note linewidth of two lasers simultaneously locked to the cavity.

5.1 COMPLETE LASER SETUP

The laser system consists of six commercial TOPTICA lasers which are specified with their names, wavelength and purpose in table 5.1. The master laser is the core laser in this experiment since it is used as a frequency reference for the DL1,2 and the MOT cooler by means of offset-locking [110]. The frequency of the master laser itself is stabilized to a high-finesse reference cavity. The 3D MOT laser is utilized for cooling the atoms in the science chamber and stabilized to the same reference cavity. The MOT cooler is used for initial cooling in the 2D MOT chamber and in a core-shell-MOT configuration as the shell beam to increase the capture velocity [70]. In addition, it is eventually used for a push beam to increase the flux into the science chamber. The Rydberg laser and the DL1,2 are used in combination to couple the atoms from their ground state to the Rydberg state by a two-photon transition. The Rydberg laser is used as the strong control laser, section 2.4, to excite the atoms from their intermediate state into one state in the Rydberg manifold while the DL1,2 are used as weak probe beams to couple the ground state and the intermediate state. DL1,2 are further used for imaging the atomic cloud to obtain information about the atomic cloud density and temperature. The Rydberg laser is the third laser which is frequency stabilized to the high-finesse reference cavity.

In Fig. 5.1 the laser layout is shown. The overall beam height is chosen to 5 cm except of the 3D MOT laser since it is equipped with a closed-loop cooler for thermal stability in terms of a plumbed cooling plate below the laser (2.5 cm thickness). The height of the optics used for coupling in the cavity is chosen to 12.7 cm due to the height of the cavity mirrors. All lasers are connected to a wavemeter[1] for wavelength

1 HIGH FINESSE WS-5

Table 5.1: Overview and description of the lasers used in the experiment. All lasers are commercial tunable diode lasers (DL) from TOPTICA. The SHG series consists of a resonant frequency doubling stage, partly in combination with a high power tapered amplifier (TA).

NAME	LASER	WAVELENGTH	PURPOSE
Master laser	DL-SHG pro	798 nm, 399 nm	Frequency reference
Rydberg laser	TA-SHG pro	790 nm, 395 nm	Rydberg excitation
3D MOT laser	TA-SHG pro	1112 nm, 556 nm	Cooling
MOT laser	TA-SHG pro	798 nm, 399 nm	Cooling, push beam
DL 1	DL pro	399 nm	Probing, imaging
DL 2	DL pro	399 nm	Probing, imaging

determination with an accuracy of below 1 pm. The wavelength of the SHG lasers is measured by the seed laser in the infrared.

The beams of the MOT cooler and the DL1,2 are overlapped with the master laser for offset locking. The offset lock of the MOT cooler is performed on the infrared output of the diode laser while DL1,2 are locked in the near ultra-violet. The overlapped beams are focused on a fast ac-photodiode[2]. The photodiode signal is further processed to an electronic board[3] which realizes a digital-phase-locked loop [110]. Hence, the lasers are not only frequency stabilized but also phase stabilized in reference to the master laser. AOMs[4] are used for fast intensity switching. Further on, the light is coupled into fibers and transferred to the experiment table. The optical fibers deliver a clean Gaussian mode to the experiment. Additionally, they have the advantage of decoupling the laser table from the experiment table, i.e. any drifts of the optical tables in respect to each other do not affect the alignment on the experiment table.

The frequency doubled light of the 3D MOT laser is used in an AOM double-pass configuration [111] in which the laser light travels twice through the AOM[5]. By applying several rf-frequencies to the AOM additional frequency components can be produced to effectively increase the capture velocity via the spectrally broadened laser light, see section 2.4. At this point this is not realized yet, but motivated from [56, 70, 80].

The frequency doubled light of the MOT cooler is split into three branches. The light of the main branch (transmitted on the first PBS) is used for the 2D MOT transferred

2 HAMAMATSU PHOTONICS G4176-03
3 ANALOG DEVICES AD4007
4 GOOCHE & HOUSEGO AOM 3200-129
5 GOOCHE & HOUSEGO AOM 3080-125

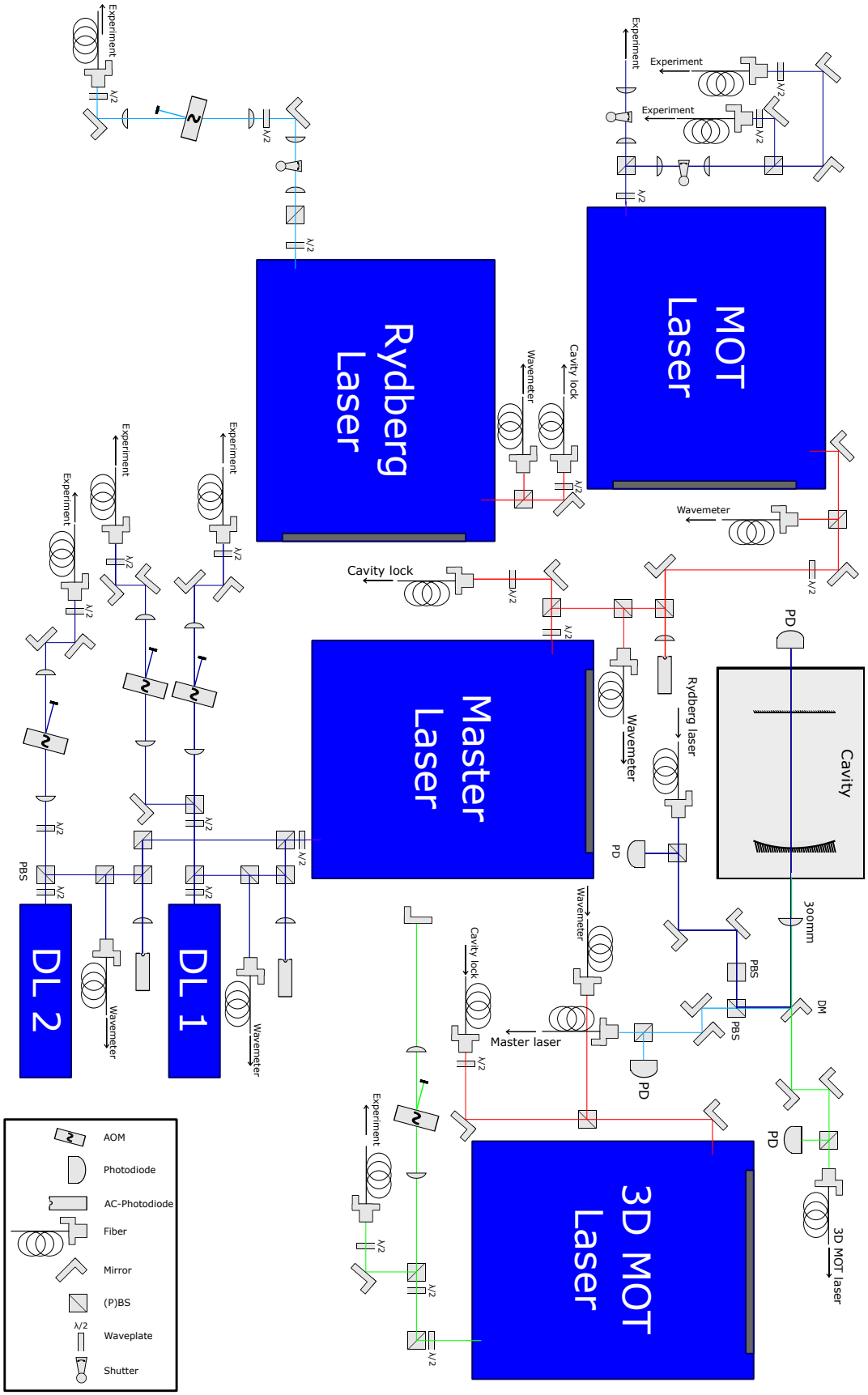

Figure 5.1: Setup of the laser table. Table 5.1 contains the specifications of the lasers used in this experiment. A legend of the optical components is placed in the lower left corner. The dichroic mirror separating the $\sim 790\,\mathrm{nm}$ and the $1112\,\mathrm{nm}$ light is marked as DM.

in free space from the laser to the experiment table. The second branch is used for the two-color MOT in the science chamber, see section 2.4. This is anticipated to demand less power, therefore the light is coupled into a fiber. The last branch is eventually used for a push beam. The intensity of the MOT cooler is controlled solely with a mechanical shutter yielding switching times of approximately 100 µs.

The Rydberg laser has one branch which is used for exciting the Rydberg states. It requires high switching times ~ 30 ns in regards to the intensity. Hence, an AOM is utilized.

The infrared output of the master, Rydberg and 3D MOT laser are coupled into fiber EOMs[6] with a power of roughly 1 mW. It is crucial to place a $\lambda/2$-waveplate in front of the fiber EOMs in order to match the polarization of the laser with the electric field of the EOM. In particular, a detailed description of the cavity setup is given in section 5.2.2.

5.2 STABILIZATION OF THE LASER SYSTEM

The output frequency of a laser is not monochromatic, neither is it constant over time but it fluctuates around a mean value due to noise. In addition, the mean value itself may walk randomly as well. Furthermore, lasers exhibit also intensity noise resulting in a fluctuation of the output power. The noise is basically caused by changes in the ambient temperature, pressure, vibrations or fluctuations of the active medium of the laser. The noise can be classified in two categories, namely white noise, i.e. frequency independent noise, which stems from quantum fluctuations and $1/f$-noise which is caused by technical noise sources [112].

In order to stabilize the frequency of a laser a frequency reference is required which may be provided by a stable optical resonator or an atomic resonance [112]. Subsequently, an error signal is generated which is proportional to the deviation of the laser frequency from the reference. In other words, a dispersive error signal with a zero-crossing at the frequency reference is used as feedback to the laser. This error signal is produced by a phase modulation technique, known as the Pound-Drever-Hall (PDH) technique (see section 5.2.4). Fast frequency drifts are compensated by the current of the diode laser while the piezo element compensates slow drifts.

With a high-finesse cavity a stable and narrow laser linewidth can be achieved for any optical wavelength. Furthermore, in contrast to an atomic resonance, no limitation of the linewidth is set by the natural lifetime of the transition. However, the cavity has to be well isolated from distortions as vibrations, acoustics and temperature changes caused by the surrounding.

6 EOSpace phase modulator

5.2.1 *Theoretical Background of Laser Stabilization*

In this section the basic mathematical formulas of optical resonators and the derivation of the PDH error signal are described. These equations are later used for explaining the obtained experimental data.

Optical Resonators as Frequency Filters

A cavity comprises, in the simplest case, two planar mirrors which confine light spatially and temporally. Hence, a cavity is characterized by the degrees of spatial and temporal confinement of the light which are represented by the free spectral range $\Delta\nu_{\mathrm{FSR}}$ and the finesse $\mathcal{F}$, respectively [113]. To examine the modes of a cavity, in the simplest case, constructed of two planar mirrors and without loss consider a monochromatic wave with frequency ω

$$E_{\mathrm{in}}(r,t) = \mathrm{Re}\left[E_0(r)\mathrm{e}^{\mathrm{i}\omega t}\right], \tag{5.1}$$

with the complex amplitude $E_0(r)$ satisfying the Helmholtz equation

$$\nabla^2 E_0(r) + kE_0(r) = 0 \tag{5.2}$$

and $k = \omega/c$. The resonator modes fulfill the boundary condition of the transverse component of the electric field being zero at the mirror surfaces $z_{1,2} = 0, L$, where L is the length of the cavity. The solution to this differential equation is a standing wave $E_0(r) = E_{\mathrm{amp}}\sin(kz) = E_{\mathrm{amp}}\sin(\pi qz/L)$, with $q \in \mathbb{N}$ satisfying the boundary conditions. It follows that the frequencies are constrained to discrete values. The free spectral range is defined as the distance in frequency space of the adjacent resonances

$$\Delta\nu_{\mathrm{FSR}} = \frac{c}{2L} \tag{5.3}$$

and is only determined by the length L of the cavity.

The finesse of the cavity is defined as the ratio of the free spectral range $\Delta\nu_{\mathrm{FSR}}$ and the full-width-half-maximum (FWHM) $\delta\nu$ of a transmission peak. Under the assumption of high mirror reflectivity $R \gg 1 - R$ the FWHM reads $\delta\nu = \Delta\nu_{\mathrm{FSR}}/(\pi(1-R)/R)$ yielding the expression for the finesse

$$\mathcal{F} = \frac{\Delta\nu_{\mathrm{FSR}}}{\delta\nu} = \frac{\pi\sqrt{R}}{1-R}. \tag{5.4}$$

Due to a non-perfect reflectivity of the resonator mirrors the laser radiation has a finite lifetime τ which obeys an exponential decay of the form

$$I(t) = I_0\mathrm{e}^{-t/\tau}. \tag{5.5}$$

The finesse of the cavity can be seen as the number of round-trips a single photon undergoes in between of the two mirrors. The finesse and the lifetime are connected as follows

$$\mathcal{F} = \tau \frac{\pi c}{L}. \tag{5.6}$$

Therefore, by measuring the decay of a cavity mode the finesse can be determined. In short, equations (5.3), (5.6) show the connection of the spatial and temporal confinement to the FSR $\Delta\nu_{\mathrm{FSR}}$ and finesse $\mathcal{F}$ of the cavity, respectively.

The transmission and reflection of a cavity can be expressed in terms of the characteristic parameters $\Delta\nu_{\mathrm{FSR}}, \mathcal{F}$. To gain a quantitative understanding consider an incoming monochromatic electric field $E_{\mathrm{in}} = E_0 \exp(\mathrm{i}\omega t)$ with a frequency ω. The reflected electric field from the cavity is $E_{\mathrm{ref}} = E_1 \exp(\mathrm{i}\omega t)$ with the complex amplitude E_0 and E_1. For a symmetric cavity with no losses the reflection coefficient is [114]

$$\mathcal{R}(\omega) = \frac{E_{\mathrm{ref}}}{E_{\mathrm{in}}} = \frac{\sqrt{R}\left(\mathrm{e}^{\mathrm{i}\omega/\Delta\nu_{\mathrm{FSR}}} - 1\right)}{1 - R\mathrm{e}^{\mathrm{i}\omega/\Delta\nu_{\mathrm{FSR}}}}, \tag{5.7}$$

with the free spectral range $\Delta\nu_{\mathrm{FSR}}$ and the reflectivity R of each mirror. The intensity of the reflected beam is

$$\begin{aligned} I_{\mathrm{ref}} &= |\mathcal{R} E_{\mathrm{in}}|^2 \\ &= I_0 \frac{\sin^2\left(\frac{\omega}{2\Delta\nu_{\mathrm{FSR}}}\right)}{(\pi/2\mathcal{F})^2 + \sin^2\left(\frac{\omega}{2\Delta\nu_{\mathrm{FSR}}}\right)} \end{aligned} \tag{5.8}$$

The reflected beam measured on the photodiode consists of the coherent sum of two beams, namely the instantaneously reflected beam at the incoupling mirror and the leakage beam which is transmitted into the cavity. Note that the leakage beam splits inside the cavity into a sum of beams which are reflected different times on the internal side of the cavity mirrors. In the ideal case of a lossless, symmetric cavity both beams have the same intensity and frequency but the phase differs. In the case of perfect cavity coupling, the instantly reflected beam undergoes a phase shift of 180° in reference to the leakage beam due to the reflection at the surface of the incoupling mirror. Therefore, the sum of the beams cancels each other out, illustrated in Fig. 5.2.

The transmitted intensity through the cavity can be obtained equivalently as the reflected intensity yielding the expression

$$I_{\mathrm{trans}} = I_0 \frac{1}{1 + (2\mathcal{F}/\pi)^2 \sin^2\left(\frac{\omega}{2\Delta\nu_{\mathrm{FSR}}}\right)}. \tag{5.9}$$

The sinus term indicates a repeating pattern on the scale of the FSR while the prefactor of the sinus term shows the width of the transmission peaks dependent on the finesse.

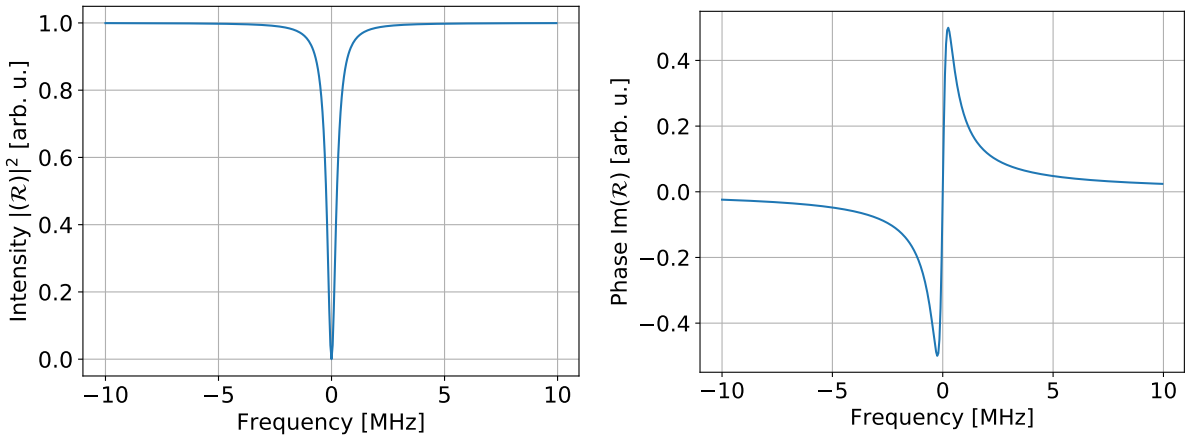

(a) **(b)**

Figure 5.2: Reflection coefficient. **(a)** Intensity $|\mathcal{R}(\omega)|^2$ and **(b)** phase $\mathrm{Im}(\mathcal{R}(\omega))$ of the reflection is shown when the laser frequency is swept over a resonance.

Reflected Signal of the Cavity

The reflected signal shown in Fig. 5.2a is only true for static responses of a cavity. However, the time response of a cavity can be explored when sweeping the laser frequency with a scan rate $\dot{\omega}$ comparable to the lifetime τ of the cavity. Temporal oscillations on the reflection photodiode (and transmission but neglected in the discussion) can be observed. These stem both from interference effects of the cavity field and the directly reflected field and also from modulations of the field inside the cavity [115].

The dynamics of the cavity field for a laser with a sweeping rate $\dot{\omega}$ are described by the differential equation [115]

$$\frac{\mathrm{d}E_{\mathrm{cav}}}{\mathrm{d}t'} = -E_{\mathrm{cav}} + \mathrm{i}\nu_\omega t' E_{\mathrm{cav}} + \mathrm{i}\frac{c\sqrt{T}}{L}\tau E_{\mathrm{in}}, \tag{5.10}$$

with the mirror transmitivity $\sqrt{T}$, $t' = t/(2\tau)$ and the normalized scan frequency

$$\nu_\omega = 4\dot{\omega}\tau^2. \tag{5.11}$$

Here, the laser is on resonance at time $t' = 0$. The derivative of the cavity field depends on the three terms. The first term simply indicates the decay of the resonant cavity mode. The second and third term possess an imaginary pre-factor which indicates an oscillating behavior, i.e. interference effects. However, the oscillating pattern is not only caused from the driving field E_{in} but also from the internal cavity

field E_{cav}. A closed-form solution of the differential equation exists for linear sweeping rates $\dot{\omega}$ which reads [116]

$$|E_{\mathrm{ref}}(t)|^2 = |E_{\mathrm{in}}|^2 \left| 1 - \frac{\beta}{\sqrt{\nu_\omega}} \left[\sqrt{\frac{\pi}{2\mathrm{i}}} \mathrm{e}^{-t' + \mathrm{i}\nu_\omega t'^2 - \mathrm{i}/(2\nu_\omega)} + \sqrt{2\mathrm{i}}\mathcal{D}\left(\frac{\mathrm{i} + \nu_\omega t'}{\sqrt{2\mathrm{i}\nu_\omega}} \right) \right] \right|^2 . \tag{5.12}$$

The cavity contrast parameter $\beta = T/(1-R)$ indicates the loss due to absorption or scattering on the mirrors which is assumed to be 1 due to simplicity. Here, $\mathcal{D}$ is the Dawson integral[7].

Optical Resonators as Spatial Mode Filters

An optical resonator defines not only the frequency distribution but also the spatial distribution of the light. A stable resonator is achieved when the light is confined inside the cavity, i.e. when the light retraces itself after several round-trips. This is the case for instance for plano-concave mirror configuration used in this setup. For optimal cavity coupling mode matching of the incoupling beam and the cavity is required. Consider a Gaussian beam propagating in z-direction at any radial distance r from the symmetry axis of the beam with a polarization in x-direction. The electric field is given by

$$\mathbf{E}(r,z) = E_0 \hat{\mathbf{x}} \frac{w_0}{w(z)} \mathrm{e}^{-\frac{r^2}{w(z)^2}} \mathrm{e}^{-\mathrm{i}\left(kz + \frac{kr^2}{2R(z)} - \zeta(z)\right)}, \tag{5.13}$$

with the beam waist w_0, the radius of the beam $w(z)$, the radius of curvature of the wavefront $R(z)$ and the Gouy phase $\zeta(z)$. The intensity of the Gaussian beam which is proportional to the absolute square of the electric field reads

$$I(r,z) = I_0 \left(\frac{w_0}{w(z)} \right)^2 \mathrm{e}^{-\frac{2r^2}{w(z)^2}}. \tag{5.14}$$

The radius of the beam $w(z)$ is related to the beam waist as

$$w(z) = w_0 \sqrt{1 + (z/z_R)^2}, \tag{5.15}$$

while $z_R = \pi w_0^2/\lambda$ is defined as the Rayleigh length at which the radius of the beam becomes $\sqrt{2}w_0$. Optimal coupling into the cavity is achieved when the curvature

$$R(z) = z \left[1 + \left(\frac{z_R}{z} \right)^2 \right] \tag{5.16}$$

of the beam is equal to the curvature of the second cavity mirror R_2 at the position of the mirror. The same mode matching argument holds for the planar mirror which requires the waist of the Gaussian beam at the position of the first cavity mirror R_1.

7 The Dawson integral $\mathcal{D}$ is defined as $\mathcal{D}(x) = \exp(-x^2) \int_0^x \exp(z^2) dz$

Degeneracy of the Cavity Modes

The fundamental Gaussian mode is not the only solution to the Helmholtz equation (5.2) but the whole family of Laguerre-Gaussian beams represent modes of spherical-mirror resonators [113]. The curvature of each wavefront of the Laguerre-Gaussian modes is the same but the electric field distribution differs. This dependency is imprinted on the Gouy phase $\zeta(z) = \arctan(z/z_R)$. It takes into account that the light is not a planar wave but a Gaussian beam which acquires a different phase shift. This leads to an increased distance of the wavefronts of a Gaussian beam compared to a planar wave with the same frequency. However, Gaussian modes of different order (l, m) acquire a phase shift with respect to each other as well. This results in a frequency spacing of the longitudinal q and transverse modes (l, m) and is given by [113]

$$\nu_{\mathrm{q,l,m}} = q\Delta\nu_{\mathrm{FSR}} + (l + m + 1)\frac{\Delta\zeta}{\pi}\Delta\nu_{\mathrm{FSR}}, \tag{5.17}$$

with the difference of the acquired Gouy phase $\Delta\zeta = \zeta(z_1) - \zeta(z_2)$ at the position $z_{1,2}$ of each mirror. This equation is consistent with the above obtained longitudinal frequency distance to a given transverse mode which is the FSR $\nu_{(\mathrm{q,q+1}),\mathrm{l,m}} = \Delta\nu_{\mathrm{FSR}}$. The transverse modes $(l, m), (l', m')$ with the same longitudinal mode are spaced in frequency:

$$\nu_{\mathrm{q,l,m}} - \nu_{\mathrm{q,l',m'}} = [(l - l') + (m - m')]\frac{\Delta\zeta}{\pi}\Delta\nu_{\mathrm{FSR}}. \tag{5.18}$$

For $\Delta\zeta = \pi/2$ the longitudinal modes associated with different transverse modes become either degenerate or displaced by $\Delta\nu_{\mathrm{FSR}}/2$ depending on the higher mode (l, m). Since the cavity is used a reference frequency for laser locking degeneracy of the modes is undesired.

The difference of the Gouy phase $\Delta\zeta$ can be determined by means of the boundary conditions. This is done in reference [113] for arbitrary mirror curvatures R_1, R_2. By assuming that $|R_1| \gg |R_2|$ the expression for $\Delta\zeta$ can be simplified to

$$\Delta\zeta = \arctan\sqrt{\left|\frac{L}{R_2 - L}\right|} - \arctan\sqrt{\left|\frac{L}{R_1}\frac{R_2 - L}{R_1 + L}\right|}. \tag{5.19}$$

In Fig. 5.3 the Gouy phase shift $\Delta\zeta$ is shown in dependence of the mirror curvature R_2 for a cavity of the length $L = 100.1\,\mathrm{mm}$ and $R_1 \to \infty$ which is close to the parameters of the experiment setup. This illustrates that for equal cavity length and mirror curvature $L = R_2$ the longitudinal modes exhibit degeneracy. In order to avoid this effect the curvature of the mirror is chosen different from the cavity length. In particular, the frequency difference of our cavity with $R_2 = 500\,\mathrm{mm}$ (red cross) leads to a frequency spacing of higher transverse modes 221 MHz. Therefore, the single fundamental Gaussian mode can serve as a reference frequency for laser locking, explained in the next section.

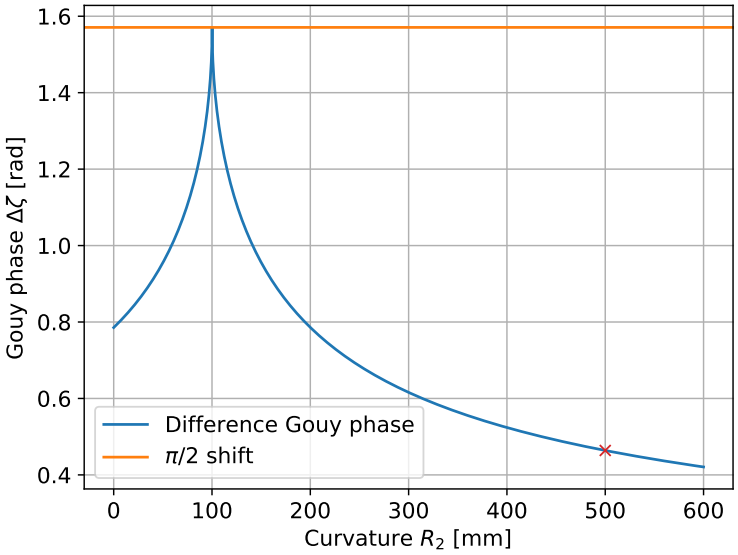

Figure 5.3: Difference of the Gouy phase $\Delta\zeta$ acquired by a Gaussian beam. The dependency of the Gouy phase on the curvature of the concave mirror R_2 is shown for a fixed length $L = 100.1\,\text{mm}$ of the cavity. The constant (orange) line indicates a phase shift of $\pi/2$ and thus degeneracy of the longitudinal modes associated with different transverse modes. Degeneracy takes place at $R_2 = L$. The red cross indicates the curvature of the mirror used in our setup. The length L resembles the cavity length used in the experiment.

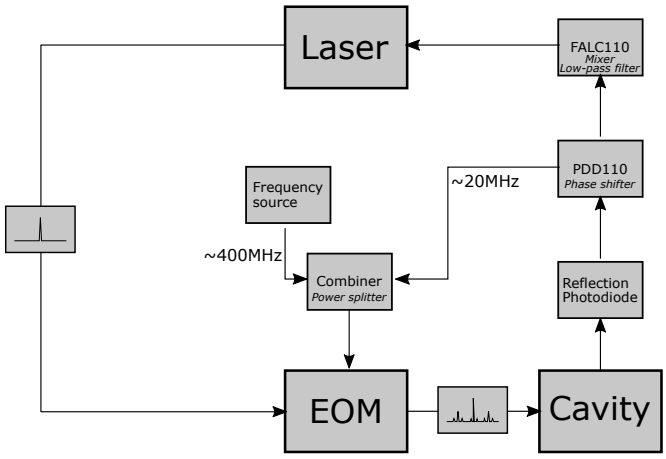

Figure 5.4: Basic layout of the electronic cavity setup. The carrier frequency is modulated with sidebands, subsequently the reflected signal of the cavity mirrors is processed on a photodiode and further modified with a phase-shifter, mixer and low-pass filter. The error signal is fed back to the laser.

PDH Error Signal

In order to stabilize the laser frequency to the cavity one can either use the transmitted or the reflected signal. However, the transmitted signal has some disadvantages compared to the reflected signal. Suppose that the laser light is operated near resonance of the cavity, i.e. a small amount of light is transmitted through the cavity. A change in the laser frequency generates a proportional error signal. Thus, with this method it is not possible to distinguish between intensity and frequency fluctuations.

In case of the reflected signal it is possible to distinguish between intensity and frequency deviations but due to the symmetry not in which direction the frequency drifts.

To get access to the derivative of the reflected signal the laser beam is phase modulated generating sidebands with a definite phase relation to the carrier frequency. The basic layout is sketched in Fig. 5.4. Given the phase standard by the sidebands it is possible to measure the phase of the reflected beam. In the following the error signal is derived mathematically.

Modulating a phase with an amplitude β and a modulation frequency Ω onto the incoming electric field yields the expression

$$\begin{aligned} E_{\text{in}} &= E_0 \mathrm{e}^{\mathrm{i}(\omega t + \beta \sin \Omega t)} \\ &= E_0 \mathrm{e}^{\mathrm{i}\omega t} \sum_{-\infty}^{\infty} J_n(\beta) \mathrm{e}^{\mathrm{i}n\Omega t} \\ &\approx E_0 \left[J_0(\beta) \mathrm{e}^{\mathrm{i}\omega t} + J_1(\beta) \mathrm{e}^{\mathrm{i}(\omega+\Omega)t} - J_1(\beta) \mathrm{e}^{\mathrm{i}(\omega-\Omega)t} \right]. \end{aligned} \tag{5.20}$$

Here, the Bessel functions J_i, $i \in \{0, 1\}$ are used and $\beta \ll 1$ is assumed. Hence, the incoming beam consists of a carrier with frequency ω and two sidebands with

frequencies $\omega \pm \Omega$. The reflected beam can be calculated by treating each term in Eq. (5.20) independently resulting in

$$\begin{aligned} E_{\text{ref}} = E_0[&\mathcal{R}(\omega)J_0(\beta)e^{i\omega t} \\ &+ \mathcal{R}(\omega+\Omega)J_1(\beta)e^{i(\omega+\Omega)t} - \mathcal{R}(\omega-\Omega)J_1(\beta)e^{i(\omega-\Omega)t}]. \end{aligned} \tag{5.21}$$

On the photodiode the absolute sqaure value of the reflected electric field E_{ref} is measured. Assuming an incident power of $P_0 = |E_0|^2$ yields a power of the reflected beam of

$$\begin{aligned} P_{\text{ref}} &= |E_{\text{ref}}|^2 \\ &= J_0^2(\beta)P_0|\mathcal{R}(\omega)|^2 + J_1^2(\beta)P_0\left(|\mathcal{R}(\omega+\Omega)|^2 + |\mathcal{R}(\omega-\Omega)|^2\right) \\ &+ 2J_0(\beta)J_1(\beta)P_0\text{Re}\left(\mathcal{R}(\omega)\mathcal{R}^*(\omega+\Omega) - \mathcal{R}^*(\omega)\mathcal{R}(\omega-\Omega)\right)\cos\Omega t \\ &+ 2J_0(\beta)J_1(\beta)P_0\text{Im}\left(\mathcal{R}(\omega)\mathcal{R}^*(\omega+\Omega) - \mathcal{R}^*(\omega)\mathcal{R}(\omega-\Omega)\right)\sin\Omega t \\ &+ (2\Omega \text{ terms}). \end{aligned} \tag{5.22}$$

Due to the phase modulation, in addition to the carrier beam at a frequency ω the two sidebands at frequencies $\omega \pm \Omega$ occur. Furthermore, the Ω terms arise due to interference of the carrier frequency with the sidebands. The 2Ω terms result from the interference of the sidebands with each other.

Furthermore, the signal is processed in a mixer and low-pass filter. Mathematically, a mixer forms the product of its input, whereas the low-pass filter isolates the low-frequency components. The phase shifter is needed to compensate delays in the two signal paths. In the case of fast phase modulations $\Omega \gg \Delta\nu_{\text{FSR}}/\mathcal{F}$, which is fulfilled in the experiment since $\Omega \approx 20\,\text{MHz}$ and $\Delta\nu_{\text{FSR}}/\mathcal{F} \approx 1.5\,\text{GHz}/40\,000 = 37.5\,\text{kHz}$, the Pound-Drever-Hall signal yields [114]

$$P_{\text{ref}} = -2J_0(\beta)J_1(\beta)P_0\text{Im}\left(\mathcal{R}(\omega)\mathcal{R}^*(\omega+\Omega) - \mathcal{R}^*(\omega)\mathcal{R}(\omega-\Omega)\right), \tag{5.23}$$

shown in Fig. 5.5. The Pound-Drever-Hall signal consists of a steep slope around zero perfectly suited for locking the laser.

Note that the PDH frequency is much smaller than the frequency spacing of higher transverse modes. Hence, cross-talk of the locking electronics to the higher modes is inhibited.

5.2.2 *Setup of the Cavity System*

In this experiment a plano-concave cavity[8] with a plane $R_1 = \infty$ and a concave mirror $R_2 = 500\,\text{mm}$ is used for frequency stabilization of the master, Rydberg and 3D MOT laser. The optical setup is shown in Fig. 5.6. The mirrors are placed 100 mm

8 Stable Laser Systems ATF 6010-4 cylindrical cavity

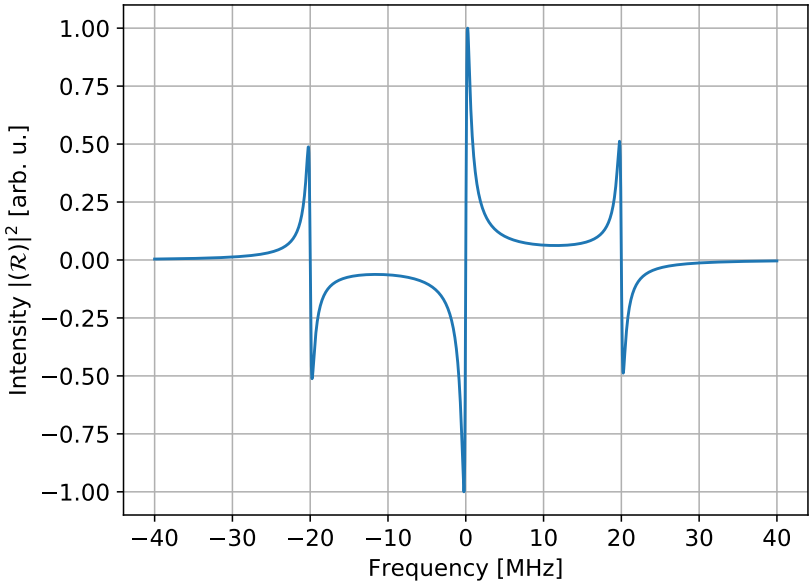

Figure 5.5: Pound-Drever-Hall signal for a cavity with finesse $\mathcal{F} = 39\,268$, a free spectral range $\Delta\nu_{\mathrm{FSR}} = 1.5\,\mathrm{GHz}$ and sidebands at $\pm 20\,\mathrm{MHz}$. These values agree approximately with the cavity specifications.

apart with a spacer out of ultra-low-expansion (ULE) glass. The thermal expansion coefficient of ULE glass has a zero crossing temperature at $T_{\mathrm{C}} = 30.7\,^{\circ}\mathrm{C}$, therefore the cavity is heated with Peltier elements constantly to that temperature for minimal distance deviations of the mirrors. The mirrors are anti-reflection coated[9] for all three wavelengths 798 nm, 790 nm and 1112 nm. The optical resonator is placed on a block of Zerodur for temperature and vibration isolation. This assembly is placed in an aluminium housing and pumped down to $10^{-8}\,\mathrm{mbar}$. To reduce thermal expansion due to heating by the incoupled light the power of each laser beam is $P_{\mathrm{master}} = 40\,\mu\mathrm{W}$, $P_{\mathrm{Rydberg}} = 43\,\mu\mathrm{W}$ and $P_{\mathrm{3DMOT}} = 100\,\mu\mathrm{W}$. Reducing the power even further leads to poor lock performance since the error signal is generated from the reflected signal of the cavity [117].

To couple all three lasers into the cavity the laser beams are overlapped. A PBS cube[10] is used to overlap the master laser, 798 nm, and the Rydberg laser, 790 nm, due to their similar wavelength. In order to avoid crosstalk between the reflected beam of the master and the Rydberg laser due to the low extinction ratio of PBS cube on the reflected beam an additional PBS cube is mounted perpendicular. Therefore, this cube acts as a filter for the horizontally polarized components of both beams. The 3D MOT laser, 1112 nm, is overlapped with the other two beams with a dichroic mirror[11].

9 Five Nine Optics
10 Thorlabs B-coated PBS cube. The extinction ratio of the reflected beam is 20:1 to 100:1 depending on the individual cube
11 Thorlabs DMLP900

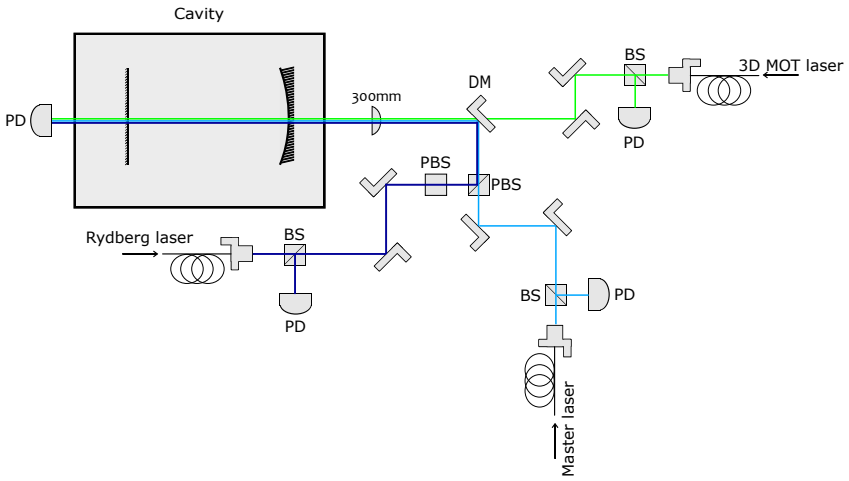

Figure 5.6: Schematics of the optical setup of the cavity system. All three laser beams are overlapped with a polarizing beam splitter (PBS) and a dichroic mirror (DM). The transmission signal is detected on a photoiode (PD). The beam splitter (BS) in front of the fiber output is rotated such that the reflected beam hits the photodiode (PD).

A lens with a focal length of $f = 300\,\mathrm{mm}$ is placed in front of the cavity such that the curvature of the laser beams matches with the curvature of the plano-convex mirror and the waist with the planar mirror, see section 5.2.1. The photodiode behind the cavity detects the transmitted signal through the cavity used for optimization of the cavity coupling and for monitoring the laser locks. The reflected signal is detected on a photodiode and further processed for generating the PDH error signal.

A fiber-coupled EOM is used to modulate the PDH sidebands on the carrier frequency of the lasers locked to the cavity. The key component of the EOM is a lithium niobate crystal. The refractive index of the crystal is dependent on the local electric field exposed to the EOM. Hence, the phase of the outcoupled light is changed based on the time it travels trough the crystal. By modulating a sinusoidal varying electric field on the EOM the frequency of the laser light is modulated, see section 5.2.1. In particular, while the laser is coupled to the crystal the PDH frequency is mixed on the EOM. Hence, the outcoupled laser contains symmetric sidebands at the applied PDH frequency. These are 15 MHz, 20 MHz and 25 MHz in the case of the Rydberg, 3D MOT and master laser, respectively. However, this allows only the stabilization of the laser to the eigenmodes of the cavity which are equally spaced at $\sim 1.5\,\mathrm{GHz}$. Typically, in Rydberg experiments it is required to control the laser frequency down to kHz to address the proper Rydberg state. Moreover, during one experiment it is required to scan the frequency of the probe laser step by step. Here, a typical range is 100 MHz [118]. For Yb, the range is expected to be higher since the linewidth of the probe transition is larger compared to Rb. Hence, locking the lasers directly to the resonances of the optical resonator is not suited.

A common approach to frequency shift the laser is the usage of an AOM. However, an AOM can only operate in a small frequency range. To overcome this limitation, the range can be enlarged by using the AOM in a configuration in which the light passes several times but this technique reduces the final output power to the experiment significantly.

In the experiment a different approach is taken. An additional sideband produced by a rf-source[12] is modulated on the laser frequency. The frequency distance of the rf-sideband can be chosen in between 50 MHz and 750 MHz. The PDH-frequency and the rf-frequency are mixed on the EOM and thus onto the carrier frequency. This leads to three error signals, the carrier frequency plus two rf-sidebands symmetrically displaced at the applied frequency. The laser is locked to one of the rf-sidebands which has a determined frequency distance to the carrier set by the rf-source. As a consequence, when scanning the rf-source frequency the laser frequency follows since the feedback of the lock keeps the laser in resonance with the cavity. This technique has the advantage over the AOM that the outcoming power is not affected by an additional optical element. Furthermore, it allows the scan of the laser frequency over almost half of a free spectral range, i.e. 750 MHz, in practice slightly smaller. Though it should be noted that the amplitude of the rf-sidebands has to be chosen such that the longterm stability of the lock does not suffer.

5.2.3 *Characterization of the Cavity*

In order to characterize the cavity the two key parameters, the free spectral range $\Delta\nu_{\mathrm{FSR}}$ and the finesse $\mathcal{F}$, are determined. The free spectral range can be measured by applying sidebands at a known frequency to the laser. The laser is scanned over a frequency range larger than the FSR. Such a signal is shown in Fig. 5.7. The carrier frequencies are marked with oranges crosses while the green crosses corresponds to the rf-sidebands. No PDH-frequency is applied. The excitation of higher transverse modes in the vicinity of the TEM_{00} is in all three cases below the one per cent level. The small peaks are caused by higher order frequencies of the rf-source. Since the frequency difference of the carrier frequency and the sideband is known this can be used as a ruler to determine the frequency difference between the two eigenmodes of the cavity.

The time difference of the rf-sideband and the carrier frequency on the photodiode corresponds to a frequency of 400 MHz. The frequency difference of the carrier bands, i.e. the FSR, can be calculated by

$$\Delta\nu_{\mathrm{FSR}} = \Delta f_{\mathrm{sideband}} \frac{\Delta t_{\mathrm{carrier}}}{\Delta t_{\mathrm{sideband}}}, \tag{5.24}$$

12 Windfreak Technologies - SynthUSBII

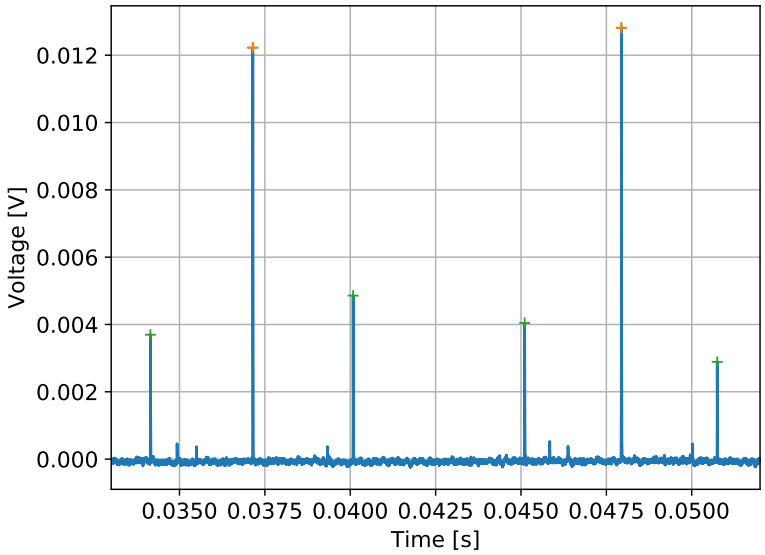

Figure 5.7: Signal on the transmission photodiode of the master laser while scanning the piezo over a cavity mode. The carrier frequencies are marked with orange crosses while the rf-source sidebands at ±400 MHz are marked with green crosses. The small peaks are higher order frequencies of the rf-source.

with the time difference of the carrier bands $\Delta t_{\text{carrier}}$ and the difference of the sideband and the carrier $\Delta t_{\text{sideband}}$ on the photodiode. The obtained free spectral range is

$$\Delta\nu_{FSR} = 1.469\,\text{GHz} \pm 0.035\,\text{GHz}. \tag{5.25}$$

The error is obtained from the peak detection method. Even though the experimentally obtained value and the theoretical value agree within the estimated error, a systematic error underlies this method. Here, it is assumed that the frequency change of the laser is proportional to the time on the photodiode. However, this is not the case since the piezo does not scan the laser frequency linearly. In contrast, the piezo undergoes a hysteresis-like scanning behavior. This is verified by scanning the laser over a multiple of free spectral ranges. The free spectral range is measured for each pair of cavity modes and plotted over the number of modes, shown in Fig. 5.8. Clearly, it can be seen that $\Delta\nu_{FSR}$ increases and decreases again with a maximum in the center indicating that the scan is at the inflection point, which is typical for hysteresis. In section 5.3 a more sophisticated method to obtain the free spectral range is presented.

The finesse of the cavity can be measured in two different ways by means of the cavity ring-down time. The basic principle of the first method is to lock the laser to the cavity and subsequently kicking it out of lock such that the PID controller is not able to follow. In particular, this is examined by applying a short square pulse with a voltage $U = 100\,\text{mV}$ and a width $t_w = 20\,\mu\text{s}$ to the second input of the

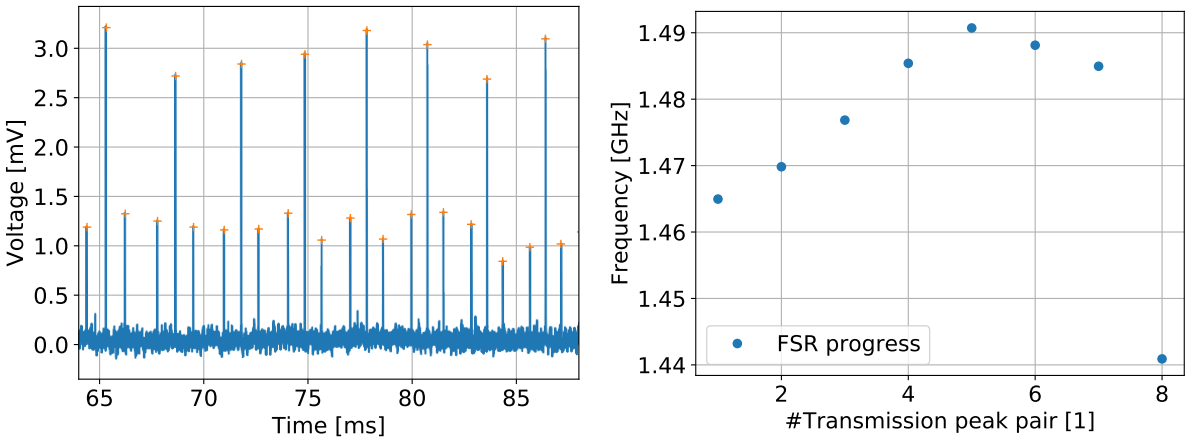

(a) **(b)**

Figure 5.8: Verification of the Hysteresis-like behaviour of the piezo. **(a)** The scan voltage of the piezo was chosen such that the diode laser scans over several, more specific eight, cavity modes. The orange crosses mark the values used for calculating the FSR. **(b)** Calculated FSR of each transmission peak pair.

commercial PID controller[13]. The oscilloscope is triggered on the pulse. Hence, the coupling into the cavity is destroyed and the laser light is completely reflected. As described in section 5.2.1, the resonant mode has a finite lifetime inside the cavity due to non-perfect reflectivity of the mirrors. As a consequence, the resonant mode decays out of the cavity and is detected on the transmission photodiode, shown in the left column in Fig. 5.9.

The decay of the resonant mode, equation (5.5), is fitted to the data displayed in orange. Small times, i.e. $0\,\mu s \leq t \lessapprox 5\,\mu s$, are not taken into account for the determination of the lifetime for the following reason. By applying the short square pulse to the PID controller a sudden change in the laser frequency takes place. The linewidth of the laser is not compressed by the lock anymore and therefore broadens. However, the change in frequency is not large enough to avoid overlap of the broadened laser frequency and the resonant mode of the cavity. Hence, a small fraction of the light is still in resonance and thus leaks into the cavity and the signal on the transmission photodiode deviates from an exponential decay for small times.

The obtained lifetime of the master, Rydberg and 3D MOT laser via the first method reads $\tau_{m,1} = 4.3\,\mu s \pm 0.3\,\mu s$, $\tau_{R,1} = 4.2\,\mu s \pm 0.3\,\mu s$ and $\tau_{3D,1} = 4.5\,\mu s \pm 0.4\,\mu s$, respectively, with the error obtained from the fit parameter and the additional degree of freedom in the choice of the data used for the fit function. The error of the 3D MOT laser is assumed to be slightly larger due to the higher noise level. This is caused by the photodiode which has a significant drop of sensitivity above wavelengths of roughly 1000 nm.

13 Toptica FALC 110

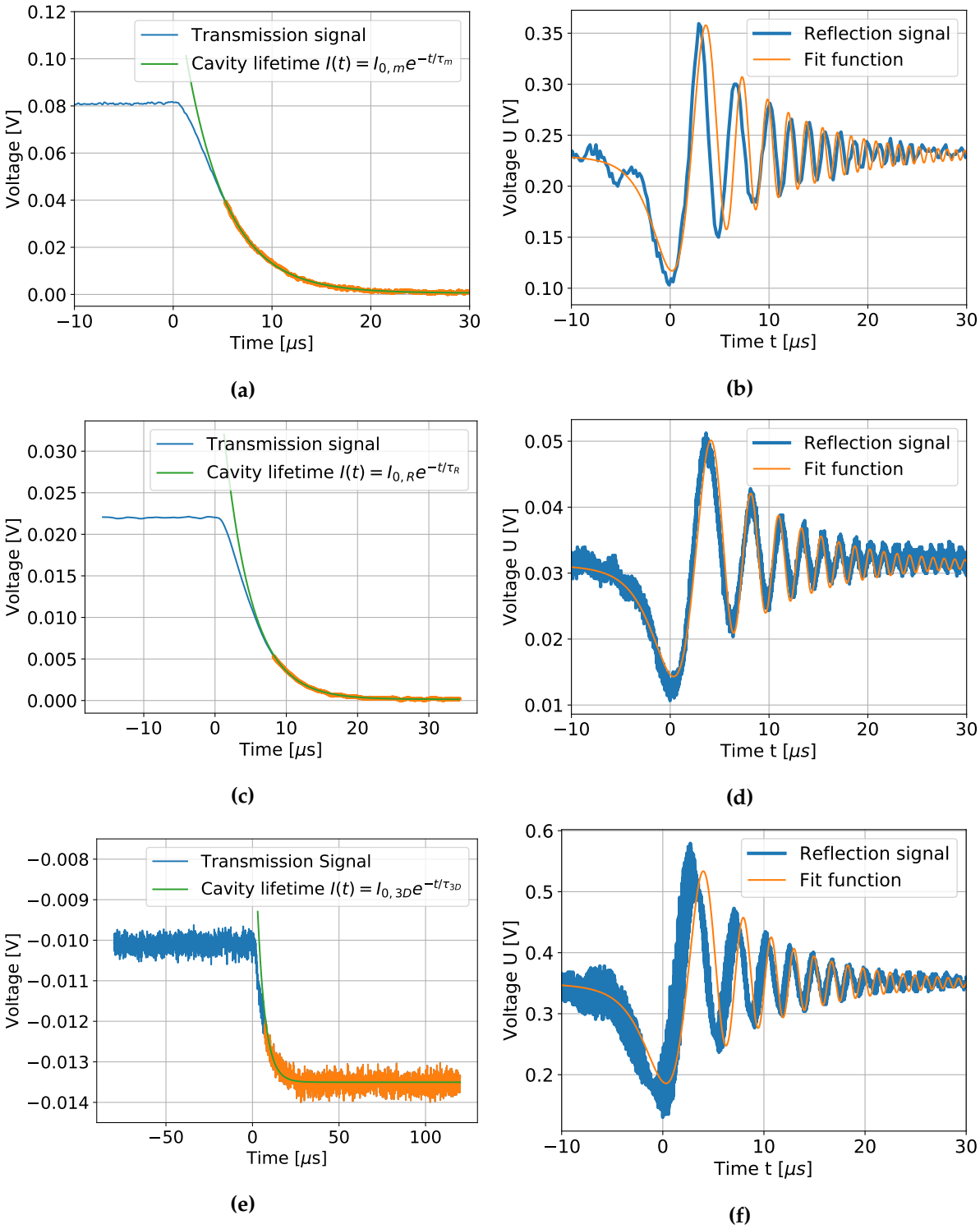

Figure 5.9: Finesse measurement of the **(a,b)** master, **(c,d)** Rydberg and **(e,f)** 3D MOT laser locked to the cavity. In the left column, the finesse is measured vie the decay of the resonant cavity mode on the transmission photodiode by kicking the laser out of lock. The data used for the fit function is displayed in orange. In the right column, the signal on the reflected photodiode is used to determine the finesse by sweeping the incident laser frequency with a rate comparable to the cavity lifetime.

Table 5.2: Experimentally obtained finesse compared to the specification of the supplier. The finesse is measured in two different ways. First, by locking the laser to the cavity and subsequently kicking it out of lock. The decay of resonant cavity mode is measured on photodiode. Second, the reflected signal is observed on a photodiode while sweeping the laser frequency at a rate comparable to the cavity-ring-down time which renders interference effects visible allowing to determine the lifetime of the cavity mode.

LASER	LOCKING METHOD (1)	REFLECTION METHOD (2)	THEORY
Master $\mathcal{F}_{\mathrm{m}}$	$40\,420 \pm 2820$	$38\,540 \pm 4230$	$42\,230$
Rydberg $\mathcal{F}_{\mathrm{R}}$	$39\,480 \pm 2820$	$38\,540 \pm 3290$	$37\,600$
3D MOT $\mathcal{F}_{3\mathrm{D}}$	$42\,300 \pm 3760$	$39\,480 \pm 4230$	$39\,300$

The basic principle of the second method does not require the laser to be locked to the cavity but the laser is swept over a cavity resonance. For comparable sweeping scan rates and cavity-ring-down times interference effects of the incoming and cavity light become visible, see section 5.2.1. In particular, the scan frequency of each laser is set to 10 Hz. The scan frequency rate is sufficiently fast to observe the interference pattern, shown in the right column of Fig. 5.9.

The ring-down time is extracted by fitting equation (5.12) to the data. The theoretical function and the decay of the signal are in good agreement although they differ for small times. This is caused by the nonlinear frequency sweep of the piezo, as explained previously in this section. However, the theoretical fit function resembles the decay of the signal yielding lifetimes for the master, Rydberg and 3D MOT laser via the second method $\tau_{\mathrm{m},2} = 4.1\,\mu\mathrm{s} \pm 0.45\,\mu\mathrm{s}$, $\tau_{\mathrm{R},2} = 4.1\,\mu\mathrm{s} \pm 0.35\,\mu\mathrm{s}$ and $\tau_{3\mathrm{D},2} = 4.2\,\mu\mathrm{s} \pm 0.45\,\mu\mathrm{s}$, respectively. The large errors stem from the nonlinear sweeping rate.

The experimentally obtained lifetimes τ of both methods and the theoretical length $L = 100.1\,\mathrm{mm}$ found in the specification sheets are used to determine the finesse of each laser, shown in table 5.2. In principle, the length can be determined from the measured FSR, equation (5.25), with the relation from equation (5.3). However, the theoretical length from the specifications is used due to the high uncertainty of the experimentally extracted FSR. Comparing the obtained values with the theoretical values calculated from the reflectivity of the mirrors a good agreement between the two experimental methods and the theory is found.

Degeneracy of longitudinal cavity modes associated with different transverse modes breaks the unambiguousness of the Gaussian mode as the reference frequency and hence, distorts the locking performance. The spacing of higher transverse modes is determined by scanning the laser across the FSR and misaligning the coupling into the cavity slightly such that the first transverse mode is excited. This is shown in

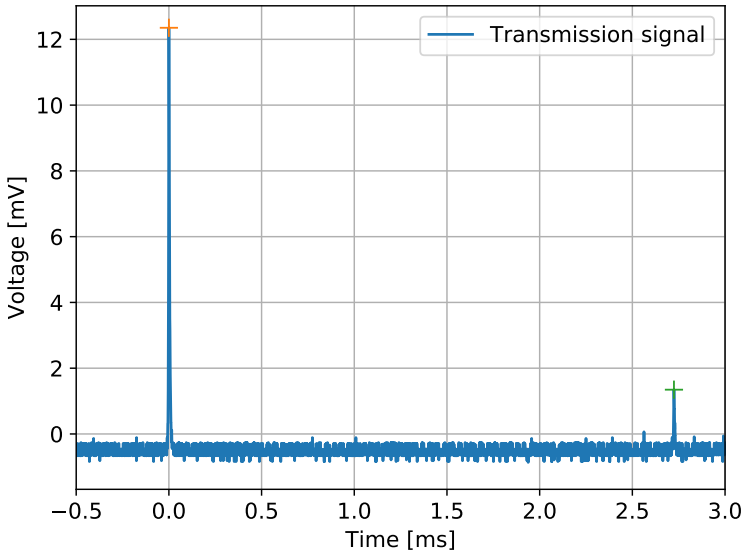

Figure 5.10: Photodiode transmission signal of the cavity. The coupling into the cavity is delibaretly misaligned such that a higher transverse mode (green cross) is excited. The carrier frequency is marked with an orange cross.

Fig. 5.10. The frequency distance is extracted in the same manner as the FSR from equation (5.25) and reads

$$\Delta\nu_{\text{Higher mode}} = 228\,\text{MHz} \pm 35\,\text{MHz}. \tag{5.26}$$

The same error as for the FSR measurement is assumed since the same systematic deviation applies. The obtained spacing of the higher mode is in good agreement with the theoretical value from equation (5.19) $\Delta\nu_{\text{Higher mode, theo}} = 221\,\text{MHz}$. Despite the high uncertainty, the measurement shows that the frequency distance of higher transverse modes is much larger than typical PDH frequencies. Hence, the lock performance is not reduced by the different eigenmodes of the cavity.

5.2.4 *Characterization of the PDH Error Signal*

The lock performance of a laser highly depends on the error signal. In particular, the lock range can be determined from the slope of the PDH signal at the reference frequency. Here, the theoretical PDH signal introduced in section 5.2.1 and the experimentally acquired signal are compared and the lock range of the Rydberg laser is determined.

To obtain the PDH error signal, the PDH sidebands are applied to the laser while it is scanned slowly with a scan frequency 0.1 Hz over a free spectral range. The commercial PID controller provides a monitor output after the reflection signal is

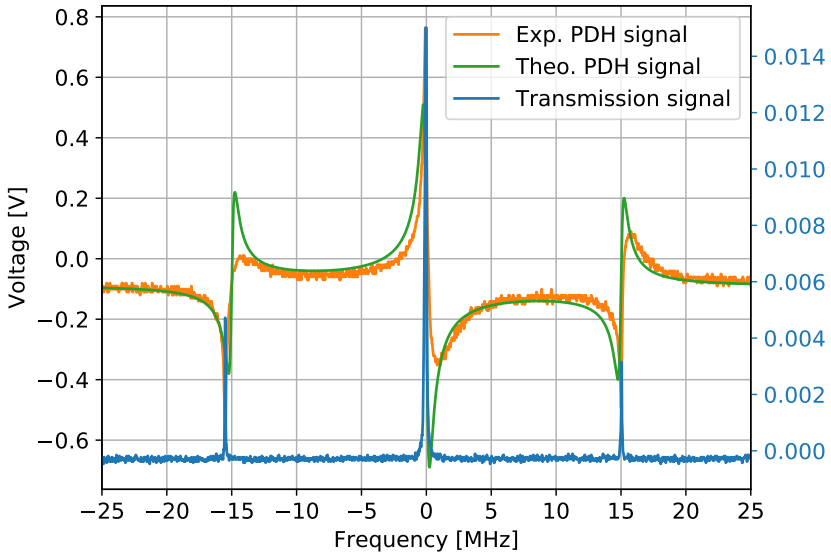

Figure 5.11: Comparison of the experimental and theoretical PDH error signal. The transmission signal (right y-axis) is shown with the experimentally and theoretically obtained PDH error signal (left y-axis). The PDH sidebands are modulated at ±15 MHz. Due to known frequency distance of the sidebands the x-axis is scaled in frequency space. However, this is solely an approximation since the evaluation from Fig. 5.8 has shown that the frequency is not exactly proportional to the time on the oscilloscope.

modulated with the phase shifter, the mixer and the low-pass filter. In Fig. 5.11 the PDH error signal of the Rydberg laser is shown, in comparison with the theoretical error signal from equation (5.23). For optimal lock performance the zero-crossing of the PDH error signal overlaps exactly with the transmission peak of the carrier frequency. Since the adjustment of the offset is highly sensitive the PDH signal does not converge to 0 V. However, after shifting the theoretical PDH offset to −0.9 mV the experimental and theoretical curves agree quite well even though the experimental PDH signal is not perfectly symmetric. Further, the PDH signal observed on the oscilloscope is not quite constant but changes the symmetry and especially the peak height at each trigger.

The slope of the PDH signal specifies the capture range of the lock. This is obtained by reading out the slope of the central part of the PDH signal. Further, the ratio of the peak-to-peak amplitude $\Delta U = 0.663\,\mathrm{V} \pm 0.01\,\mathrm{V}$ of the central part and the absolute value of the slope $a = -1.923\,\mathrm{V/MHz} \pm 0.116\,\mathrm{V/MHz}$ yield the capture range

$$f_{\mathrm{range}} = 345\,\mathrm{kHz} \pm 26\,\mathrm{kHz}, \tag{5.27}$$

with the error obtained by error propagation from the fit parameters. Note that the sign of the slope of the PDH signal can be changed by shifting the phase of the phase mixer (Fig. 5.4) by 180°.

5.3 MEASUREMENT OF THE LASER LINEWIDTH

In the previous section 5.2.4 the sideband method for measuring the FSR was presented. However, it turned out that this is imprecise due to a systematic error in the measurement technique. Here, the FSR is measured by means of optical heterodyne detection. It is based on mixing two lasers with similar wavelength resulting in a signal observable with a spectrum analyzer[14] or a fast-Fourier-transform oscilloscope[15]. A short introduction to the limitations of the resolution with either device is given. It transpires that the resolution of the spectrum analyzer is not high enough for proper characterization of the beat note signal. Thus, this is done by switching to the FFT oscilloscope which gives access to higher resolution. Furthermore, the beat note signal is exploited to analyze the lock performance and to obtain an upper boundary for the linewidth of the laser frequency.

5.3.1 *Theoretical Background of Laser Linewidth Measurement*

Optical Heterodyne Detection

Optical heterodyne detection is a measurement technique for determination of the linewidth of a laser. Two lasers with nearly similar frequencies are superimposed. This leads to an oscillation at the difference and the sum of the two frequencies under the condition that the spatial distribution overlaps and that the polarization is non-orthogonal. The sum of the lasers is in the optical range and therefore not accessible with electronics. However, the beat frequency, i.e. the difference of the frequencies, can be in the MHz-GHz range and is therefore resolvable with standard spectrum analyzers or FFT oscilloscopes. In the following, a short theoretical description is given by means of the signal detection of a beat note signal with a photodiode and the subsequent visualization with a spectrum analyzer.

The intensity of two superimposed lasers with an electric field

$$E_{1/2} = \mathrm{Re}\left[E_{0,1/2} e^{\mathrm{i}(\omega_{1/2} t + \varphi_{1/2})}\right] \tag{5.28}$$

for laser 1 and 2 detected with an AC photodiode reads

$$I(t) = (E_1(t) + E_2(t))^2 = E_1^2(t) + E_2^2(t) + 2E_1(t)E_2(t). \tag{5.29}$$

14 Agilent Spectrum Analyzer N9322C, 9 kHz-7.0 GHz

15 Teledyne Wavepro 735Zi, 3.5GHz Oscilloscope, 40 GSs^{-1}

The first two terms correspond to the constant intensity while the last term is a result of interference of the electric field of laser 1 with laser 2. The constant terms are filtered out while the oscillating terms are measured by the AC photodiode. In order to detect the oscillating signal a spectrum analyzer which measures the power spectral density can be used. The Wiener-Khinchin theorem states that the power spectral density S of a stationary stochastic process is equal to the Fourier transformation $\mathfrak{F}$ of the corresponding auto correlation function [119]. Here, the autocorrelation function is the correlation $\langle\cdot\rangle$ of a signal $I(t)$ with its own signal $I(t+\tau)$ but delayed by a time τ [120]. Putting the Wiener-Khinchin-theorem and the autocorrelation function together yields the expression

$$S(\omega) = \mathfrak{F}\left[\langle I(t)I(t+\tau)\rangle\right]. \tag{5.30}$$

This equation can be written in a form such that the power spectral density S of the beat note is expressed in terms of the power spectral density of the two lasers [121]

$$S(\omega) = \left(S_{E_1} \otimes S_{E_2}\right)(\omega). \tag{5.31}$$

In short, the power spectral density of the heterodyne detection, i.e. the beat note signal, is a convolution of the power spectral density of both lasers. A detailed calculation can be found in [122].

The beat note signal gives direct access to the determination of the laser linewidth. The finite linewidth stems from white noise due to quantum fluctuations and $1/f$-noise due to technical noise. It can be shown that white noise leads to a Lorentz laser spectrum while $1/f$-noise causes a gaussian broadening. In general, both noise types contribute to the finite laser linewidth leading to a Voigt profile. This is a convolution of a Gaussian

$$S_{\mathrm{G}} = \frac{1}{\sigma\sqrt{2\pi}} \mathrm{e}^{-(\omega-\mu_{\mathrm{G}})/2\sigma^2} \tag{5.32}$$

and Lorentzian curve

$$S_{\mathrm{L}} = \frac{1}{\pi}\left(\frac{\Gamma}{(\omega-\mu_{\mathrm{L}})^2+\Gamma^2}\right), \tag{5.33}$$

with the center $\mu_{\mathrm{G,L}}$. From these definitions it follows that the FWHM of the Gaussian function is

$$\Delta\omega_{\mathrm{G}} = 2\sigma\sqrt{2\ln 2} \tag{5.34}$$

and of the Lorentzian function

$$\Delta\omega_{\mathrm{L}} = 2\Gamma. \tag{5.35}$$

Note that both distributions are normalized. The normalized Voigt function has the form

$$\begin{aligned} S_{\mathrm{V}} &= (S_{\mathrm{G}} \otimes S_{\mathrm{L}})(\omega) \\ &= \int_{\infty}^{\infty} S_{\mathrm{G}}(\omega') S_{\mathrm{L}}(\omega - \omega') \mathrm{d}\omega' \\ &= \frac{1}{\sigma\sqrt{2\pi}} \mathrm{Re}\left[\mathrm{erfc}\left(\frac{\omega - \omega_0 + \mathrm{i}\gamma}{\sigma\sqrt{2}}\right)\right], \end{aligned} \tag{5.36}$$

with the complementary error function erfc[16]. The linewidth of the of the Voigt profile cannot be acquired analytically, but an approximation with an accuracy of 0.02 % the Voigt linewidth $\Delta\omega_{\mathrm{V}}$ reads [123]

$$\Delta\omega_{\mathrm{V}} = 0.5346\Delta\omega_L + \sqrt{0.2165975\Delta\omega_L^2 + \Delta\omega_{\mathrm{G}}^2}, \tag{5.37}$$

where $\Delta\omega_{\mathrm{G}}$ is the Gauss linewidth and $\Delta\omega_{\mathrm{L}}$ the Lorentz linewidth.

Resolution Bandwidth

In our laboratory two devices are available to display frequency signals in the range kHz − GHz, i.e. a spectrum analyzer and a FFT oscilloscope. Here, a short introduction to the limitation by means of the resolution of either device is given.

The spectrum analyzer has resolution bandwidth (RBW) of 10 Hz and a video bandwidth (VBW) of 1 Hz. The RBW is the bandwidth over which two signals are distinguishable. The VBW filters noise which acts as a low-pass filter but increases the sweep time [124].

The FFT oscilloscope can be used to convert the time domain into frequency domain similar to that of a spectrum analyzer display. Unlike the spectrum analyzer where the RBW and VBW can be controlled the FFT span is determined by the sampling rate of the oscilloscope. Three key parameters characterize the FFT spectrum on an oscilloscope, i.e. the Nyquist frequency f_{Ny} which is the frequency span of the FFT, the frequency resolution Δf and the capture time t_{cap} of the oscilloscope which is the time over which the waveform is recorded. Note that in general the frequency span of FFT oscilloscopes start at 0 Hz and goes up to the span frequency. Hence, f_{Ny} is the maximum frequency displayed in the frequency domain. As initial settings the number of sample points N and the sampling period in the time domain ΔT can be chosen. These parameters are related as [125]

$$f_{\mathrm{Ny}} = \frac{1}{2\Delta T}, \tag{5.38}$$

$$t_{\mathrm{cap}} = N\Delta T, \tag{5.39}$$

$$\Delta f = \frac{1}{t_{\mathrm{cap}}} = \frac{1}{N\Delta T}. \tag{5.40}$$

16 The complementary error function erfc is defined as $\mathrm{erfc}(x) = 2/\sqrt{\pi}\int_x^{\infty} \exp(-z^2)dz$

It follows that the frequency resolution can be increased by choosing higher number of sample points N or a larger sampling period ΔT. However, choosing a larger sample period ΔT counters the Nyquist frequency resulting in a smaller frequency span. Hence, given a default memory length N a compromise in the sample period has to be made to reach a high Nyquist frequency at a reasonable resolution.

5.3.2 *Beat Note Signal*

In order to beat the master and Rydberg laser at the frequency of the FSR of the cavity, the Rydberg laser is tuned to approximately the same wavelength as the master laser, i.e. 798 nm. Further, the lasers are locked to adjacent cavity modes yielding a beat frequency of 1.5 GHz. The beat note signal is observed with the frequency doubled lasers due spatial constraints on the laser table. Given that the FSR is roughly 1.5 GHz a beat note signal at the a frequency of $f_{\text{beat}} = 3\,\text{GHz}$ is anticipated. This frequency is resolvable with the available spectrum analyzer and the FFT oscilloscope.

In Fig. 5.12 the beat note signal of the master and Rydberg laser is shown for the case where the two lasers are locked to adjacent cavity modes. The beat frequency is $f_{\text{beat}} = 2.9932\,\text{GHz}$ yielding a FSR of $\Delta\nu_{\text{FSR}} = 1.4966\,\text{GHz} \pm 0.0001\,\text{GHz}$ which is in very good agreement with the theoretical value $\Delta\nu_{\text{FSR,theo}} = 1.497\,\text{GHz}$. Several error sources can be eliminated. Fluctuations of the PDH frequency can be neglected as origin of the error. This is verified by measuring the frequency with the spectrum analyzer over 5 min. In that time no frequency deviations are observed within the resolution of the spectrum analyzer of 10 Hz. The deviation from the theoretical value is in the range of 100 kHz and therefore, the error in this measurement method mainly stems from electronic noise.

The servo bumps originating from the finite bandwidth of the feedback-loop specify the time scale on which the lock can react to distortions. The bandwidth of the servo bumps is determined to $0.6\,\text{MHz} \pm 0.2\,\text{MHz}$, with the same error as the beat note frequency. That corresponds to a reaction time of $\tau_{\text{lock}} = 1.7\,\mu\text{s} \pm 0.6\,\mu\text{s}$. For frequencies opposed to the servo bumps the sign of the phase shifter changes, hence the lock increases the deviation to the reference frequency instead of decreasing it.

The accurately measured value of the FSR allows to determine the length of the cavity precisely. The length and the FSR are related according to equation (5.3). Hence, the length of the cavity reads

$$L = 100.158\,\text{mm} \pm 0.007\,\text{mm}, \tag{5.41}$$

while the error is obtained from error propagation. The length of the cavity specified from the manufacturer is 100.1 mm. Thus, the experimental and theoretical value agree very well. As mentioned in section 5.2.1, the length of the cavity does not

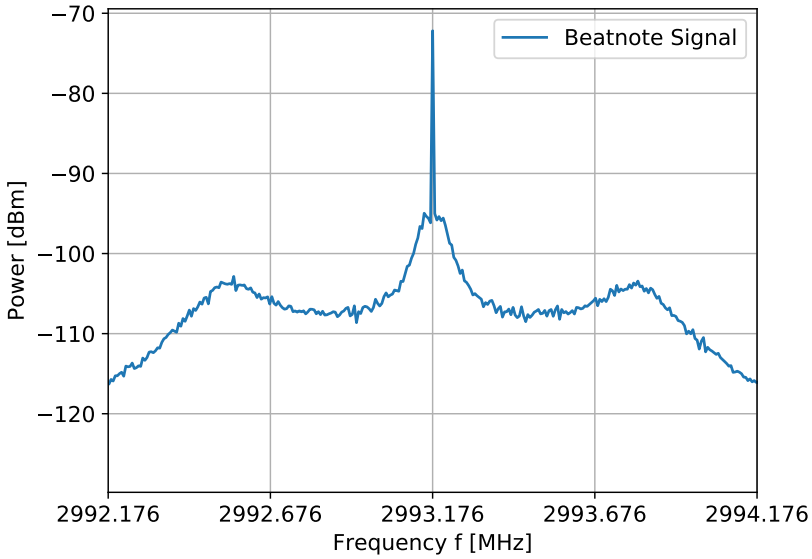

Figure 5.12: Beat note signal at $2\Delta\nu_{\mathrm{FSR}} = 2.9932\,\mathrm{GHz}$. Since the beat note signal is observed with the frequency doubled light of the lasers it has twice the FSR of the cavity. The RBW is 30 Hz and the VBW is 30 Hz.

coincide with the curvature of the concave mirror $R_2 = 500\,\mathrm{mm}$ to lift the degeneracy of higher transverse modes.

In order to determine the linewidth of the beat note signal it is shown in Fig. 5.13 with a reduced span. The beat note signal is plotted in a logarithmic and linear scale. The linear scale shows that the beat note signal solely consists of one data point highlighting that the resolution bandwidth of the spectrum analyzer is too low. The low resolution shows up in the logarithmic scale as well in terms of missing data points.

In order to increase the frequency resolution a FFT oscilloscope is used. For this device a capture time $t_{\mathrm{cap}} = 640\,\mathrm{ms}$ with a sampling period $\Delta T = 20\,\mathrm{ns}$ is chosen. This yields a frequency resolution $\Delta f = 1.56\,\mathrm{Hz}$ almost one magnitude higher than the RBW of the spectrum analyzer. The Nyquist frequency is $f_{\mathrm{Ny}} = 25\,\mathrm{MHz}$. Hence, a higher frequency resolution can be achieved but with a maximum beat frequency of 25 MHz.

The beat frequency is reduced by exploiting the sidebands generated from a rf-source in addition to the PDH frequency sidebands. Both lasers are locked on the rf-sideband to the same cavity mode. Hence, the frequency difference of the lasers is determined by the frequency difference of the rf-frequency. In particular, the sideband of the master laser is modulated at 410 MHz while the frequency sideband of the Rydberg laser is chosen to 400 MHz. Hence, the frequency difference of the diode lasers is 10 MHz while for the frequency doubled light it is 20 MHz, still

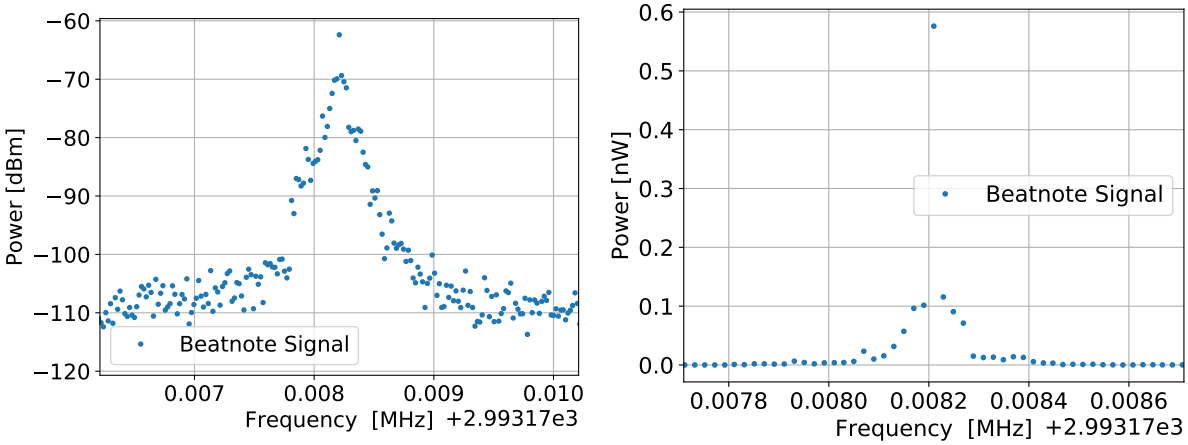

(a) **(b)**

Figure 5.13: Beat note signal detected on the spectrum analyzer with reduced span. **(a)** The beat note signal in logarithmic scale is plotted. **(b)** The beat note signal in linear scale is plotted. The resolution bandwidth of the spectrum analyzer is a limiting factor of resolving the linewidth.

significantly smaller than the FSR. The chosen parameters of the rf-sidebands allows the observation of the beat note signal with the FFT oscilloscope at the above assigned values. The beat note signal within a small span is shown in Fig. 5.14, again in logarithmic and linear scale.

Comparing the beat note signals in logarithmic scale in Fig. 5.13a and 5.14a, indeed a higher resolution is achieved. Further, the beat note signal in the linear scale consists of several data points. Based on this data set, the linewidth of the beat note can be extracted from the Voigtian and Lorentzian fit function. These functions are solely fitted to the data in the linear. In the logarithmic scale, the functions do not coincide with the data outside of the carrier. This indicates that an additional noise spectrum underlies the beat note signal presumably stemming from electronic noise. Given equation (5.37) and (5.35), the linewidth reads

$$\Delta\omega_{\mathrm{V,beat}} = 3\,\mathrm{Hz} \pm 4\,\mathrm{Hz}, \tag{5.42}$$

$$\Delta\omega_{\mathrm{L,beat}} = 4\,\mathrm{Hz} \pm 5\,\mathrm{Hz}. \tag{5.43}$$

The error is obtained from the fit parameters and both linewidths agree within the error range. A relatively large error follows from the fit parameters since the resolution limit 1.56 Hz of the FFT oscilloscope is almost reached.

A good agreement between the Voigtian and the Lorentzian distribution can be found, hence the Gaussian part of the Voigtian function contributes negligibly to the linewidth of the beat note. This indicates a high reduction of technical noise due to the lock performance. A relative reduction of approximately 10^{-4} with respect to the

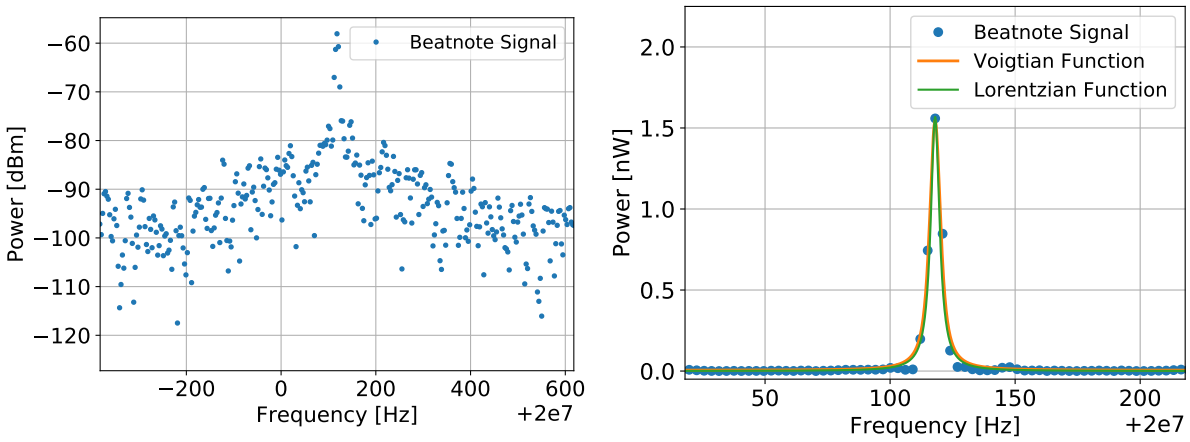

Figure 5.14: Beat note signal with increased resolution bandwidth on the FFT oscilloscope over a small span. A Voigtian and Lorentzian function are fitted to the data but can barely be distinguished due to the high overlap. **(a)** The beat note signal in logarithmic scale is plotted. **(b)** The beat note signal in linear scale with a Lorentzian and Voigtian function is plotted.

linewidth of the cavity is achieved. However, longterm drifts effectively increase the beatnote linewidth. This is analyzed in the following section.

5.3.3 *Characterization of the Cavity Lock*

The dependence of the beat note on the settings of the PID controller is discussed. Further, the longterm behavior of the beat note signal is analyzed.

Settings of the PID controller

The optical beat note signal is exploited as a diagnostic tool for the performance of the cavity lock. The PID controller settings are optimized such that the linewdith of the beatnote is minimal and the bandwidth of the servo bumps is maximal. Noise contributions to the beat note signal are discussed.

For the stabilization optimization of the laser frequency and the reduction of the laser linewidth the commercial PID controller FALC is used. Three switch panels consisting of a fast limited integrator *FLI*, fast limited differentiator *FLD* and slow limited integrator *SLI* with 10 different adjustments are used to control the transfer function of the controller. The optimized settings are shown in table 5.3.

In order to characterize in particular the noise sidebands of the beat note signal different settings of the *SLI* are investigated, shown in Fig. 5.15a, 5.15b. For decreasing *SLI* the linewidth of the beat note decreases as well. However, for too low *SLI* settings

Table 5.3: Optimized settings of the FALC.

LASER	*FLI*	*FLD*	*SLI*
Master laser	4	8	5
Rydberg laser	4	7	3

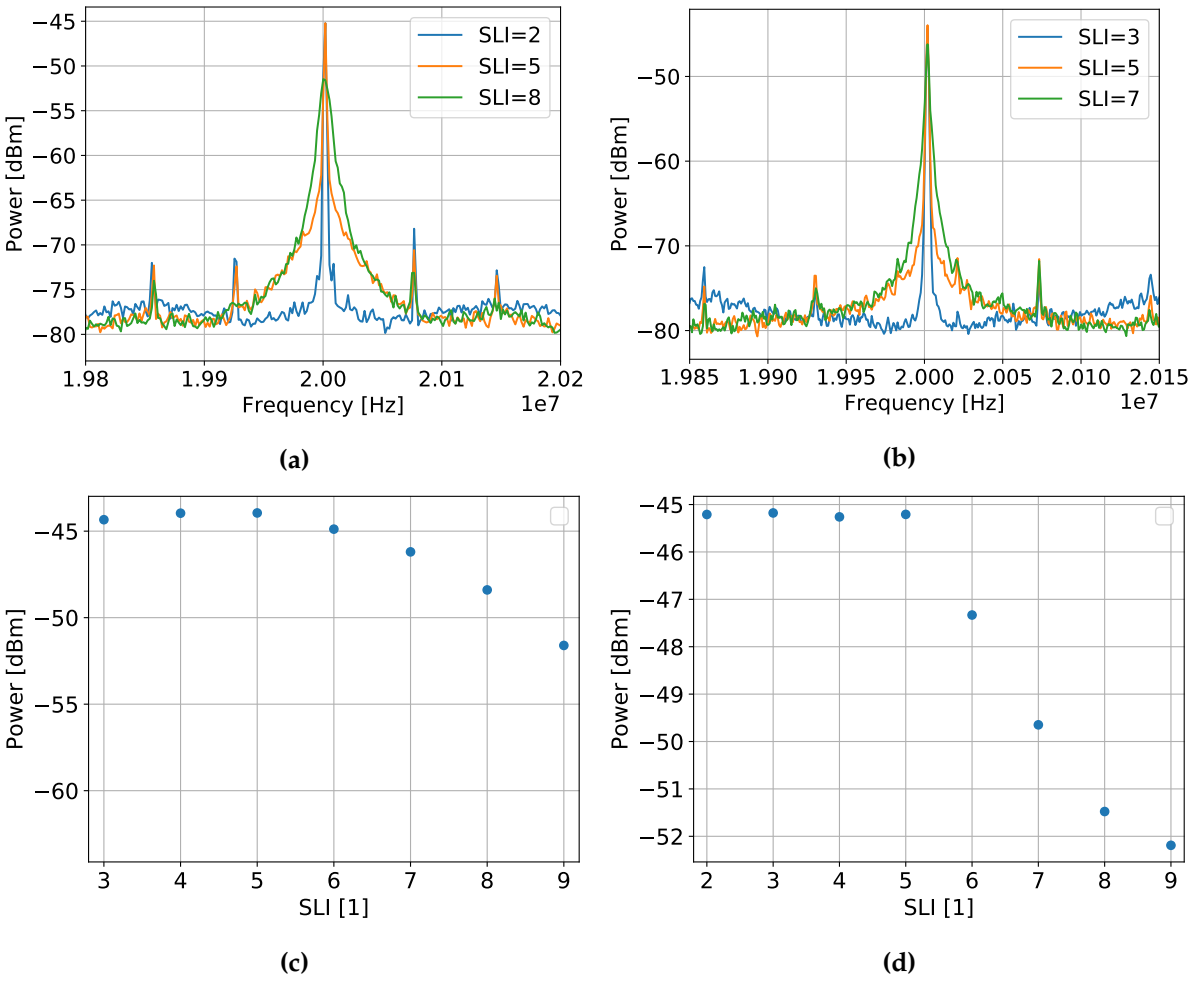

Figure 5.15: Optimization of the *SLI* settings of both lasers, left column master laser, right column Rydberg laser. **(a,b)** The beatnote signal is shown for three different *SLI* settings. **(c,d)** The amplitude of the beat note signal is shown in dependence on the *SLI* setting. The higher the amplitude the narrower the linewdith.

the bandwidth of the servobumps decreases, and becomes visible in the plot range (blue data line). Optimal performance is achieved when the power of the carrier is maximal. This is determined by extracting the amplitude of the beat note signal and plotting it over the *SLI* setting, Fig. 5.15d, 5.15c. Due to power conservation the area underneath the beat note must be constant, i.e. a higher beat note peak has the consequence of a narrower linewidth at constant carrier level above noise. The optimum parameters are $SLI_{\mathrm{m}} = 5$ and $SLI_{\mathrm{R}} = 3$ for the master and Rydberg laser, respectively.

Raising the beat note amplitude comes at the cost of additional noise sidebands at sub-100 kHz. These are altered by the slow limited integrator *SLI*. The sideband amplitudes behave reciprocal to the *SLI* settings, i.e. they decrease for increasing *SLI*. However, it is quite difficult to evaluate the source of the noise. The variation by *SLI* settings indicates a dependency on the lock electronics but the noise sidebands do not vanish completely for the *SLI* turned off. Possible noise sources in the sub-100 kHz range could be electronic components as for instance dc-dc-converters or non-perfect impedance matching of cable connections.

Several noise sources are investigated. It is checked that the acoustic noise in the laboratory can be neglected. The cable which carry the information of the lock signals are chosen minimally. Furthermore, worthwhile to mention, the local oscillator of the master and Rydberg laser for the generation of the frequency doubled laser light is chosen by TOPTICA at approximately 25 MHz. Therefore, cross-talk between the PDH frequency for locking the master laser to the cavity and the PDH frequency for locking the lasers to the internal SHG cavity is anticipated. Indeed, by increasing the amplitude of the local oscillator of either laser additional sidebands in the sub-100 kHz range occur but different to the sideband frequencies of the *SLI*. However, the amplitude is chosen such that the sidebands are below the noise level.

Note that the noise sidebands are not visible in Fig. 5.12. This is due to the incident power on the photodiode. For the characterization of the beat note linewidth a collimating lens $f = 50$ mm is placed in front of the photodiode rendering the sidebands above the noise level.

Longterm Drift

In order to quantify the longterm stability of the cavity lock the beat note signal is measured over a time scale of 35 min. The frequency and amplitude drifts are shown in Fig. 5.16. The first beat frequency and amplitude is set as the reference point, hence at time $t = 0$ s the frequency and amplitude deviation is zero.

The frequency drift is in the range of 40 Hz and predomeninantly caused by non-perfect polarization matching of the incoupling beam into the fiber EOM. This is observed by optimizing the incoupling polarization of one the lasers where the frequency oscillations were reduced from kHz to sub-100 Hz. The amplitude fluctuates

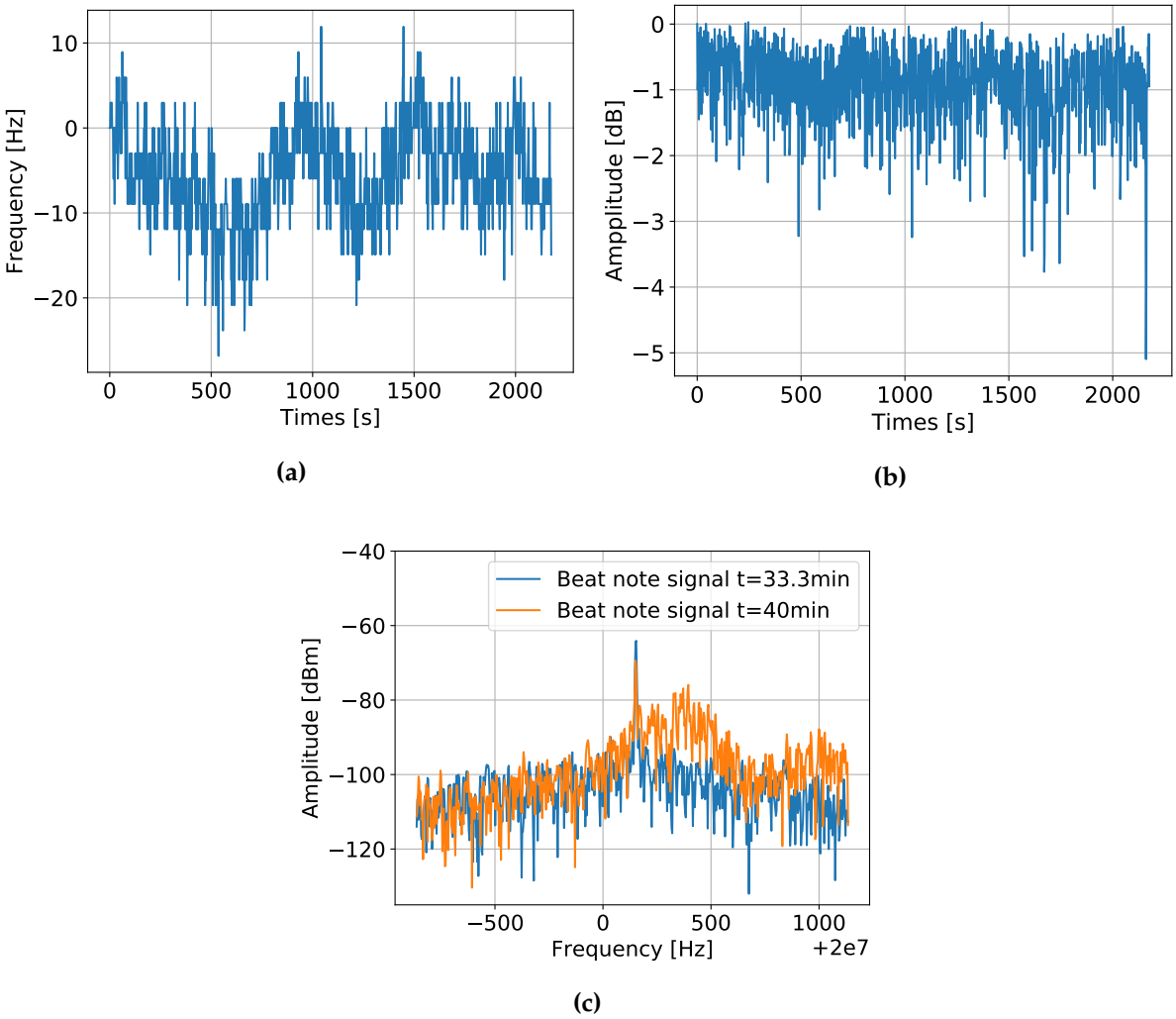

Figure 5.16: Longterm behavior of the beat note signal. **(a)** An oscillatory drift of the beat frequency is observable. **(b)** The ampitude drift is in the range of roughly 3 dB depending on the performance of the lasers. **(c)** An occurring 'shoulder' distorts the beat note signal (orange). In comparison, the beat note signal when both lasers are stable (blue).

in the range of 3 dB. Deviations in the range of up to 2 dB stem from the peak detection method and are not necessarily related to frequency or intensity fluctuations. Due to the finite resolution the maximum value in the plot is not unconditionally the peak value of the beat note but may lie on the slope which results in a lower amplitude.

However, it is believed that larger amplitude drops are caused by multi mode operation of the diode lasers. Another possibility is the lock performance of the piezo not being able to compensate for longterm drifts. Hence, the current is not sufficient to keep the laser locked. As an example, Fig. 5.16c shows the distorted beat note signal in comparison to an ideal signal. This behavior leads to the occurrence of a 'shoulder' disturbing the beat note signal in regards of the power in the carrier. Nevertheless, due to time constraints in the framework of this thesis this couldn't be investigated in more detail but is an important factor for the longterm stability of the lasers for future experiments.

6

SUMMARY AND OUTLOOK

6.1 SUMMARY

In the scope of this thesis a new, ultracold ytterbium experiment for nonlinear quantum optics based on Rydberg atoms was designed from the start and partly constructed. At the current status, the foundation of every quantum optics experiment was laid, i.e. the stabilization of the laser system to a frequency reference, in particular an ultrastable, high-finesse cavity is chosen for this setup. Due to time constraints, the assembly of the vacuum chamber could not be finished.

A thorough planning is inevitable in order to build a quantum optics experiment from the very start tailored to the individual requirements. Hence, the first period of the master's project was filled with comprehensive discussions spanning from the realization of the vacuum chamber design, the laser system setup, optical and mechanical designs and others. In that regard, several design decisions were established by the implementation and simulation of the encountered physics problems. This developed setup was presented in chapter 2. Crucial components of the design as the performance of the 2D MOT and the electric field control were theoretically modeled and verified with numerical simulations. The results of the atom trajectories in the 2D MOT were shown in chapter 3. These gave important inside on the characteristics of a 2D MOT which led to a better understanding, but also to the knowledge that additional protection measures of the glass cell are necessary to increase the lifetime of this expensive component. In chapter 4, the design of the electric field control was presented. This is a central part of a Rydberg physics experiment due to the high sensitivity of Rydberg atoms to electric fields. Here, simulations of the electric stray fields from the microchannel plate were examined verifying that the influence of the microchannel plate does not distort the Rydberg experiments. In addition, ion trajectory simulations were studied which demonstrated that with the chosen setup the ionized Rydberg core can be successfully steered on the microchannel plate.

However, the second period consisted of the construction of the so far planned experiment. The experiment was divided conceptually in two regimes: the laser table on which the laser stabilization and control takes place and the experiment table on which the actual experiments are performed. The first step towards a working experiment was the setup of the laser system which was discussed in chapter 5. In the scope of this thesis, focus was placed on the stabilization of the master, Rydberg

and 3D MOT laser to an ultrastable, high-finesse cavity with $\mathcal{F} \sim 40\,000$. The finesse of each laser was obtained experimentally with two independent methods both in good agreement with the theoretical specifications of the cavity supplier. Further, the coupling to the cavity and frequency stabilization by means of Pound-Drever-Hall technique were analyzed thoroughly. Here, the beat note signal of the master and Rydberg laser was exploited as a diagnostic tool allowing to determine the FSR $\Delta\nu_{\mathrm{FSR}} = 1.4966\,\mathrm{GHz} \pm 0.0001\,\mathrm{GHz}$ of the cavity with high precision and the shortterm laser linewidth to below 10 Hz but with a longterm drift of 75 Hz. Hence, yielding an upper limit of the effective laser linewidth still below 100 Hz.

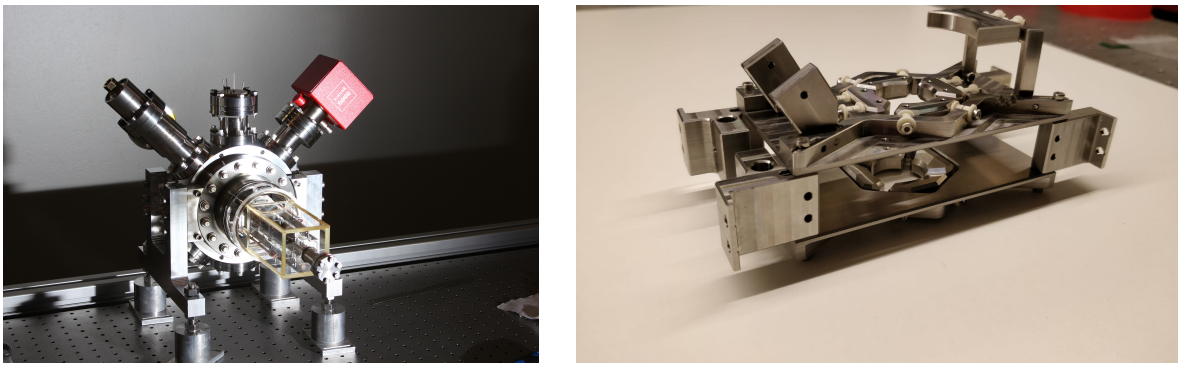

(a) **(b)**

Figure 6.1: Pictures of the status of the experiment at the submission date. **(a)** The 2D MOT chamber assembled by Simon Ball and Mohamed Noaman is shown. **(b)** The test assembly of the electric field control build by the author and Mohamad Noaman.

6.2 OUTLOOK

In less than one year, we designed and partly assembled a new ultracold Rydberg experiment from the very beginning. It aims for studying nonlinear quantum optics phenomena with the novel approach of exploiting the advantages of the alkaline-earth-like element ytterbium being an ideal candidate for exploring new realms of elementary quantum physics.

To the submission date of the thesis the 2D MOT chamber is assembled and a test assembly of the electric field control was done, see Fig. 6.1. Further, all pieces for the whole vacuum setup have arrived in our laboratory. Hence, the plan for the next months is straightforward: The vacuum chambers will be assembled, baked out and subsequently the 2D MOT chamber will be pumped to ultra-high vacuum around 10^{-9} mbar and the science chamber to around 10^{-11} mbar. Given that the vacuum assembly and pumping works successfully we are looking forward to creating an ytterbium 2D MOT in spring 2019.

BIBLIOGRAPHY

[1] Ofer Firstenberg, Charles Adams, and Sebastian Hofferberth. „Nonlinear quantum optics mediated by Rydberg interactions.“ In: *Journal of Physics B: Atomic, Molecular and Optical Physics* 49 (Feb. 2016). DOI: 10.1088/0953-4075/49/15/152003 (cit. on p. 1).

[2] P. Bienias, S. Choi, O. Firstenberg, M. F. Maghrebi, M. Gullans, M. D. Lukin, A. V. Gorshkov, and H. P. Büchler. „Scattering resonances and bound states for strongly interacting Rydberg polaritons.“ In: *Phys. Rev. A* 90 (5 2014), p. 053804. DOI: 10.1103/PhysRevA.90.053804 (cit. on pp. 1, 2).

[3] Johannes Otterbach, Matthias Moos, Dominik Muth, and Michael Fleischhauer. „Wigner Crystallization of Single Photons in Cold Rydberg Ensembles.“ In: *Phys. Rev. Lett.* 111 (11 2013), p. 113001. DOI: 10.1103/PhysRevLett.111.113001 (cit. on pp. 1, 2).

[4] Matthias Moos, Michael Höning, Razmik Unanyan, and Michael Fleischhauer. „Many-body physics of Rydberg dark-state polaritons in the strongly interacting regime.“ In: *Phys. Rev. A* 92 (5 2015), p. 053846. DOI: 10.1103/PhysRevA.92.053846. URL: https://link.aps.org/doi/10.1103/PhysRevA.92.053846 (cit. on p. 1).

[5] Ofer Firstenberg, Thibault Peyronel, Qi-Yu Liang, Alexey Gorshkov, Mikhail D Lukin, and Vladan Vuletic. „Attractive photons in a quantum nonlinear medium.“ In: *Nature* 502 (Sept. 2013). DOI: 10.1038/nature12512 (cit. on p. 1).

[6] Richard P. Feynman. „Simulating physics with computers.“ In: *International Journal of Theoretical Physics* 21.6 (1982), pp. 467–488. ISSN: 1572-9575. DOI: 10.1007/BF02650179 (cit. on p. 1).

[7] Michael A. Nielsen and Isaac L. Chuang. *Quantum Computation and Quantum Information: 10th Anniversary Edition*. Cambridge University Press, 2010. DOI: 10.1017/CBO9780511976667 (cit. on p. 1).

[8] H John Caulfield and Shlomi Dolev. „Why future supercomputing requires optics.“ In: *Nat. Photonics* 4 (May 2010). DOI: 10.1038/nphoton.2010.94 (cit. on p. 1).

[9] P. A. Franken, A. E. Hill, C. W. Peters, and G. Weinreich. „Generation of Optical Harmonics.“ In: *Phys. Rev. Lett.* 7 (4 1961), pp. 118–119. DOI: 10.1103/PhysRevLett.7.118 (cit. on p. 1).

[10] Tatjana Wilk, Simon C. Webster, Axel Kuhn, and Gerhard Rempe. „Single-Atom Single-Photon Quantum Interface." In: *Science* 317.5837 (2007), pp. 488–490. ISSN: 0036-8075. DOI: 10.1126/science.1143835. eprint: http://science.sciencemag.org/content/317/5837/488.full.pdf (cit. on p. 1).

[11] Danny O'Shea, Christian Junge, Jürgen Volz, and Arno Rauschenbeutel. „Fiber-Optical Switch Controlled by a Single Atom." In: *Phys. Rev. Lett.* 111 (19 2013), p. 193601. DOI: 10.1103/PhysRevLett.111.193601 (cit. on p. 1).

[12] Thomas F. Gallagher. *Rydberg Atoms*. Cambridge Monographs on Atomic, Molecular and Chemical Physics. Cambridge University Press, 1994. DOI: 10.1017/CBO9780511524530 (cit. on p. 1).

[13] M. Saffman, T. G. Walker, and K. Mølmer. „Quantum information with Rydberg atoms." In: *Rev. Mod. Phys.* 82 (3 2010), pp. 2313–2363. DOI: 10.1103/RevModPhys.82.2313 (cit. on p. 1).

[14] Inbal Friedler, David Petrosyan, Michael Fleischhauer, and Gershon Kurizki. „Long-range interactions and entanglement of slow single-photon pulses." In: *Phys. Rev. A* 72 (4 2005), p. 043803. DOI: 10.1103/PhysRevA.72.043803 (cit. on pp. 1, 2).

[15] Sebastian Weber, Christoph Tresp, Henri Menke, Alban Urvoy, Ofer Firstenberg, Hans Peter Büchler, and Sebastian Hofferberth. „Calculation of Rydberg interaction potentials." In: *Journal of Physics B: Atomic, Molecular and Optical Physics* 50.13 (2017), p. 133001 (cit. on p. 1).

[16] M. D. Lukin, M. Fleischhauer, R. Cote, L. M. Duan, D. Jaksch, J. I. Cirac, and P. Zoller. „Dipole Blockade and Quantum Information Processing in Mesoscopic Atomic Ensembles." In: *Phys. Rev. Lett.* 87 (3 2001), p. 037901. DOI: 10.1103/PhysRevLett.87.037901 (cit. on p. 1).

[17] Y. O. Dudin and A. Kuzmich. „Strongly Interacting Rydberg Excitations of a Cold Atomic Gas." In: *Science* 336.6083 (2012), pp. 887–889. ISSN: 0036-8075. DOI: 10.1126/science.1217901. eprint: http://science.sciencemag.org/content/336/6083/887.full.pdf (cit. on p. 1).

[18] Asaf Paris-Mandoki, Christoph Braun, Jan Kumlin, Christoph Tresp, Ivan Mirgorodskiy, Florian Christaller, Hans Peter Büchler, and Sebastian Hofferberth. „Free-Space Quantum Electrodynamics with a Single Rydberg Superatom." In: *Phys. Rev. X* 7 (4 2017), p. 041010. DOI: 10.1103/PhysRevX.7.041010 (cit. on p. 1).

[19] Michael Fleischhauer, Atac Imamoglu, and Jonathan P. Marangos. „Electromagnetically induced transparency: Optics in coherent media." In: *Rev. Mod. Phys.* 77 (2 2005), pp. 633–673. DOI: 10.1103/RevModPhys.77.633 (cit. on p. 1).

[20] M. Fleischhauer and M. D. Lukin. „Dark-State Polaritons in Electromagnetically Induced Transparency.“ In: *Phys. Rev. Lett.* 84 (22 2000), pp. 5094–5097. DOI: 10.1103/PhysRevLett.84.5094 (cit. on p. 1).

[21] Lene Vestergaard Hau, S E. Harris, Zachary Dutton, and Cyrus H. Behroozi. „Hau, L. V., Harris, S. E., Dutton, Z. and Behroozi, C. H. Light speed reduction to 17 m per second in an ultracold atomic gas. Nature 397, 594-598.“ In: *Nature* 397 (Feb. 1999). DOI: 10.1038/17561 (cit. on p. 1).

[22] J. D. Pritchard, D. Maxwell, A. Gauguet, K. J. Weatherill, M. P. A. Jones, and C. S. Adams. „Cooperative Atom-Light Interaction in a Blockaded Rydberg Ensemble.“ In: *Phys. Rev. Lett.* 105 (19 2010), p. 193603. DOI: 10.1103/PhysRevLett.105.193603 (cit. on p. 2).

[23] Thibault Michel Max Peyronel, Ofer Firstenberg, Qi-Yu Liang, Sebastian Hofferberth, Alexey Gorshkov, Thomas Pohl, Mikhail D Lukin, and Vladan Vuletic. „Quantum nonlinear optics with single photons enabled by strongly interacting atoms.“ In: *Nature* 488 (July 2012), pp. 57–60. DOI: 10.1038/nature11361 (cit. on p. 2).

[24] D. Maxwell, D. J. Szwer, D. Paredes-Barato, H. Busche, J. D. Pritchard, A. Gauguet, K. J. Weatherill, M. P. A. Jones, and C. S. Adams. „Storage and Control of Optical Photons Using Rydberg Polaritons.“ In: *Phys. Rev. Lett.* 110 (10 2013), p. 103001. DOI: 10.1103/PhysRevLett.110.103001 (cit. on p. 2).

[25] Ofer Firstenberg, Thibault Peyronel, Qi-Yu Liang, Alexey Gorshkov, Mikhail D Lukin, and Vladan Vuletic. „Attractive photons in a quantum nonlinear medium.“ In: *Nature* 502 (Sept. 2013). DOI: 10.1038/nature12512 (cit. on p. 2).

[26] Nina Stiesdal, Jan Kumlin, Kevin Kleinbeck, Philipp Lunt, Christoph Braun, Asaf Paris-Mandoki, Christoph Tresp, Hans Peter Büchler, and Sebastian Hofferberth. „Observation of Three-Body Correlations for Photons Coupled to a Rydberg Superatom.“ In: *Phys. Rev. Lett.* 121 (10 2018), p. 103601. DOI: 10.1103/PhysRevLett.121.103601 (cit. on p. 2).

[27] Alexey V. Gorshkov, Johannes Otterbach, Michael Fleischhauer, Thomas Pohl, and Mikhail D. Lukin. „Photon-Photon Interactions via Rydberg Blockade.“ In: *Phys. Rev. Lett.* 107 (13 2011), p. 133602. DOI: 10.1103/PhysRevLett.107.133602 (cit. on p. 2).

[28] M. J. Gullans, J. D. Thompson, Y. Wang, Q.-Y. Liang, V. Vuletic, M. D. Lukin, and A. V. Gorshkov. „Effective Field Theory for Rydberg Polaritons.“ In: *Phys. Rev. Lett.* 117 (11 2016), p. 113601. DOI: 10.1103/PhysRevLett.117.113601 (cit. on p. 2).

[29] Krzysztof Jachymski, Przemysław Bienias, and Hans Peter Büchler. „Three-Body Interaction of Rydberg Slow-Light Polaritons." In: *Phys. Rev. Lett.* 117 (5 2016), p. 053601. DOI: 10.1103/PhysRevLett.117.053601 (cit. on p. 2).

[30] C. Gaul, B. J. DeSalvo, J. A. Aman, F. B. Dunning, T. C. Killian, and T. Pohl. „Resonant Rydberg Dressing of Alkaline-Earth Atoms via Electromagnetically Induced Transparency." In: *Phys. Rev. Lett.* 116 (24 2016), p. 243001. DOI: 10.1103/PhysRevLett.116.243001 (cit. on pp. 2, 5).

[31] F B Dunning, T C Killian, S Yoshida, and J Burgdörfer. „Recent advances in Rydberg physics using alkaline-earth atoms." In: *Journal of Physics B: Atomic, Molecular and Optical Physics* 49 (June 2016), p. 112003. DOI: 10.1088/0953-4075/49/11/112003 (cit. on p. 2).

[32] J. Millen, G. Lochead, and M. P. A. Jones. „Two-Electron Excitation of an Interacting Cold Rydberg Gas." In: *Phys. Rev. Lett.* 105 (21 2010), p. 213004. DOI: 10.1103/PhysRevLett.105.213004 (cit. on p. 2).

[33] D. P. Sadler, E. M. Bridge, D. Boddy, A. D. Bounds, N. C. Keegan, G. Lochead, M. P. A. Jones, and B. Olmos. „Radiation trapping in a dense cold Rydberg gas." In: *Phys. Rev. A* 95 (1 2017), p. 013839. DOI: 10.1103/PhysRevA.95.013839 (cit. on p. 2).

[34] Ryan K Hanley, Alistair D Bounds, Paul Huillery, Niamh C Keegan, Riccardo Faoro, Elizabeth M Bridge, Kevin J Weatherill, and Matthew P A Jones. „Probing interactions of thermal Sr Rydberg atoms using simultaneous optical and ion detection." In: *Journal of Physics B: Atomic, Molecular and Optical Physics* 50.11 (2017), p. 115002. URL: http://stacks.iop.org/0953-4075/50/i=11/a=115002 (cit. on p. 2).

[35] Santosh Pisharody. „Electron Dynamics in double Rydberg Wavepackets." PhD Thesis. Technical Institute of Technology, Bombay, 2003 (cit. on p. 2).

[36] S. N. Pisharody and R. R. Jones. „Probing Two-Electron Dynamics of an Atom." In: *Science* 303.5659 (2004), pp. 813–815. ISSN: 0036-8075. DOI: 10.1126/science.1092220. URL: http://science.sciencemag.org/content/303/5659/813 (cit. on p. 2).

[37] R Mukherjee, J Millen, R Nath, M P A Jones, and T Pohl. „Many-body physics with alkaline-earth Rydberg lattices." In: *Journal of Physics B: Atomic, Molecular and Optical Physics* 44.18 (2011), p. 184010. URL: http://stacks.iop.org/0953-4075/44/i=18/a=184010 (cit. on p. 2).

[38] C. Tresp, C. Zimmer, I. Mirgorodskiy, H. Gorniaczyk, A. Paris-Mandoki, and S. Hofferberth. „Single-Photon Absorber Based on Strongly Interacting Rydberg Atoms." In: *Phys. Rev. Lett.* 117 (22 2016), p. 223001. DOI: 10.1103/PhysRevLett.117.223001 (cit. on p. 3).

[39] Hannes Gorniaczyk, Christoph Tresp, Przemek Bienias, Asaf Paris Mandoki, Weibin Li, I Mirgorodskiy, H P. Büchler, Igor Lesanovsky, and S Hofferberth. „Enhancement of Rydberg-mediated single-photon nonlinearities by electrically tuned Förster resonances." In: *Nature Communications* 7 (July 2016). DOI: 10.1038/ncomms12480 (cit. on pp. 3, 9).

[40] Asaf Paris-Mandoki, Hannes Gorniaczyk, Christoph Tresp, Ivan Mirgorodskiy, and Sebastian Hofferberth. „Tailoring Rydberg interactions via Förster resonances: state combinations, hopping and angular dependence." In: *Journal of Physics B: Atomic, Molecular and Optical Physics* 49.16 (2016), p. 164001. URL: http://stacks.iop.org/0953-4075/49/i=16/a=164001 (cit. on p. 3).

[41] Y. Takasu, K. Honda, K. Komori, T. Kuwamoto, M. Kumakura, Y. Takahashi, and T. Yabuzaki. „High-Density Trapping of Cold Ytterbium Atoms by an Optical Dipole Force." In: *Phys. Rev. Lett.* 90 (2 2003), p. 023003. DOI: 10.1103/PhysRevLett.90.023003 (cit. on pp. 5, 9, 13, 22).

[42] Takeshi Fukuhara, Yosuke Takasu, Mitsutaka Kumakura, and Yoshiro Takahashi. „Degenerate Fermi Gases of Ytterbium." In: *Phys. Rev. Lett.* 98 (3 2007), p. 030401. DOI: 10.1103/PhysRevLett.98.030401 (cit. on pp. 5, 11).

[43] L Franchi, L F Livi, G Cappellini, G Binella, M Inguscio, J Catani, and L Fallani. „State-dependent interactions in ultracold 174 Yb probed by optical clock spectroscopy." In: *New Journal of Physics* 19.10 (2017), p. 103037 (cit. on p. 5).

[44] Francesco Scazza. „Probing SU(N)-symmetric orbital interactions with ytterbium Fermi gases in optical lattices." PhD Thesis. Munich University, 2015 (cit. on pp. 5, 8, 9).

[45] Takuya Kohno, Masami Yasuda, Kazumoto Hosaka, Hajime Inaba, Yoshiaki Nakajima, and Feng-Lei Hong. „One-Dimensional Optical Lattice Clock with a Fermionic 171 Yb Isotope." In: *Applied Physics Express* 2.7 (2009), p. 072501 (cit. on p. 5).

[46] Koen Sponselee et al. „Dynamics of Ultracold Quantum Gases in the Dissipative Fermi-Hubbard Model." In: *arXiv* (2018). DOI: arXiv:1805.11853 (cit. on p. 5).

[47] Alexey Gorshkov, Michael Hermele, V Gurarie, C Xu, Paul Julienne, Jun Ye, P Zoller, Eugene Demler, M D. Lukin, and Ana Rey. „Two-orbital SU(N) magnetism with ultracold alkaline-earth atoms." In: *Nature Physics* 6 (Feb. 2010), p. 289. DOI: 10.1038/NPHYS1535 (cit. on p. 5).

[48] Y. Wang, S. Subhankar, P. Bienias, M. Łącki, T-C. Tsui, M. A. Baranov, A. V. Gorshkov, P. Zoller, J. V. Porto, and S. L. Rolston. „Dark State Optical Lattice with a Subwavelength Spatial Structure." In: *Phys. Rev. Lett.* 120 (8 2018), p. 083601. DOI: 10.1103/PhysRevLett.120.083601 (cit. on p. 5).

[49] Shintaro Taie, Rekishu Yamazaki, Seiji Sugawa, and Yoshiro Takahashi. „An SU(N) Mott insulator of an atomic Fermi gas realized by large-spin Pomeranchuk cooling." In: *Nature Physics* 8 (Aug. 2012). DOI: 10.1038/nphys2430 (cit. on p. 5).

[50] William McGrew et al. „Atomic clock performance enabling geodesy below the centimetre level." In: *Nature* 564 (Nov. 2018). DOI: 10.1038/s41586-018-0738-2 (cit. on p. 5).

[51] Jacopo Grotti et al. „Geodesy and metrology with a transportable optical clock." In: *Nature Physics* 14 (May 2017). DOI: 10.1038/s41567-017-0042-3 (cit. on p. 5).

[52] C L Vaillant, M P A Jones, and R M Potvliege. „Long-range Rydberg–Rydberg interactions in calcium, strontium and ytterbium." In: *Journal of Physics B: Atomic, Molecular and Optical Physics* 45.13 (2012), p. 135004. URL: http://stacks.iop.org/0953-4075/45/i=13/a=135004 (cit. on pp. 5, 36).

[53] Ryuta Yamamoto, Jun Kobayashi, Takuma Kuno, Kohei Kato, and Yoshiro Takahashi. „An ytterbium quantum gas microscope with narrow-line laser cooling." In: *New Journal of Physics* 18.2 (2016), p. 023016. URL: http://stacks.iop.org/1367-2630/18/i=2/a=023016 (cit. on p. 5).

[54] Emanuele Distante, Pau Farrera, Auxiliadora Padrón, David Paredes-Barato, Georg Heinze, and Hugues de Riedmatten. „Storing single photons emitted by a quantum memory on a highly excited Rydberg state." In: *Nature Communications* 8 (Jan. 2017), p. 14072. DOI: 10.1038/ncomms14072 (cit. on pp. 5, 10).

[55] A.F. Hollemann. *Lehrbuch der anorganischen Chemie*. Walter de Gruyter, 1995 (cit. on p. 5).

[56] Sören Dörscher. „Creation of ytterbium quantum gases with a compact 2D-/3D-MOT setup." PhD Thesis. Universität Hamburg, 2013 (cit. on pp. 6–9, 13, 15, 16, 18, 21, 27, 42).

[57] Reina Maruyama. „Optical trapping of ytterbium atoms." PhD Thesis. Washington University, 2003 (cit. on pp. 6, 8).

[58] Massimo Inguscio and Leonardo Fallani. *Atomic Physics - Precise Measurements and Ultracold Matter*. Great Clarendon Street - Oxford - OX2 6DP, United Kingdom: Oxford University Press, 2015, 155 ff (cit. on p. 6).

[59] Michael Berglund and Michael Wieser. „Isotopic compostions of the elements 2009 (IUPAC technical report).“ In: *Pure and Applied Chemistry* 83.2 (2011), pp. 48,49. DOI: 10.1351/PAC-REP-10-06-02 (cit. on p. 6).

[60] G. Audi, A.H. Wapstra, and C. Thibault. „The AME2003 atomic mass evaluation - (II). Tables, graphs and references.“ working paper or preprint. Dec. 2003. URL: http://hal.in2p3.fr/in2p3-00014186 (cit. on p. 6).

[61] C. J. Foot. *Atomic Physics*. Great Clarendon Street, Oxford OX2 6DP: Oxford Master Series in Physics, 2005 (cit. on p. 6).

[62] Y. Takasu, K. Komori, K. Honda, M. Kumakura, T. Yabuzaki, and Y. Takahashi. „Photoassociation Spectroscopy of Laser-Cooled Ytterbium Atoms.“ In: *Phys. Rev. Lett.* 93 (12 2004), p. 123202. DOI: 10.1103/PhysRevLett.93.123202 (cit. on p. 8).

[63] P. van der Straaten H.J. Metcalf. *Laser cooling and trapping*. New York, USA: Springer, 1999 (cit. on p. 8).

[64] K. Beloy, J. A. Sherman, N. D. Lemke, N. Hinkley, C. W. Oates, and A. D. Ludlow. „Determination of the $5d6s\ ^3D_1$ state lifetime and blackbody-radiation clock shift in Yb.“ In: *Phys. Rev. A* 86 (5 2012), p. 051404. DOI: 10.1103/PhysRevA.86.051404 (cit. on p. 8).

[65] C. J. Bowers, D. Budker, E. D. Commins, D. DeMille, S. J. Freedman, A.-T. Nguyen, S.-Q. Shang, and M. Zolotorev. „Experimental investigation of excited-state lifetimes in atomic ytterbium.“ In: *Phys. Rev. A* 53 (5 1996), pp. 3103–3109. DOI: 10.1103/PhysRevA.53.3103 (cit. on p. 8).

[66] J Migdalek and W E Baylis. „Relativistic transition probabilities and lifetimes of low-lying levels in ytterbium.“ In: *Journal of Physics B: Atomic, Molecular and Optical Physics* 24.4 (1991), p. L99. URL: http://stacks.iop.org/0953-4075/24/i=4/a=001 (cit. on p. 8).

[67] H. Lehec, A. Zuliani, W. Maineult, E. Luc-Koenig, P. Pillet, P. Cheinet, F. Niyaz, and T. F. Gallagher. „Laser and microwave spectroscopy of even-parity Rydberg states of neutral ytterbium and multichannel-quantum-defect-theory analysis.“ In: *Phys. Rev. A* 98 (6 2018), p. 062506. DOI: 10.1103/PhysRevA.98.062506. URL: https://link.aps.org/doi/10.1103/PhysRevA.98.062506 (cit. on pp. 8, 34).

[68] Mukherjee Rick. „Strong interactions in alkaline-earth Rydberg ensembles.“ PhD Thesis. Universität Dresden, Max-Planck Institut für Physik komplexer Systeme, 2013 (cit. on p. 9).

[69] Thomas Niederprüm, Oliver Thomas, Torsten Manthey, Tobias M. Weber, and Herwig Ott. „Giant Cross Section for Molecular Ion Formation in Ultracold Rydberg Gases.“ In: *Phys. Rev. Lett.* 115 (1 2015), p. 013003. DOI: 10.1103/PhysRevLett.115.013003 (cit. on p. 9).

[70] Jeongwon Lee, Jae Hoon Lee, Jiho Noh, and Jongchul Mun. „Core-shell magneto-optical trap for alkaline-earth-metal-like atoms.“ In: *Phys. Rev. A* 91 (5 2015), p. 053405. DOI: 10.1103/PhysRevA.91.053405 (cit. on pp. 9, 13, 15, 16, 21, 22, 27, 41, 42).

[71] Hannes Busche, Simon W. Ball, and Paul Huillery. „A high repetition rate experimental setup for quantum non-linear optics with cold Rydberg atoms.“ In: *The European Physical Journal Special Topics* 225.15 (2016), pp. 2839–2861 (cit. on pp. 10, 26).

[72] A Gaj, Alexander Krupp, Jonathan Balewski, R Löw, S Hofferberth, and Tilman Pfau. „From molecular spectra to a density shift in dense Rydberg gases.“ In: *Nature communications* 5 (Aug. 2014), p. 4546. DOI: 10.1038/ncomms5546 (cit. on p. 10).

[73] Ivan Mirgorodskiy, Florian Christaller, Christoph Braun, Asaf Paris-Mandoki, Christoph Tresp, and Sebastian Hofferberth. „Electromagnetically induced transparency of ultra-long-range Rydberg molecules.“ In: *Phys. Rev. A* 96 (1 2017), p. 011402. DOI: 10.1103/PhysRevA.96.011402 (cit. on p. 10).

[74] Chris H. Greene, A. S. Dickinson, and H. R. Sadeghpour. „Creation of Polar and Nonpolar Ultra-Long-Range Rydberg Molecules.“ In: *Phys. Rev. Lett.* 85 (12 2000), pp. 2458–2461. DOI: 10.1103/PhysRevLett.85.2458 (cit. on p. 10).

[75] F. Camargo, J. D. Whalen, R. Ding, H. R. Sadeghpour, S. Yoshida, J. Burgdörfer, F. B. Dunning, and T. C. Killian. „Lifetimes of ultra-long-range strontium Rydberg molecules.“ In: *Phys. Rev. A* 93 (2 2016), p. 022702. DOI: 10.1103/PhysRevA.93.022702 (cit. on p. 10).

[76] Stefano Giorgini, Lev P. Pitaevskii, and Sandro Stringari. „Theory of ultracold atomic Fermi gases.“ In: *Rev. Mod. Phys.* 80 (4 2008), pp. 1215–1274. DOI: 10.1103/RevModPhys.80.1215 (cit. on p. 11).

[77] T. G. Tiecke, S. D. Gensemer, A. Ludewig, and J. T. M. Walraven. „High-flux two-dimensional magneto-optical-trap source for cold lithium atoms.“ In: *Phys. Rev. A* 80 (1 2009), p. 013409. DOI: 10.1103/PhysRevA.80.013409 (cit. on pp. 13, 18).

[78] Markus Greiner, Immanuel Bloch, Theodor W. Hänsch, and Tilman Esslinger. „Magnetic transport of trapped cold atoms over a large distance.“ In: *Phys. Rev. A* 63 (3 2001), p. 031401. DOI: 10.1103/PhysRevA.63.031401 (cit. on p. 13).

[79] T. L. Gustavson, A. P. Chikkatur, A. E. Leanhardt, A. Görlitz, S. Gupta, D. E. Pritchard, and W. Ketterle. „Transport of Bose-Einstein Condensates with Optical Tweezers.“ In: *Phys. Rev. Lett.* 88 (2 2001), p. 020401. DOI: 10.1103/PhysRevLett.88.020401 (cit. on p. 13).

[80] T. Kuwamoto, K. Honda, Y. Takahashi, and T. Yabuzaki. „Magneto-optical trapping of Yb atoms using an intercombination transition.“ In: *Phys. Rev. A* 60 (2 1999), R745–R748. DOI: 10.1103/PhysRevA.60.R745. URL: https://link.aps.org/doi/10.1103/PhysRevA.60.R745 (cit. on pp. 13, 22, 42).

[81] Akio Kawasaki, Boris Braverman, QinQin Yu, and Vladan Vuletic. „Two-color magneto-optical trap with small magnetic field for ytterbium.“ In: *Journal of Physics B: Atomic, Molecular and Optical Physics* 48.15 (2015), p. 155302. URL: http://stacks.iop.org/0953-4075/48/i=15/a=155302 (cit. on p. 13).

[82] Sören Dörscher, Alexander Thobe, Bastian Hundt, André Kochanke, Rodolphe Le Targat, Patrick Windpassinger, Christoph Becker, and Klaus Sengstock. „Creation of quantum-degenerate gases of ytterbium in a compact 2D-/3D-magneto-optical trap setup.“ In: *Review of Scientific Instruments* 84.4 (2013), p. 043109. DOI: 10.1063/1.4802682 (cit. on p. 13).

[83] S. A. Hopkins, K. Butler, A. Guttridge, S. Kemp, R. Freytag, E. A. Hinds, M. R. Tarbutt, and S. L. Cornish. „A versatile dual-species Zeeman slower for caesium and ytterbium.“ In: *Review of Scientific Instruments* 87.4 (2016), p. 043109. DOI: 10.1063/1.4945795 (cit. on p. 13).

[84] Pfeiffer Vacuum. *The Vacuum Technology Book Volume II - Know How Book*. Asslar, Germany: Pfeiffer Vacuum, 2012 (cit. on p. 15).

[85] K. Metzger. „Dreidimensionale Feldberechnung starr magnetisierter Permanentmagnete mit einer Anwendung in eisenlosen, elektrischen Maschinen.“ In: *Archiv für Elektrotechnik* 59 (1977), pp. 229 –242 (cit. on p. 16).

[86] H. Metcalf T. Bergmann G. Erez. „Magnetostatic trapping fields for neutral atoms.“ In: *Physical Review A* 35.4 (1987) (cit. on p. 16).

[87] Bastian Höltkemeier. „2D MOT as a source of a cold atom target.“ Diploma Thesis. Universität Heidelberg, 2011 (cit. on p. 18).

[88] Martin Miranda. „Quantum gas microscope for ytterbium atoms.“ PhD Thesis. Tokyo Institute of Technology (cit. on p. 19).

[89] N. Hinkley, J. A. Sherman, N. B. Phillips, M. Schioppo, N. D. Lemke, K. Beloy, M. Pizzocaro, C. W. Oates, and A. D. Ludlow. „An Atomic Clock with 10–18 Instability.“ In: *Science* 341.6151 (2013), pp. 1215–1218. DOI: 10.1126/science.1240420 (cit. on p. 19).

[90] Creston Herold. „Ultracold mixtures of rubidium and ytterbium for open quantum system engineering.“ PhD Thesis. University of Maryland, 2014 (cit. on p. 21).

[91] Ad Lagendijk Tom Savels Allard Mosk. „Dynamics of a two-level atom in a broadband light field.“ In: *ArXiv* (2004). URL: https://arxiv.org/pdf/cond-mat/0410661v2.pdf (cit. on p. 22).

[92] Stefan Liam Kemp. „Laser cooling and optical trapping of Ytterbium.“ PhD Thesis. Durham University, 2017 (cit. on p. 22).

[93] Anders H. Hansen, Alexander Khramov, William H. Dowd, Alan O. Jamison, Vladyslav V. Ivanov, and Subhadeep Gupta. „Quantum degenerate mixture of ytterbium and lithium atoms.“ In: *Phys. Rev. A* 84 (1 2011), p. 011606. DOI: 10.1103/PhysRevA.84.011606 (cit. on p. 22).

[94] Yoann Bruneau, Guyve Khalili, Pierre Pillet, and Daniel Comparat. „Guided and focused slow atomic beam from a 2 dimensional magneto optical trap.“ In: *The European Physical Journal D* 68.4 (Apr. 2014), 10.1140/epjd/e2014–40389–y. URL: https://hal.archives-ouvertes.fr/hal-00981456 (cit. on p. 23).

[95] J. Schoser, A. Batär, R. Löw, V. Schweikhard, A. Grabowski, Yu. B. Ovchinnikov, and T. Pfau. „Intense source of cold Rb atoms from a pure two-dimensional magneto-optical trap.“ In: *Phys. Rev. A* 66 (2 2002), p. 023410. DOI: 10.1103/PhysRevA.66.023410 (cit. on pp. 23, 26).

[96] M.D. Lukin. *Modern Atomic and Optical Physics II – Lectures by M.D. Lukin*. Notes taken and typed by L.Childress, Fall Semester 2005 (cit. on p. 24).

[97] P. D. Lett, W. D. Phillips, S. L. Rolston, C. E. Tanner, R. N. Watts, and C. I. Westbrook. „Optical molasses.“ In: *J. Opt. Soc. Am. B* 6.11 (1989), pp. 2084–2107. DOI: 10.1364/JOSAB.6.002084 (cit. on p. 24).

[98] Daniel A. Steck. *Quantum and Atom Optics*. available online at http://steck.us/teaching, revision 0.8.3 25 May 2012 (cit. on p. 24).

[99] Thomas H. Loftus, Tetsuya Ido, Martin M. Boyd, Andrew D. Ludlow, and Jun Ye. „Narrow line cooling and momentum-space crystals.“ In: *Phys. Rev. A* 70 (6 2004), p. 063413. DOI: 10.1103/PhysRevA.70.063413 (cit. on p. 25).

[100] W.C. Martin, Romuald Zalubas, and Lucy Hagan. *Atomic energy levels - the rate earth elements*. Institute for Basic Standards, National Bureau of Standards, Washington D.c. 20234: National Standard Reference data system, 1978 (cit. on p. 25).

[101] K. Dieckmann, R. J. C. Spreeuw, M. Weidemüller, and J. T. M. Walraven. „Two-dimensional magneto-optical trap as a source of slow atoms.“ In: *Phys. Rev. A* 58 (5 1998), pp. 3891–3895. DOI: 10.1103/PhysRevA.58.3891 (cit. on p. 26).

[102] Thomas Uehlinger. „A 2D Magneto-Optical Trap as a High-Flux Source of Cold Potassium Atoms.“ Diploma Thesis. Universität Zürich, 2008 (cit. on p. 26).

[103] C. S. Hofmann, G. Günter, H. Schempp, N. L. M. Müller, A. Faber, H. Busche, M. Robert-de Saint-Vincent, S. Whitlock, and M. Weidemüller. „An experimental approach for investigating many-body phenomena in Rydberg-interacting quantum systems." In: *Frontiers of Physics* 9.5 (2014), pp. 571–586. DOI: 10.1007/s11467-013-0396-7 (cit. on p. 26).

[104] Herrmann Haken and Christoph Wolf. *Atom und Quantenphysik*. Berlin Heidelberg, Deutschland: Springer Spektrum, 2001 (cit. on p. 32).

[105] Wolfgang Nolting. *Grundkurs Theoretische Physik 5/2 Quantummechanik - Methoden und Anwendungen*. Berlin Heidelberg, Deutschland: Springer Spektrum, 2015 (cit. on p. 32).

[106] David Griffith. *Introduction to Quantum Mechanics*. upper Saddle River, NJ 07458: Prentics Hall, 1995 (cit. on p. 32).

[107] Johannes Schmidt. „Generation of non-classical light using ultra-cold Rydberg ensembles." Master Thesis. Universität Stuttgart, 2014 (cit. on pp. 34, 36).

[108] Robert Löw, Hendrik Weimer, Johannes Nipper, Jonathan Balewski, Björn Butscher, Hans Peter Büchler, and Tilman Pfau. „An experimental and theoretical guide to strongly interacting Rydberg gases." In: *Journal of Physics B-atomic Molecular and Optical Physics - J PHYS-B-AT MOL OPT PHYS* 45 (Feb. 2012). DOI: 10.1088/0953-4075/45/11/113001 (cit. on p. 34).

[109] M. S. O'Sullivan and B. P. Stoicheff. „Scalar polarizabilities and avoided crossings of high Rydberg states in Rb." In: *Phys. Rev. A* 31 (4 1985), pp. 2718–2720. DOI: 10.1103/PhysRevA.31.2718 (cit. on p. 36).

[110] Jürgen Appel, Andrew MacRae, and A I Lvovsky. „A versatile digital GHz phase lock for external cavity diode lasers." In: *Measurement Science and Technology* 20.5 (2009), p. 055302. URL: http://stacks.iop.org/0957-0233/20/i=5/a=055302 (cit. on pp. 41, 42).

[111] E. Donley, T. Heavner, F. Levi, M. Tataw, and S. Jefferts. „Double-pass acousto-optic modulator system." In: *Review of Scientific Instruments* 76 (2005), p. 063112. URL: http://www.aaoptoelectronic.com/wp-content/uploads/documents/AOM%20tuning.pdf (cit. on p. 42).

[112] Frank Träger. *Springer Handbook of Laser and Optics*. Heidelberg, Germany: Springer, 2012 (cit. on p. 44).

[113] Malvin Teich Bahaa Saleh. *Fundamentals of Photonics*. New York, USA: Wiley-Interscience publication, 1991 (cit. on pp. 45, 49).

[114] Eric D. Black. „An introduction to Pound–Drever–Hall laser frequency stabilization." In: *American Journal of Physics* 69.1 (2001), pp. 79–87. DOI: 10.1119/1.1286663 (cit. on pp. 46, 52).

[115] M. J. Lawrence, B. Willke, M. E. Husman, E. K. Gustafson, and R. L. Byer. „Dynamic response of a Fabry–Perot interferometer.“ In: *J. Opt. Soc. Am. B* 16.4 (1999), pp. 523–532. DOI: 10.1364/JOSAB.16.000523 (cit. on p. 47).

[116] Michael Martin. „Quantum Metrology and Many-Body Physics: Pushing the Frontier of the Optical Lattice Clock.“ PhD Thesis. University of Colorado, 2013 (cit. on p. 48).

[117] J. Alnis, A. Matveev, N. Kolachevsky, Th. Udem, and T. W. Hänsch. „Subhertz linewidth diode lasers by stabilization to vibrationally and thermally compensated ultralow-expansion glass Fabry-Pérot cavities.“ In: *Phys. Rev. A* 77 (5 2008), p. 053809. DOI: 10.1103/PhysRevA.77.053809 (cit. on p. 53).

[118] Christoph Tresp. „Rydberg polaritons and Rydberg atoms - Novel tools for quantum nonliner optics.“ PhD Thesis. Universität Stuttgart, 2017 (cit. on p. 54).

[119] A. Khintchine. *Korrelationstheorie der stationären stochastischen Prozesse*. Mathematische Annalen, 1934 (cit. on p. 63).

[120] G. Debarge P.B. Gallion. „Quantum phase noise and field correlation in single frequency semiconductor laser systems.“ In: *IEEE Journal of quantum electronics* QE.20 (1984), pp. 343–349 (cit. on p. 63).

[121] Christoph Tresp. „A Setup for Highly Precise Excitation and Detection of Rydberg Atoms.“ Master Thesis. Universität Stuttgart, 2012 (cit. on p. 63).

[122] Jonathan Balewski. „Photoassoziationsspektroskopie.“ Master Thesis. Universität Stuttgart, 2009 (cit. on p. 63).

[123] „Empirical fits to the Voigt line width: A brief review.“ In: *Journal of Quantitative Spectroscopy and Radiative Transfer* 17.2 (1977), pp. 233 –236. ISSN: 0022-4073. DOI: https://doi.org/10.1016/0022-4073(77)90161-3 (cit. on p. 64).

[124] Keysight Technologies. *Keysight N9322C Spectrum Analyzer*. Chengdu, China: Keysight Technologies, 2014 (cit. on p. 64).

[125] LeCroy Corporation. *WavePro DSO Operators Manual*. New York, USA: LeCroy Corporation, 2002 (cit. on p. 64).

ACKNOWLEDGMENTS

This work is was not accomplished solely by myself and I did not want to take credit for that. All people who contributed directly or indirectly to it, thank you! Especially, I would like to mention

— my supervisor Sebastian Hofferberth who deserves a special thanks! Funnily, I didn't meet you during our mutual time in Stuttgart but I had to move to Denmark to join your group. I am happy that you convinced me to extend my Erasmus semester and that you offered me the opportunity to be part of setting up this intriguing experiment from scratch. Not only did I learn a lot of interesting physics during the time in our lab but I want to say that I also acquired some foosball skills.

— all current group members Simon Ball, Nina Stiesdal, Hannes Busche, Aksel Nielsen, Mohammad Noaman but also the former ones Christoph Tresp, Christoph Braun and Julia Bjørnstrøm. It is a pleasure to work in such a nice group atmosphere, especially the awesome self-cooked food I enjoyed from you guys!

— Simon Ball with whom I mainly worked on this project. Besides the discussions about physics I learned a lot about the interesting British humor.

— Nina Stiesdal who is an inspiring person. Your drawings on the milk and on the fruits always brings a smile on my face, even in the early morning hours. This really makes my day. Manger tak for sidste år i Danmark!

— Hannes Busche for giving great, last-minute feedback even during the Christmas days. Thanks a lot for that, you saved me!

— Aksel Nielsen who is a really tough teacher in Danish pronunciation. Brød!

— Christoph Tresp and Christoph Braun who I didn't meet until I moved to Denmark. Thanks for receiving me into this nice group in the very beginning. Not only could I discuss physics topics with you but also refresh my Swabian. Mir danget schee!

— Torben Sørensen and Lars Hansen of the mechanical workshop who did incredible work machining all metallic parts and Dany Kyrping of the electronic workshop who helped us building a lot of electronic parts of the experiment.

— my family. Mama, Papa, vielen Dank für all Eure Unterstützung über die letzten Jahre. Ohne Eurer Vertrauen und Euren Zuspruch hätte ich es mit Sicherheit nicht bisher hierher geschafft. Meine Geschwister, Alex, Lennart und Elena, ich hoffe wir bleiben uns immer so verbunden!